Orbital decay of objects in a low Earth orbit

Analysing the effect of the aerodynamic characteristics and initial state uncertainty on orbital decay

MSc Thesis

Luis Miguel Peña

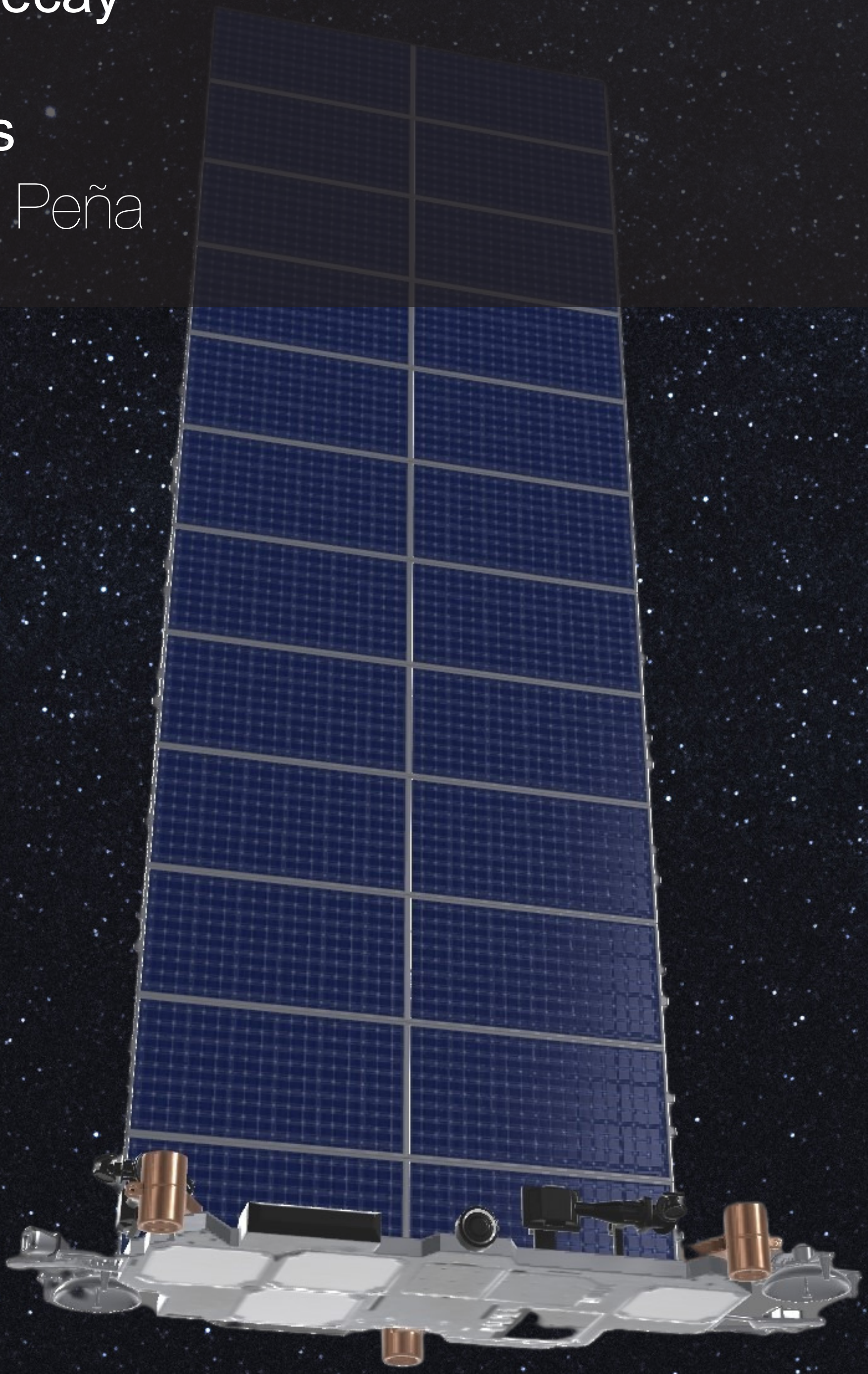

Delft University of Technology

TU Delft

Orbital decay of objects in a low Earth orbit

Analysing the effect of the aerodynamic characteristics and initial state uncertainty on orbital decay

by

Luis Miguel Peña

to obtain the degree of Master of Science
at the Delft University of Technology,
to be defended publicly on Friday, July 16, 2023 at 9:30am

Student number:	4647041	
Thesis Committee:	Prof. Dr. L.L.A. Vermeersen	TU Delft, chair
	Dr. A. Sciacchitano	TU Delft, examiner
	Dr. Ir. E. Mooij	Tu Delft, supervisor
	Dr. Ir. C. Siemes	Tu Delft, supervisor
Institution:	Delft University of Technology,	Faculty of Aerospace Engineering
Place:	Delft, The Netherlands	

Starlink satellite render. Adapted from `https://shorturl.at/eHO34`

TU Delft

Preface

With this piece of paper, I mark the ”end” of my time at Delft. After what have been some of the best, and worst, months of my life, I have finally completed this task. I am not too sure how I feel about this stage of my life finally coming to an end, but as I have said uncountable times during my updates meetings, ”It is what it is”.

I want to end this journey by thanking everyone who has been here for me throughout this process. For starters, I would like to firstly thank my supervisors, Erwin and Christian. They have dealt with a lot of me in the past few months. I will forever be grateful to them for being a pain in my *** and pushing me to work harder. I will miss our morning meetings, where we spent a significant amount of time invested in telling the stories from the night before, and those late-night email chains. Overall, I could not have asked for a better duo to supervise this process. I will forever be thankful for what you have done for me during this period.

Now, moving to my incredible roommates throughout the thesis months who have heard all my screams of joy and frustration. I could not have done this without their constant support, be it from those dinner nights, having motivational beers or simply lending me a pillow to punch. We now know that all those hours were well spent. In addition, I would also thank the admins. Although a short stay together here in Delft, most of which we do not remember, we grew to have a lovely friendship. You will forever have a friend in me. I could not forget the CR2GL, for all those invested hours in learning new skills. And to everyone else that made this time at Delft a very pleasant one, I thank you. I could not have done any of this without them.

Finally, I would like to thank my parents and family. Although not physically present, I know I can count on them for anything I ever need. I could not have been any more lucky with the immeasurable support I got from them. I know I do not say it very often, but I do love them.

Luis Miguel Peña
Delft, June 2023

Abstract

The ever-increasing number of massive satellite constellations in orbit poses a threat not only to all the satellites in those altitudes but also to humans in Earth. Once these satellites stop being functional and start decaying, it is of key importance to be able to accurately predict the re-entry behaviour of these satellites. In order to improve the re-entry prediction, one option is to have a better estimate of the re-entry interface, the position when the decaying satellite reaches 120 km altitude. This is the main topic of this thesis. As a matter of fact, the research question to answer this dilemma is the following:

To what extent is it possible to improve the re-entry epoch prediction by using more accurate aerodynamic modelling of the object in orbit while also taking into account initial state, translational and rotational, uncertainties such that impact analysis on Earth will be more accurate and reliable?

To address this research question, the project encompasses the following subquestions:

1. Is there an improvement in the re-entry epoch prediction when using variable values for the aerodynamic coefficients?
2. What is the effect of adding rotational dynamics to the re-entry interface epoch prediction?
3. What is the effect of the initial state uncertainty on the re-entry epoch prediction?
4. Is it possible to perform a re-entry epoch prediction on the current Starlink satellites? If so, what is the change in the accuracy of epoch prediction with respect to the ESOC prediction model?

The thesis investigates the impact of employing variable values for the aerodynamic coefficients on re-entry interface epoch prediction accuracy. By considering a number of parameters such as the object's shape, attitude relative to the flow, atmospheric density, and the satellite's relative velocity, the research aims to determine if more precise aerodynamic coefficient modelling can lead to improved predictions of re-entry epochs. The use of Stochastic PArallel Rarefied-gas Time-accurate Analyzer (SPARTA), a Monte-Carlo simulation technique, is used to generate these coefficients.

Additionally, by incorporating rotational dynamics into the orbital decay process, the research explores the influence of object initial attitude and rotation rate and its associated uncertainties on the accuracy of epoch predictions. These additions will provide enough data such an analysis on the effect of rotational dynamics on prediction of the re-entry interface epoch can be carried out. Furthermore, the thesis also focuses on evaluating the initial translational state uncertainty on the re-entry interface epoch. With the use of TLE data and their corresponding errors, a number of simulations are run to understand the uncertainty effect on the re-entry epoch prediction. Finally, the thesis explores a more practical approach. By analysing the latest available TLE of a Starlink satellite in orbit, the software developed in this project predicts the re-entry interface epoch of a Starlink satellite. This value is compared with the existing prediction from the European Space Operations Centre (ESOC).

The conclusions reached from this thesis shed answer a number of the sub-questions previously presented. The main conclusions are the following:

- *Accuracy of re-entry prediction with variable aerodynamic coefficients*
  Simulation 1 highlighted that using a constant aerodynamic coefficient might not accurately represent real-life situations. The behaviour of the Starlink satellite demonstrated a significant dependency on $C_D A$. This finding suggests that employing a constant aerodynamic coefficient for force interactions may lead to inaccurate predictions of the re-entry interface epoch. Additionally, adding the lift force in simulation models, which is often overlooked in current prediction models, can be crucial for specific shapes like Starlink, as the values from the lift force are not small enough to be ignored.

- *Effect of rotational dynamics on re-entry prediction*
  Simulations 2 and 3 revealed that rotational dynamics play a crucial role in predicting the re-entry interface epoch due to their impact on the average C_DA of the satellite. These simulations concluded that considering rotational dynamics reduces the range of C_DA experienced by the satellite. As a result, this reduction leads to a narrower spread of re-entry interface epoch predictions.
- *Influence of initial state uncertainty on re-entry prediction*
  Simulation 1.6 and Simulation 3 concurred that the effect of initial Two-Line Element (TLE) errors on re-entry interface epoch prediction is not significant compared to the effect of the average C_DA experienced by the satellite during orbit propagation. While initial TLE errors in translational motion may widen the final re-entry interface epoch window, the C_DA dominates the prediction. Moreover, the simulations found no correlation between the initial attitude and the final re-entry interface epoch, suggesting that a nominal attitude case can be applied to all propagations when rotational dynamics are included.
- *Re-entry epoch prediction for Starlink satellites and comparison with existing models*
  The analysis for Starlink 1181 satellite, which is currently in orbit, was carried out and compared versus the predictions from the European Space Operations Centre (ESOC). There was a seven day offset between the prediction from this thesis and the ESOC one. However, from the results of Simulation 4, it was found that a discrepancy of approximately six days in the prediction compared to the last available TLE existed. When applying these 6 days as a correction factor to the predicted re-entry interface epoch window, the research aligns closely with that of the ESOC prediction.

In conclusion, the findings suggest that more accurate aerodynamic modelling is crucial for enhancing re-entry interface epoch prediction. The dependency of the prediction on the average C_DA experienced by the satellite was significant and not adequately captured by TLE data. It is important to note that using freely rotating rotational dynamics far from re-entry may not be recommended, as the satellite likely maintains a nominal attitude with active attitude control systems until closer to re-entry. More information on the behaviour of the satellite would be required to perform a better decay analysis. It is also recommended to conduct sensitivity analyses of density and aerodynamic coefficients and to investigate different satellite shapes to enhance re-entry epoch prediction capabilities. Implementing these recommendations will contribute to more reliable and accurate predictions for re-entry epochs and impact analysis, advancing the field of orbital decay studies.

Contents

Preface iii

Abstract v

Nomenclature xi

1 Introduction 1

I Background Information 5

2 Mission Heritage 7
- 2.1 Orbit Decay . . . 7
- 2.2 Interactions between the Sun and Earth . . . 8
  - 2.2.1 Radiation and Solar Activity . . . 9
  - 2.2.2 Solar Winds and Geomagnetic Activity . . . 10
- 2.3 Previous Research . . . 10
  - 2.3.1 Atmospheric Modelling . . . 11
  - 2.3.2 Thermospheric Winds . . . 12
  - 2.3.3 Aerodynamic modelling . . . 12
  - 2.3.4 Conclusion . . . 13

3 Case Study 15
- 3.1 Requirements . . . 15
  - 3.1.1 Orbit Requirements . . . 15
  - 3.1.2 Environment Requirements . . . 17
  - 3.1.3 Aerodynamic Requirements . . . 18
- 3.2 Reference Mission: Starlink Satellites . . . 18
  - 3.2.1 Starlink Sizing . . . 19

4 Satellite Dynamics 23
- 4.1 Keplerian Elements . . . 23
- 4.2 Two-Line Element . . . 23
  - 4.2.1 Generation of TLE . . . 24
  - 4.2.2 TLE Applications and Errors . . . 25
- 4.3 Reference Frames . . . 26
  - 4.3.1 Different Reference Frames . . . 26
  - 4.3.2 Frame Transformation . . . 27
- 4.4 Quaternions . . . 29
- 4.5 Equations Of Motion . . . 29
  - 4.5.1 Translational EoM . . . 30
  - 4.5.2 Rotational EoM . . . 30
  - 4.5.3 Perturbing Forces and Torques . . . 31

5 Aerodynamic Modeling 35
- 5.1 Flow Regimes . . . 35
  - 5.1.1 Continuum Flow Regime . . . 35
  - 5.1.2 Free Molecular Flow Regime . . . 36
  - 5.1.3 Transition Regime . . . 38
- 5.2 Aerodynamic Coefficients . . . 38

II Software Architecture 41

6 SPARTA Set-Up 43
6.1 Software Architecture . . . 43
6.2 Mesh . . . 45
6.3 SPARTA. . . 46
6.3.1 Set-up conditions . . . 46
6.3.2 Simulation Inputs . . . 47
6.3.3 Speed Ratio Simulation Trick . . . 48
6.3.4 Input Files for SPARTA . . . 48
6.4 SPARTA and TUDAT rotation angles . . . 49
6.4.1 Set up of object in TUDAT . . . 49
6.4.2 Set up of object in SPARTA . . . 50
6.4.3 SPARTA rotations . . . 50
6.4.4 SPARTA and TUDAT link. . . . 51
6.5 SPARTA Output Post-Processing . . . 51
6.6 SPARTA Database . . . 52
6.6.1 Speed Ratio Selection . . . 54
6.6.2 Aerodynamic Angles Selection . . . 54
6.6.3 Database Generation. . . . 57

7 TUDAT Set-Up 59
7.1 Environment Set-Up . . . 59
7.1.1 Earth Modelling . . . 59
7.1.2 Thermospheric Winds Model: HWM14 . . . 60
7.1.3 Atmospheric Model: NRLMSISE-00 . . . 61
7.2 Orbital Perturbations . . . 62
7.2.1 Gravitational Field of Earth . . . 62
7.2.2 Third Body Perturbations. . . . 62
7.2.3 Solar Radiation Pressure. . . . 63
7.2.4 Aerodynamic Perturbations . . . 63
7.3 Starlink Properties . . . 64
7.4 Propagator and Integrator . . . 65
7.4.1 Numerical Methods . . . 66
7.4.2 Propagator . . . 67
7.4.3 State Model . . . 68
7.4.4 Integrator Selection. . . . 68
7.5 Initial State Generation . . . 71
7.5.1 Initial Translational State . . . 71
7.5.2 TLE Errors . . . 71
7.5.3 Initial Rotational State . . . 72

8 Verification and Validation 73
8.1 Verification TUDAT . . . 73
8.1.1 Acceptance Tests . . . 73
8.1.2 Verification NRLMSISE-00 . . . 75
8.1.3 Verification HWM14 . . . 75
8.1.4 Verification Aerodynamic Coefficient Interpolator . . . 76
8.2 Verification SPARTA . . . 77
8.2.1 Verification Force Coefficient. . . . 77
8.2.2 Verification Flow Regime . . . 78
8.2.3 Verification Moment Coefficients. . . . 79
8.3 Validation Software . . . 80
8.3.1 Simulation V&V 1: Fixed Inertial Attitude . . . 81
8.3.2 Simulation V&V 2: Validation Versus Other TLE . . . 82

III Results 85

9 Simulation Results 87
- 9.1 Simulation 1: Constant Aerodynamic Angles . . . 88
  - 9.1.1 Simulation 1 Set-Up . . . 88
  - 9.1.2 Results Simulation 1 . . . 89
  - 9.1.3 Simulation 1.5 . . . 91
  - 9.1.4 Simulation 1.6 . . . 92
- 9.2 Simulation 2: Random Initial Attitude and no TLE Error . . . 93
  - 9.2.1 Simulation 2 Set-Up . . . 94
  - 9.2.2 Results Simulation 2 . . . 95
- 9.3 Simulation 3: Random Initial Attitude and TLE Error . . . 97
  - 9.3.1 Simulation 3 Set-Up . . . 97
  - 9.3.2 Results Simulation 3 . . . 98
- 9.4 Simulation 4: Re-entry Epoch Spread vs Initial TLE . . . 98
  - 9.4.1 Simulation 4 set-up . . . 100
  - 9.4.2 Results Simulation 4.1 and Simulation 4.2 . . . 101
  - 9.4.3 Results Simulation 4.3 . . . 103
- 9.5 Simulation 5: Into the Future . . . 104
  - 9.5.1 Simulation 5 set-up . . . 104
  - 9.5.2 Results Simulation 5 . . . 105

10 Conclusions and Recommendations 107
- 10.1 Conclusion . . . 107
- 10.2 Recommendations . . . 108

References 114

Nomenclature

Abbreviations

Abbreviation	Definition
CHAMP	CHAllenging Minisatellite Payload
CMR	Common Metadata Repository
CoM	Center of Mass
DAC	DSMC Analysis Code
DOY	Day Of Year
DSMC	Direct Simulation Monte Carlo
DTM	Drag Temperature Model
DUT	Delft University of Technology
EFAST	Extended Fourier Amplitude Sensitivity Test
ESOC	European Space Operations Centre
EoM	Equations of Motion
ERS-2	European Remote-sensing Satellite 2
ESA	European Space Agency
FPI	Fabry-Perot Interferometer
GOCE	Gravity field and steady-state Ocean Circulation Explorer
HWM14	Horizontal Wind Model 14
ISA	International Standard Atmosphere
LST	Local Solar Time
MSFC	Marshall Space Flight Center
NASA	National Aeronautics and Space Administration
NRLMSIS	Naval Research Laboratories Mass Spectrometer and Incoherent Scatter model
PCHIP	Piecewise Cubic Hermite Interpolating Polynomial
SGP4	Simplified General Perturbation model 4
SPARTA	Stochastic PArallel Rarefied-gas Time-accurate Analyzer
TLE	Two Line Element set
TUDAT	TU Delft Astrodynamics Toolbox
USSTRATCOM	United States STRATegic COMmand
UV	Ultra-Violet

Symbols

Symbol	Definition	Unit
A_{sun}	Area Facing the Sun	[m^2]
a	Semi-major Axis	[m]
B^*	TLE Ballistic Coefficient	[R$_E{}^{-1}$]
C	Reference-Frame Transformation Matrix	[-]
C_τ	Shear Coefficient	[-]

Symbol	Definition	Unit
C_D	Drag Coefficient	[-]
C_L	Lift Coefficient	[-]
C_l	Moment Coefficient in the X Direction of the Body Axis	[-]
C_m	Moment Coefficient in the Y Direction of the Body Axis	[-]
C_n	Moment Coefficient in the Z Direction of the Body Axis	[-]
C_p	Pressure Coefficient	[-]
C_{rad}	Reflectivity Coefficient	[-]
C_S	Side Force Coefficient	[-]
C_X	Force Coefficient in the X Direction of the Body Axis	[-]
C_Y	Force Coefficient in the Y Direction of the Body Axis	[-]
C_Z	Force Coefficient in the Z Direction of the Body Axis	[-]
c	Speed of Light	[m s^{-1}]
D	Drag	[N]
E	Energy	[J]
$\mathbf{e}$	Unit vector	[-]
e	Eccentricity	[-]
$\mathbf{I}$	Inertial Tensor	[kg m^2]
i	Inclination	[°]
Kn	Knudsen Number	[-]
L	Characteristic Length	[m]
l_{ref}	Reference Length	[m]
L/D	lift to Drag Ratio	[-]
M	Mass	[kg]
M	Mach Number	[-]
M	Mean Anomaly	[rad]
m	Mass	[kg]
N	Gas Density	[kg m^{-3}]
$P_{n,m}$	Legendre Function	[-]
p	Pressure	[N m^{-2}]
$\mathbf{q}$	Normalised Quaternions Vector	[-]
q_∞	Dynamic Pressure	[kg m^{-2} s^{-1}]
$\ddot{\mathbf{r}}$	Acceleration	[m s^{-2}]
$\dot{\mathbf{r}}$	Velocity	[m s^{-1}]
$\mathbf{R}$	Body-Frame Transformation matrix	[-]
R	Gas Constant	[J K^{-1} mol^{-1})]
R	Radius of body	[m]
$\mathbf{r}$	Position Vector	[m]
r	Distance	[m]
S	Cross-sectional Area	[m^2]
S_{sun}	Mean Solar Flux at 1 au	[W m^{-2}]
$\mathbf{s}_i$	Position From Third Body to Centre of Main Body	[m]
s	Molecular Speed Ratio	[-]
$\mathbf{T}$	Perturbation Moments Matrix	[Nm]
T	Temperature	[K]
t	Time	[s]
U	Gravitational Potential	[J kg^{-1}]
$\mathbf{V}_\infty$	Velocity Vector	[m s^{-1}]
V	Speed Relative to Surrounding Atmosphere	[m s^{-1}]
v	Speed Relative to Earth's Geometric Centre	[m s^{-1}]
$\mathbf{x}$	Distance Vector Between Original CoM and New CoM	[m]

Symbol	Definition	Unit
α	Angle of Attack	[-]
α_E	Accommodation Coefficient	[-]
β	Sideslip Angle	[rad]
γ	Ratio of Specific Heats	[-]
γ	Flight Path Angle	[rad]
δ	Latitude	[rad]
δ_{ij}	Kronecker Delta	[-]
θ_i	Inclination Angle	[rad]
θ	Pitch Angle	[rad]
λ	Mean Free Path	[m]
μ	Standard Gravitational Parameter	[m^3 s^{-2}]
ρ	Density	[kg m^{-3}]
σ	Bank Angle	[rad]
σ	Effective Gas Particle Diameter	[m]
τ	Longitude	[rad]
τ	Shear Stress	[N m^{-2}]
ϕ	Roll Angle	[rad]
χ	Heading Angle	[rad]
Ψ	Yaw Angle	[rad]
$\boldsymbol{\omega}$	Rotation vector	[rad s^{-1}]
Ω	Longitude of Ascending Node	[rad]
$\boldsymbol{\omega}$	Angular Velocity	[rad s^{-1}]
ω	Angular Speed	[rad s^{-1}]
ω_{cb}	Angular Speed of Central Body	[rad s^{-1}]
ω	Argument of Pericentre	[rad]

1

Introduction

What goes up must come down. Such a common saying cannot describe better the aim of this project. To try to better understand how objects come down. Thanks to pioneers in previous generations, such as Newton or King-Hele, we now know the physics behind such a motion, and we can describe and understand it. From the fall of an apple to the de-orbiting of a satellite, it is possible to predict how it will fall. When predicting the fall of objects at low altitudes, the analysis can be quite precise. However, the accuracy of the prediction as the initial altitude of the fall increases decreases by more and more the higher we go into the atmosphere. The higher we go, the harder it is to properly model the behaviour of the object. There will always be assumptions, errors and uncertainties in the model simulating the behaviour.

To fully understand orbital decay, a lot of research has to be performed. Several factors affect orbital decay, such as third-body perturbations, solar radiation pressure, atmospheric weather and aerodynamic forces, among others. Each of these perturbations will have different effects and magnitudes depending on the orbit of the object. For this project, the main focus is on the aerodynamic perturbations the object in orbit experiences in the lower thermosphere. This is because at the final stages of the orbit, drag, an aerodynamic perturbation, is the main factor contributing to the decay. Additionally, there are a lot of factors that dictate the effect of the drag on the object that is interesting to study. For instance, as the object's orbital altitude decreases the atmosphere becomes denser which in turn results in a higher drag force acting on the object.

Of course, it would be impossible to fully analyse all the effects that dictate how aerodynamics affects the object in orbit. Thus, it is important to narrow them down to be able to better understand specific aspects. Other projects can then be developed to complement the knowledge learned from this project. For this thesis, the aerodynamic coefficients, both force and moment coefficients, are generated, and their effect is tested on the orbital decay. These two sets of aerodynamic coefficients will be key to better understanding the effect of aerodynamics on orbital decay. Additionally, as previously mentioned, there are also uncertainties in the simulations of orbital decay. These will also be taken into account in this project. The main focus will be on the initial state uncertainties. The initial state consists of initial position and velocity, both of which affect translational dynamics, and the initial attitude and rotational rate, which affect the rotational dynamics.

Now let us dive in a little on the aerodynamic coefficients. The aerodynamic coefficients are composed of six coefficients, three force and three moment ones. These coefficients depend on several factors such as the velocity of the object, the density of the fluid, the shape of the object and attitude with respect to the flow, among others. To make the most realistic analysis possible, it is necessary to try and take into account as many relevant factors as possible when calculating them. To do so different techniques are used to calculate the coefficients during different stages of the orbital decay. The best technique found so far is based on a Monte Carlo simulation. This is because as the altitude is above the 100 km most of the time the object will be in a region called the free flow regime. In this region, the molecules of the gas collide more often with the object than between each other. To analyse the effect of this behaviour on the aerodynamic coefficients, a numerical model has to be used. This is because the behaviour of particles in this regime is rather random. Thus, for this project, the software called SPARTA, a Monte Carlo simulator, is used. SPARTA, as will be later explained, models the gas behaviour in a probabilistic way using Monte Carlo. The results from SPARTA can then be used to calculate the pressure and shear coefficients experienced by the object in orbit. It is then possible to calculate the aerodynamic coefficients based on these pressure and shear coefficients by surface integrating them over the area of the satellite.

The other previously mentioned main area of interest is the initial state uncertainty. As it is impossible to precisely know the position, velocity and attitude of a satellite in orbit from a measurement, there will be a set of errors, or uncertainties, in said measurement. The most common method of knowing the position and velocity of a satellite is through a database of TLEs values. As will be later explained, the TLEs are measurements that are made by the United States Strategic Command (USSTRAT-COM), and they contain information on the orbit of the object of interest. These TLEs contain a number of errors in them, which means that the satellite could have a different position and velocity than the one from the TLEs. Thus, it is important to analyse the effect of this uncertainty in the re-entry interface epoch, as it is the only information publicly available. Additionally, for the attitude and rotational rate of the satellite, no public information is available. Thus, for the analysis of this project, a random initial attitude is generated and the effect of said attitude on the final re-entry interface is studied.

Of course, it is important to ask why we are doing this research. If there is no end goal from the analysis of the orbital decay, why spend time when there are other areas of space that still require a significant amount of research? To answer this question, it is necessary to look at a stage further along the decay process of an object in orbit. After the orbit decay, the re-entry of the object begins. If the object, or pieces of it, manage to survive the extreme mechanical and thermal loads experienced during re-entry they impact Earth. The impact on Earth poses a significant risk to the people of Earth. If the impact of a large piece of debris happens to be on a city a significant number of people could be hurt, apart from the obvious economical damage that it can cause. Given the increasing number of satellites in orbit, and currently with the new trend of massive constellations, such as Project Kuiper[1] by Amazon, OneWeb by OneWeb[2] or Starlink by SpaceX[3], it is of key importance to be able to be able to have an accurate prediction of the decay of these satellites in order to prevent any potential damages if any debris survives the re-entry phase. Thus, the preliminary research question for the project arises:

To what extent is it possible to improve the re-entry epoch prediction by using more accurate aerodynamic modelling of the object in orbit while also taking into account initial state, translational and rotational, uncertainties such that impact analysis on Earth will be more accurate and reliable?

From the research question, it is then possible to also define the research objective, which is:

To achieve an improved re-entry epoch prediction by means of applying a more accurate aerodynamic model of the object in orbit and taking into account initial state uncertainties to have a better impact prediction on Earth.

From the research question and objective, four main aspects can be singled out. Firstly, the aerodynamic model is used for the object in orbit. The aerodynamic model used should be better than the current models. Nowadays, a constant drag area is used for orbit propagation calculations. Thus, one of the aims is to have a better aerodynamic model by having several different aerodynamic coefficients based on flight conditions. To do so, the Monte Carlo simulation software SPARTA will be used. Thus, the first question to answer becomes the following:

1. Is there an improvement in the re-entry epoch prediction when using variable values for the aerodynamic coefficients?

The second aspect that is pointed out from the research objective is the effect of translational and rotational dynamics. The rotational dynamics are usually ignored, yet they can play a very important role in the orbital decay of the satellites due to its effects on the aerodynamic coefficients. Thus, it is of high importance to analyse the effect of said dynamics on the orbital decay and the re-entry interface epoch, which is defined as the date at which the satellite reaches an altitude of 120 km. Thus, the second question to answer arises and it is the following:

---

[1] `https://www.cnbc.com/2019/04/04/amazon-project-kuiper-broadband-internet-small-satellite-network.html` last access: 17 May 2023

[2] `https://planet4589.org/space/con/ow/stats.html` last access: 17 May 2023

[3] `https://planet4589.org/space/con/star/stats.html` last access: 17 May 2023

2. What is the effect of adding rotational dynamics to the re-entry interface epoch prediction?

The third aspect that can be selected from the research objective is the uncertainty in the initial state. As previously mentioned 12 errors could be taken into account. These are three for the position, three for velocity, three for attitude and three for the rotational rate. It is important to take these uncertainties into account, as the re-entry epoch could change by a significant amount if the initial state of the satellite is different. This difference means that even if the date of re-entry is correct, the impact analysis would result in a different possible area, which could increase the risk of landing in a populated area. Thus, it is important to take these uncertainties into account and see the effect they have on the re-entry epoch prediction. This reasoning brings us to the third question to be answered, which is:

3. What is the effect of the initial state uncertainty on the re-entry epoch prediction?

Finally, the last aspect of importance is to achieve the improved re-entry epoch, or at least try to. To do so, analysis on a current spacecraft that will re-enter Earth in a near future would be critical to show the prediction is better. This is the main reason why the Starlink constellation was chosen for the analysis. The Starlink satellites deorbit at a high rate due to the low altitude they operate at and the large number of satellites there are in the constellation. Thus, after having the model verified and validated with previous re-entries of Starlink satellites, it will be used to see if it can accurately predict the Starlink decay. Comparison with predictions from other sources, such as ESA, will be done to be able to comment on the accuracy of the prediction. This brings us to the last question to answer, and it is the following:

4. Is it possible to perform a re-entry epoch prediction on the current Starlink satellites? If so, what is the change in accuracy of epoch prediction with respect to ESOC prediction model?

In order to answer this question, the thesis is structured as follows. Firstly, in Chapter 2, the background information regarding orbital decay, the effects of the aerodynamic coefficients, with focus on the drag, the different interactions between the Sun and the Earth and the different environment models are given. Then, in Chapter 3, the mission requirements and the case study of the Starlink satellites are introduced and elaborated upon. Next, in Chapter 4, the most important reference frames, orbital elements and the equation of motion that determine the satellite dynamics are introduced. Once the dynamics are clear, the focus will shift to the aerodynamic modelling of the satellite and the different aspects that affect the aerodynamic coefficients. This information is provided in Chapter 5. Afterwards, the software architecture is given in Section 6.1. Though a brief section, it provides a clear overview of the final software set-up and the interdependencies between the different aspects of the software. Subsequently, the set-up of SPARTA along with the results and post-processing of said results is provided in Chapter 6. Next, the set-up of TUDAT with all the environment parameters, the orbital perturbations and the propagator and integrator selection for the thesis is given in Chapter 7. Only then, once all the software is properly introduced and explained, the verification and validation that was performed for all the different areas of the software is provided in Chapter 8. At that point, when the software has been verified and validated, the results can be generated. A number of simulations and their corresponding results and analysis of said results are given in Chapter 9. Finally, the thesis comes to a conclusion in Chapter 10. In the last section a wrap up of all the different aspects of the project is given. Additionally, the recommendations and improvements for future cases are given.

Part I

Background Information

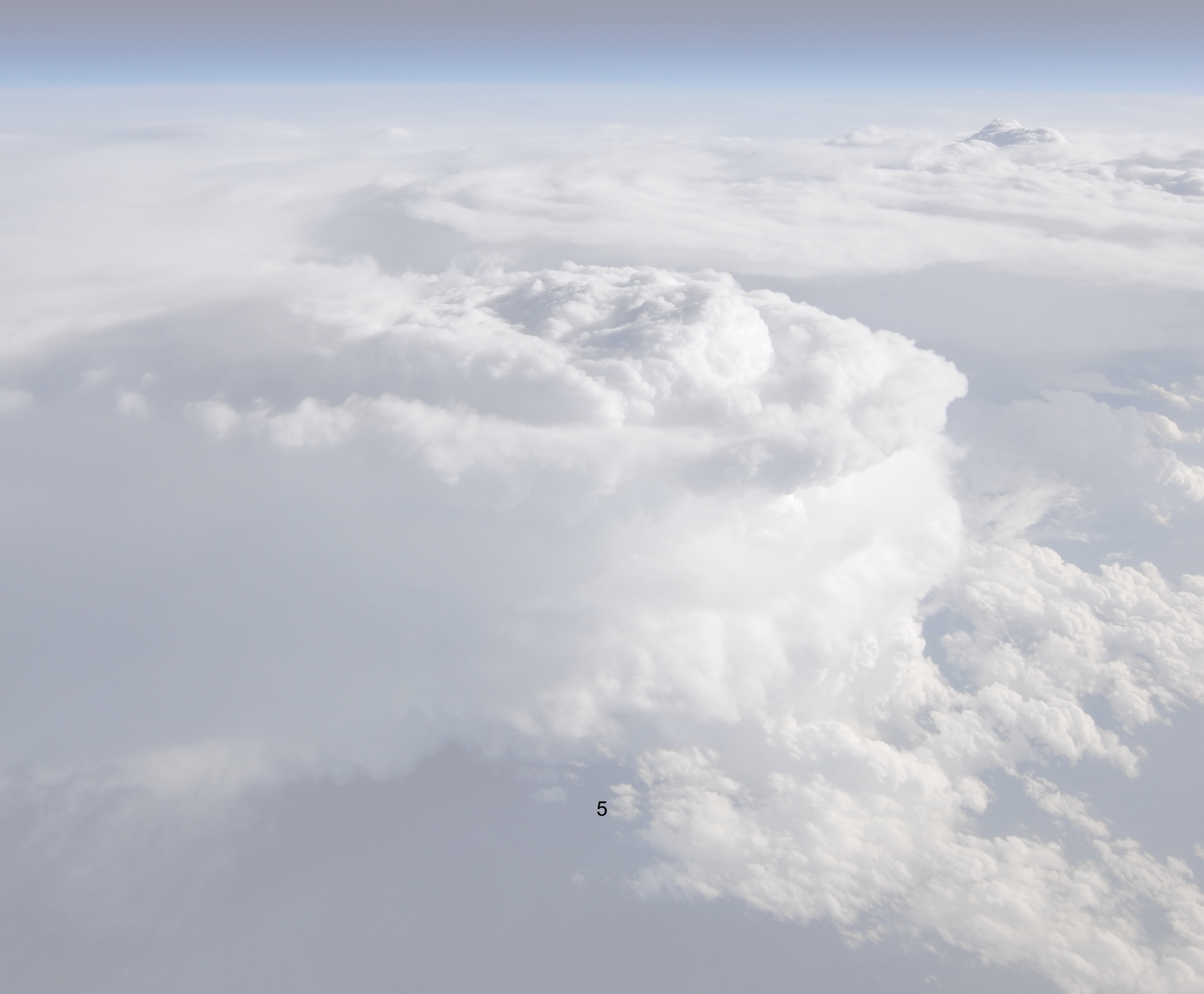

2

Mission Heritage

This section reviews previous research on the effect of the upper atmosphere on the propagation of an orbit. This research will provide useful information which can be used as the introduction point for the project. The chapter is structured into four sections. Section 2.1 gives an introduction to orbit decay analysis and opens the discussion about all possible aspects that need to be taken into account. This is followed by Section 2.2 where the interactions between the Sun and the Earth's atmosphere are explained. Next, Section 2.3.1 talks about the importance of the atmospheric model and goes over the atmospheric model used. Finally, Section 2.3.2 covers the thermospheric wind model used.

2.1. Orbit Decay

Part of the goal of the project is to be able to predict more accurately the entry point of the vehicle into the lower atmosphere. Even today, with all the technological advances and data collected, an accurate prediction of the orbital decay rate is extremely challenging. Thus, it is imperative to understand which effects are relevant for the current analysis and how these effects affect the orbits in the long run.

It was this research that brought to my attention the publications of Desmond King-Hele, considered one of the founding fathers of orbit decay analysis. In his book, *Theory of Satellite Orbits in an Atmosphere*, King-Hele [1964] provides a great analytical insight into the behaviour of orbits when an atmosphere is present. The analytical solution to the changes in different orbital parameters, from eccentricity to semi-major axis and orbital period, are explained in detail. Additionally, the effect of atmospheric drag, along with the uneven gravitational field of the Earth, are quantified for these parameters and ”simple” integrals are provided for a first initial estimate.

Nevertheless, the most important take from the book was not the analytical solutions, but the understanding of which effects are the most influential on orbital decay. It goes without saying that aerodynamic forces are one of the most important, if not the greatest, factors influencing orbital decay. The aerodynamic forces can be decomposed into three different ones, lift, side force and drag. The drag is of high interest to us because it acts on the direction of the velocity, and thus slows down the satellite, is usually modelled using the following equation:

$$D = \frac{1}{2}\rho V^2 S C_D \tag{2.1}$$

where V is the velocity of the object relative to the surrounding atmosphere, ρ the density, S the reference area and C_D the drag coefficient.

Of all the previously mentioned components of the drag equation, not a single one is known with full certainty for the satellite in orbit. Thus, it becomes critical to understand the behaviour of all the different components, how to calculate them and be able to quantify the uncertainty in the parameters previously calculated. To begin with, the value of the atmosphere's density can be either measured or calculated from different methods, such as the orbit decay of satellites. Whichever method is used, there are a number of factors that influence the density of the atmosphere. Some of the main factors are the solar cycle, day-and-night cycles and geomagnetic activity [King-Hele 1964; Bruinsma and Boniface 2021]. To further understand the topic, a more in-depth analysis of the atmospheric density and its dependency on other external factors will be given in Section 2.3.1 along with an analysis of the atmospheric model used.

The second aspect that is of interest is the velocity of the satellite relative to the Earth. The value of V given in Equation (2.1) is the velocity of the object relative to the surrounding atmosphere. However, it is of interest to know the velocity of the satellite relative to the Earth's geometric centre. To do so, King-Hele [1964] derived the following equation:

$$D = \frac{1}{2}\rho v^2 F S C_D \tag{2.2}$$

$$F = (1 - \frac{rw}{v}\cos i)^2 \tag{2.3}$$

where v is now the velocity of the satellite relative to Earth's geometric centre and F is described as seen in Equation (2.3) by King-Hele [1964]. In Equation (2.3), r represents the orbital radius, i is the inclination of the orbit and w is the rotational velocity of the Earth. Thus, F can be interpreted as the effect of the atmospheric rotation on drag. Said effect is of importance as the atmosphere rotates together with the Earth, but the object in orbit does not. This creates a difference in the velocity relative to the atmosphere that should be taken into account. As it is expected, the value of F is not perfectly known for a satellite. This is due to the fact that while the rotation of Earth is known to a high degree of accuracy the second factor that determines the value of F, the thermospheric winds, are not easy to predict and model. More information on thermospheric winds and what will be applied to this study will be provided later on in Section 2.3.2.

The next aspect of the drag equation to be analysed is the drag coefficient C_D. From the research performed, it is clear that there are a couple of aspects that affect the calculations of the drag coefficient. Firstly, for a satellite whose orbit is above the 120 km altitude the density coefficient calculations become more complicated as the flow in which the satellite is in cannot be considered to be a continuum any more. At these altitudes, the flow can either be in a transition regime or a free molecular flow. More on the different flow regimes will be provided in Chapter 5. It should be noted that the main focus of the calculations will be on the free flow regime as the satellite will, for most of its lifetime, be in this regime. Nonetheless, the transition regime will be taken into account, as this regime will play a very important role in the last revolutions of the orbit before the re-entry point.

The next aspect to take into account is that, during the free flow regime, the particles do not have the same behaviour as that of the continuum flow. When in contact with the satellite surface, the particles are re-emitted and two main aspects need to be considered. Firstly, there is the question of how much energy the molecules lost after the collision with the surface. In order to calculate the lost energy, a new variable, called accommodation coefficient, α_E, and defined as seen in Equation (5.3), is introduced. The second aspect of re-emission to take into account is the angle of re-emission. As the molecules are re-emitted from the surface of the satellite, different possible angular distributions for the re-emission can be applied [Moe et al. 1998]. More on the accommodation coefficient and re-emission distribution will be provided in Chapter 5.

Finally, the last aspect of the drag equation that needs to be analysed is the value of the reference area S. The definition of the area is a relatively easy task, it is the cross-area that is facing the direction of the velocity. However, as the reference area depends on the satellite's shape, its orientation with respect to the incoming air and the rotation of the satellite said area will be constantly changing, and thus it will be complicated to define properly. A scaling method is performed in this thesis in order to take into account this constantly changing area. More information on the generation of the aerodynamic coefficients will be given in Chapter 6.

2.2. Interactions between the Sun and Earth

One of the most important aspects of the project at hand is to better understand the effect of atmospheric density in orbital decay. In order to fully understand the effect of the atmosphere on orbital decay, it is necessary to understand what factors affect the density of the atmosphere. As can be expected, the Sun plays a major role in the changes in atmospheric properties due to the amount of energy that it produces and reaches Earth. This energy reaches Earth in two ways, radiation and solar wind. The aim of this section is to explore these two ways more in-depth. To do so, Section 2.2.1 explains the effect of the

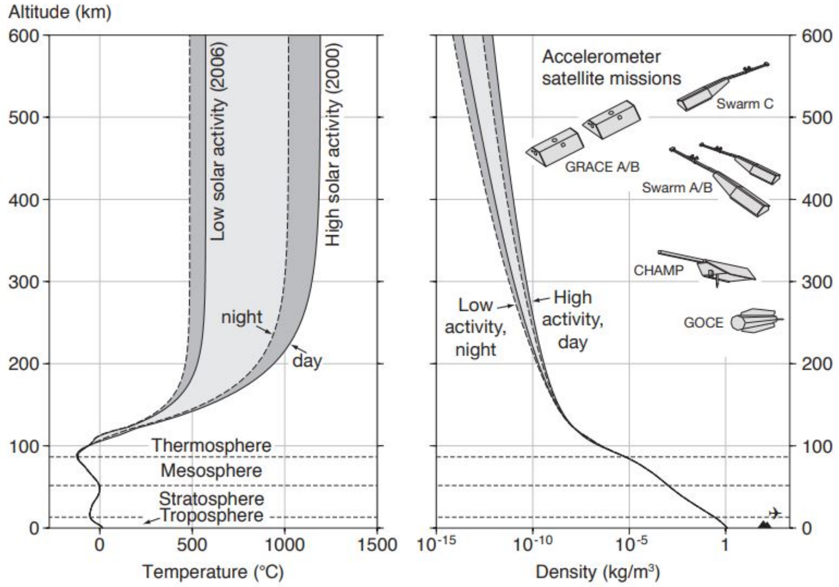

Figure 2.1: Altitude profiles of atmospheric temperature (left) and density (right), according to the NRLMSISE-00 model, evaluated for 18:00 on July 15 2000 and 2006, over Delft, The Netherlands [Doornbos 2011]

radiation energy received by the Earth. Then, Section 2.2.2 introduces and focuses on the effect of solar winds on the atmosphere.

2.2.1. Radiation and Solar Activity

The physics behind the behaviour of the Sun and the energy that is irradiated by the Sun is quite complicated. For this project, the most relevant aspect is that it is the shortest wavelengths of the emissions that are responsible for the heating of the atmosphere. The radiation on these small wavelengths is often called ultraviolet (UV) and extreme ultraviolet (EUV) radiation. These wavelengths cause the heating of the thermosphere, which leads to changes in atmospheric properties [Rees 1989; Hargreaves 1992]. The level of radiation that arrives at Earth in these wavelengths depends on the activity level of the Sun, and the effect on Earth is most notable on the face facing the Sun. From there, our first two drivers of atmospheric arise. The first one is the solar activity and the second one is the day-to-night variation. A more in-depth explanation will now be given. For reference, in Figure 2.1, it is possible to see the effect of these two effects on the density and temperature profiles of the atmosphere.

Diurnal Variations

To begin with, there is the effect of day-to-night variations. As the Sun is not heating the whole atmosphere at the same time, there is a range of densities and temperatures for the different days and nights of the year. This variation is also subjected to seasonal changes due to the Sun-Earth positioning. In the lower atmosphere, the effect of the day-to-night variation is an increase in density and temperature during the daytime followed by a decrease in density and temperatures to a minimum during the nighttime.

Solar Activity Variation

As previously explained, the most influential wavelengths for the heating of the atmosphere are UV and EUV. Unfortunately, the Sun does not have a constant emission of these radiation wavelengths. The level of solar radiation in these wavelengths depends on the so-called Sunspots. Sunspots are active regions of the Sun that produce solar flares. These solar flares can release higher radiation on the UV and EUV wavelengths, among others. The variation in the emission of radiation in these wavelengths depends on the so-called solar cycle. Each solar cycle lasts around 11 years and during the minima, there are fewer sunspots. This results in a low emission of EUV radiation, which in turn means the atmosphere receives less energy and heats up less. This can be seen by the lower temperatures and densities in Figure 2.1. The contrary is true for the solar maxima period.

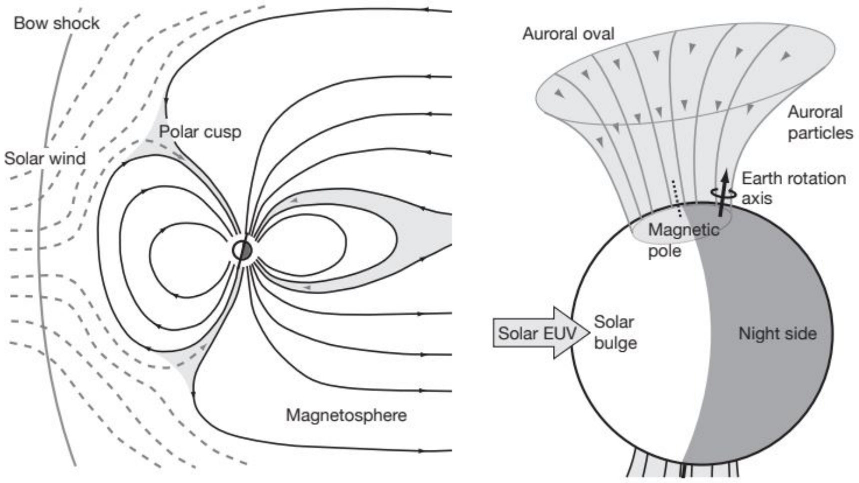

Figure 2.2: Schematic views of the Earth's magnetosphere, the polar cusps and their relation with processes affecting thermosphere density variations [Doornbos 2011]

It is important to note that even though these sunspots are unpredictable, it is possible to watch them ahead of time. Due to the period of the Sun's rotation, which is almost 27 days, it is possible to have a good prediction of the number of sunspots in that time margin. Once again, this is only an approximation as new sunspots could arise in a moment, but it is a good prediction of the incoming EUV activity.

As might be expected, to be able to quantify the effect of these radiation wavelengths on the atmosphere, an index must be used. The most commonly used index is the $\mathrm{F}_{10.7}$ solar activity proxy. This proxy was created as it shows a good correlation with the thermospheric density [Tapping 2013]. The $\mathrm{F}_{10.7}$ proxy is the amount of energy received from the Sun at the 10.7 cm wavelength. The range of values of the $F_{10.7}$ could, in theory, be from 0 to infinite solar flux units (sfu). However, no value lower than 50 or higher than 457.9 sfu has ever been recorded[1].

2.2.2. Solar Winds and Geomagnetic Activity

The second energy source of interest is the so-called solar wind. Solar wind transmit a continuous stream of charged particles into the magnetic field of Earth. Most of the particles are deflected by the magnetic field of Earth. However, a fraction of these particles enter through the poles into the Earth's atmosphere, causing geomagnetic storms. These storms introduce a lot of extra energy into the thermosphere, causing sudden changes in the density and temperature composition of the atmosphere. For reference, the energy deposited in the thermosphere due to the geomagnetic storms is usually about one-fourth of the energy absorbed from the EUV radiation [Knipp et al. 2004]. A visual representation of the solar winds and the interaction with the magnetic field and thermosphere can be seen in Figure 2.2.

Similar to EUV radiation, the intensity of solar winds from the sun is not constant. During the calm period of the solar cycle, the solar winds tend to have smaller and slower amounts of plasma. The opposite is true during the more active period of the solar cycle. In order to measure and quantify these geomagnetic storms, an index has been created. The two most common ones will now be explained. First, there is the K_p index. It ranges from 0 to 9 in discrete steps of one-third [Thomsen 2004]. The K_p index is created by using data from 11 stations around Earth in order to avoid local influences. The second very common index is the 3-hourly a_p index. The a_p index has a range from 0 to 400 nT and it is linked to the K_p index. The a_p index has some variations for different planets and different hour intervals, which could also be used.

2.3. Previous Research

One of the aims of this chapter is to gather information on research previously done which could help the future steps of this project. It is important to go through a library of previous studies in order to better understand what went well, what went wrong and what should be avoided, and what are some of the conclusions, results and recommendations that can be applied to the project at hand. Part of this research initially focused on previous theses by both Master's and PhD students at DUT. The most relevant theses found for this project are those of Toonen [2021] which focus on atmospheric winds and aerodynamic simulations, Doornbos [2011] along with his publications which had a main focus on thermospheric density, thermospheric winds and SPRATA, and finally March [2020], along with his publications, whose research helped with understanding of SPARTA and aerodynamics of the objects.

---

[1] `https://lasp.colorado.edu/lisird/data/noaa_radio_flux/` (Last access: 15 April 2023)

Afterwards, the research was expanded to other scientific papers with a focus on authors who are considered authorities in the topics. For instance, a significant amount of research was performed on the papers from J. M. Picone and J.T. Emmert who are some of the most cited members in the development and analysis of atmospheric models. Other remarkable authors whose contributions were found to be significant are E. Mooij, C. Siemes and P. Visser and J.R. Wertz, among others.

Nonetheless, it would be impossible to cover all the areas that were researched in this section. A selection of the most important aspects that need to be introduced and explained in this section was performed. Thus, this section is divided into three different parts. Firstly, the atmospheric modelling and chosen atmospheric model are introduced in Section 2.3.1. Then, the thermospheric winds are introduced in Section 2.3.2. This is then followed by a brief introduction to SPARTA and analytical methods for the analysis of the free molecular flow regime in Section 2.3.3. Finally, in Section 2.3.4 a conclusion of the different

2.3.1. Atmospheric Modelling

Now that the interactions between the Sun and the Earth are clear, it is time to dive into the atmosphere and the modelling of such in this project. As the satellite is going through different altitudes during its lifetime, it is important to have an atmospheric model that is as accurate as possible in order to reduce the errors in the numerical analysis. There have been many different atmospheric models throughout the years. From the Jacchia-70 to the newly developed NRLMSISE 2.0 and DTM2020. Each atmospheric model tries to improve on its predecessors. However, this is no easy task. To have a better model, a number of aspects need to be taken into account. From the data sets that are required to produce the model to the methods used to fill in the gaps in the data sets. This process requires not only time but also data that can be verified.

For this project, the NRLMSISE-00 atmospheric model was chosen. This decision followed a deep analysis of the different available models, the requirements for this project and the complexity of the implementation of each model. A brief introduction to the model, the limitations and the set-up will now be given.

NRLMSISE-00

The NRLMSISE-00 model is a semi-empirical model. This means that the model fits the collected data into a model and when there is no data for a given time period, location or geophysical conditions it provides fitted data for those variables. The model takes statistical variability into account when interpolating or extrapolating the data for the missing cases. The missing data generation is performed by fitting a set of parametric equations to the data sets [Picone et al. 2002].

The NRLMSISE-00 model was a great upgrade from the previous models for a number of reasons. Firstly, it not only used the newly collected data from different space missions but also used the data sets the previous models used. This gave it a wider range of possible values to analyse and create a model that fits the data better. Additionally, the temperature data range, and accuracy, were also improved. The temperature model plays a key role in the NRLMSISE-00 model as the temperature is linked to solar activity and it affects almost all components of the atmosphere while also creating significant chemical changes in the composition of such [Litvin et al. 2000]. Finally, dependency on the geomagnetic activity has been added to the NRLMSISE-00 model.

However, like every model, the NRLMSISE-00 model also has its limitations. One of the main limitations is the altitude at which reliable data can be used. As the altitude gets higher, the number of data points decreases significantly. This means that the accuracy of the model will decrease. Above the 800-1200 km the data points become scarce. This does not necessarily affect the project at hand, but if extensions of the analysis to higher altitudes want to be made it should be taken into account. Additionally, when the geomagnetic activity is high, data points decrease. This will limit the accuracy of the atmospheric model if there are moments in time of high geomagnetic activity. Furthermore, another source of error is the use of $F_{10.7}$ as a proxy for the solar UV flux.

Finally, since the first release of the NRLMSISE-00 model, a new model has been released. The new release, in 2020, called NRLMSIS 2.0 is an improvement on the NRLMSISE-00 version. The new version is, in theory, more accurate due to the increase in the data collected since 2000. However, it should be pointed out that most of the major changes are performed for the altitudes below 100 km [Emmert et al. 2021]. As the project only focused on altitudes above 120 km, there was no benefit in implementing the newer model.

2.3.2. Thermospheric Winds

The next aspect that will be talked about is the thermospheric winds and their effect on orbit calculations. The thermospheric winds play a critical role in the modelling of the thermosphere and, when possible, should be taken into account. The physics behind the behaviour of thermospheric winds will not be covered in this study, as they are not the main focus. For the interested reader, Rishbeth [1993] provides an introduction to the mathematical equations governing thermospheric winds. For the current project, the main focus is the effect of these winds on the relative velocity of the satellite with respect to the atmosphere and the aerodynamic coefficients of the object. Thus, the first aspect to understand is the flow of the winds.

Thermospheric winds tend to flow from high-pressure to low-pressure regions of the atmosphere. This means that it is expected to see an influence of the Sun's activity on the magnitude of the winds. The two most influential factors are the day-to-night changes in temperature, which results in a wind flow from the day side to the night side, and the summer to winter regions flow. Additionally, geomagnetic activities also play an important role in the thermospheric winds. Due to the amount of energised particles that enter through the poles they affect the wind flow and create a flow from higher to low latitudes [Forbes 2007]. This new flow also interacts with the day-to-night circulation previously mentioned. The combined effect of both causes could enhance or lessen each other. Thus, it cannot be said that the thermospheric winds depend on the Local Solar Time (LST), Day Of Year (DOY), latitude and geomagnetic activity.

The second aspect to understand is the magnitude of such winds and how to model them. Measurement of thermospheric winds is rather complicated. Usually, a very precise onboard accelerometer is required to measure non-gravitational accelerations. Then, processing of the data needs to be performed to retrieve information about the thermospheric winds. Another very common method is to use very precise orbit determination [March 2020]. A number of missions have been used to generate thermospheric wind data. From the CHAllenging Mini Satellite Payload (CHAMP) mission, which started in the 2000s, to the new Swarm mission, which is currently running, different measurements can be made. Additionally, on ground-based 630 nm Fabry-Perot Interferometer (FPI) and Incoherent Scatter Radar measurements can also be used [Drob et al. 2015].

In order to use this data, a number of thermospheric wind models have been created. The most common one is the Horizontal Wind Model (HWM). The latest version is the HWM14 takes into account the data from GOCE as well as some new FPI data. In the HWM14 the maximum horizontal wind that can be expected at an altitude of 300 km is 500 $\mathrm{m\,s^{-1}}$. For reference, assuming an orbital velocity of 7.5 $\mathrm{km\,s^{-1}}$,an across-track wind of 500 $\mathrm{m\,s^{-1}}$ would generate a sideslip angle of about 3.8°. This sideslip angle could increase the C_D of a satellite by 5% or more depending on the shape of the satellite [Toonen 2021].

Additionally, it should be noted that the thermospheric winds also change the relative velocity of the object with respect to the atmosphere. This means that the thermospheric winds not only have an effect on the aerodynamic coefficients of the object but also have a direct effect on the drag force experienced by the satellite, as seen by the V factor in Equation (2.1). Toonen [2021] found that in the free molecular flow regime these changes in velocity could account for an increase, or decrease, of the drag force by up to 10%. Thus, for this project, a thermospheric wind model was implemented. The HWM14 was implemented in Python and linked to TUDAT, as will be explained in Section 7.1.

2.3.3. Aerodynamic modelling

Finally, the last topic of interest is aerodynamic modelling. The aerodynamic modelling of an object in orbit is key in order to have a realistic behaviour of the object in orbit. This section is rather brief as it will be explained in more detail in Chapter 5 but relevant enough to add it here. It will consist of three main topics, the analytical solution for the calculations of the shear and pressure coefficients in the free molecular flow regime, the use of SPARTA and the reflection model of particles in the free molecular flow regime.

Firstly, it was found that there are analytical solutions to the shear and pressure coefficients in the free molecular flow regime. These were developed by Sentman [1961] and Chambre and Schaaf [1961] and relate the pressure and shear coefficients to the speed ratios of molecules in the atmosphere. This research has been implemented in Toonen [2021], Doornbos [2011] and March [2020] in order to verify their results. The results from the analysis will be further explored in Chapter 5 but they looked promising.

The second important aspect was the use of SPARTA. All three previously mentioned theses use SPARTA for their simulations. Inputs, settings and expected outputs are also analysed, sensitivity analyses are carried out and recommendations are given. All this information has been noted and will be applied when required in this project. Additionally, Toonen [2021] also used SPARTA for the transition regime analysis in the lower atmosphere, at altitudes of around 120 km. This is very interesting as the transition regime is a regime where there are no analytical expressions to properly model the aerodynamic behaviour. Thus, having information on expected results and what were some of the challenges found when analysing that regime is really useful. Finally, it is important to point out that the reader created by Hładczuk [2022] provides very interesting information on how to set the simulation parameters, as well as an explanation of how to apply a simulation ”trick” for the calculation of the aerodynamic coefficients.

Finally, the last aspect to be introduced is the accommodation and reflection model of particles in the free molecular flow regime. As will be seen in Chapter 5 it is of key importance to select the correct reflection model and accommodation coefficient. The effect on the aerodynamic coefficients is highly dependent on these values. As it is shown by March [2020] and March et al. [2021] the selection of values of the accommodation coefficient can be very complicated, and the results could vary by a lot.

2.3.4. Conclusion

Three main conclusions are reached from the research on previous studies. Firstly, the importance of the atmospheric model and the parameters that affect said model. It is of key importance to be able to model the atmosphere as accurately as possible. In order to do so, the previously mentioned NRLMSISE-00 model will be implemented. Next, the influence of the thermospheric winds is significant and should be taken into account. The changes in velocity not only affect the drag force directly but also the C_D coefficient. An increase of 10% was found on the drag force and of 5% on the drag coefficient [Toonen 2021]. Thus, for this project, it has been decided that these percentages are high enough to take them into account. The atmospheric winds will be modelled using the HWM14 model.

Finally, it is noted that SPARTA and the analytical method for analysis of the free molecular flow regime are worth implementing. The results from the previous studies show that SPARTA provides results which have been verified and validated with other literature. The same applied to the analytical method. Thus, the implementation of these techniques will be applied in this project. It should also be noted that SPARTA seems to produce results in the transition regime that agree, with good accuracy, with experimental results, while the analytical method starts to deviate. Thus, SPARTA will be used for the transition regime modelling.

3

Case Study

One of the most important aspects of this, and any, project is to be able to apply the different aspects that are to be investigated and analyse the results consistently. To do so, it is important to a set of requirements and a reference mission. This is done in order to have a benchmark to be able to have consistency when looking at the results. Consistency is key as otherwise it would be impossible to assess the effect of the different sources of error in the mission. In this chapter, the requirements for the project are first introduced in Section 3.1. Once the requirements are known, a reference mission which fits those requirements is explained in Section 3.2.

3.1. Requirements

As previously mentioned, requirements are key for a project as they provide a clear and comprehensive understanding of what needs to be achieved by the project. The requirements set in this section help define the scope of the project, its limitations, purpose and goals. In this section, the requirements that have been derived from the literature study will be presented and explained. In Section 3.1.1 the orbital requirements are introduced. This is then followed by the different model requirements in Section 3.1.2. Finally, in Section 3.1.3 the initial aerodynamic requirements are shown.

3.1.1. Orbit Requirements

In this subsection, the orbit requirements are presented.

- **REQ-ORB-01**: The orbit shall have an apogee altitude smaller than 300 km.
- **REQ-ORB-02**: The orbit shall not have an altitude lower than 120 km.
- **REQ-ORB-03**: The orbit shall not have an eccentricity of more than 0.01.
- **REQ-ORB-04**: The orbit shall have any inclination in the range of 0 ° $\leq i \leq$ 180 °

The altitude range for the analysis of the mission has been chosen to be between 120 km and 300 km. This altitude range for the analysis has been chosen for a number of reasons. Firstly, the lower bound has been chosen as at that altitude the object is considered to start the re-entry phase due to the high atmospheric drag [King-Hele 1964]. As for the higher bound, it was chosen after analysing different aspects. To begin with, special attention was paid to the orbit decay time. It would be desired to keep the propagation time to a minimum. This is due to the fact that while propagating the orbital decay one needs to use models, such as atmospheric and thermospheric wind, that rely on predictions of solar and magnetic activity. The prediction of these parameters is not very accurate. For instance, as seen in Labonville et al. [2019] the predictions of when the new solar cycle maxima will be differed by up to 4 years depending on which method is used. Due to this, a small altitude which results in a time frame of at most a couple of weeks, preferably days, for the propagation is desired. It was thus decided to use an apogee bellow 400 km. This is also due to the fact that the orbital decay, assuming a low solar activity, for this altitude could be of more than 10 years. For example, ESA's ERS-2 which has an orbit of 570 km has an expected decay time of 15 years [Diekmann 2012].

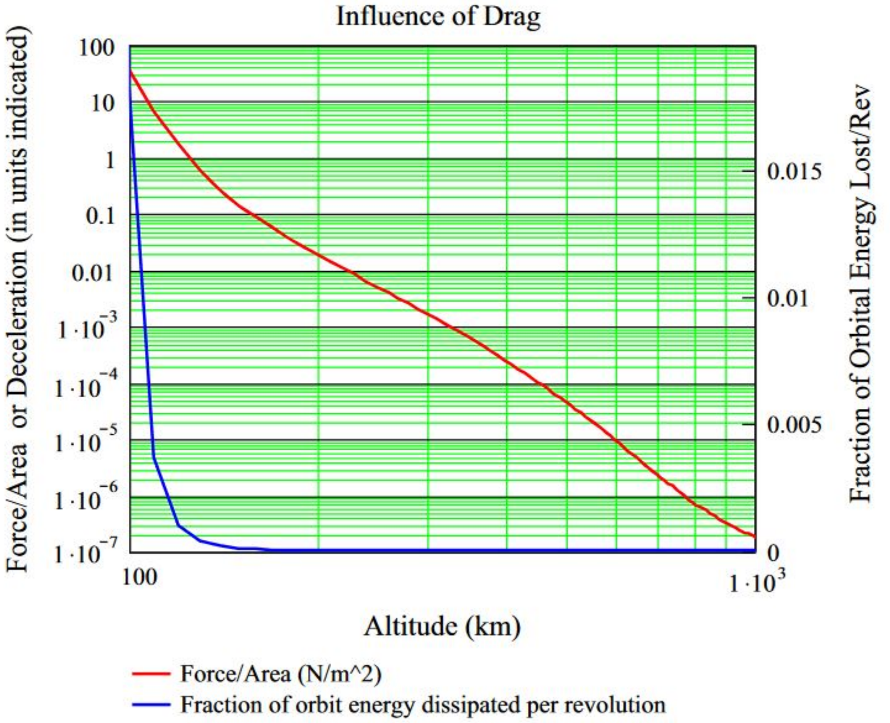

Figure 3.1: Influence of Drag for a 1000 kg satellite, 100 m^2 drag area, C$_D$ = 2.2 and Harris–Priester model atmosphere [Vallado and Finkleman 2014]

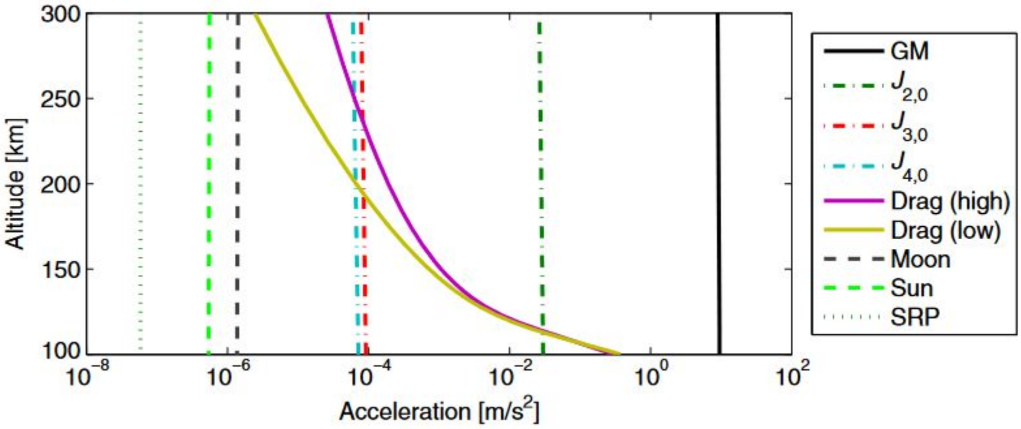

Figure 3.2: Perturbing forces on a Delta-K rocket stage [Ronse and Mooij 2014]

The other main reason to select the higher bound to 300 km is the effect of drag. After all, the project is interested in how the aerodynamic coefficients affect the decay of the object being analysed. Therefore, in order to choose 300 km Figure 3.1 in combination with Figure 3.2 are used. In Figure 3.1 the perturbing acceleration due to drag per m^2 and how it varies with altitude is shown, while in Figure 3.2 a wide variety of perturbing accelerations are shown. It can be seen that the main acceleration is, up to around 115 km, always due to the non-spherical gravitational terms of the Earth. However, just before the 300 km altitude the drag becomes the second main perturbing force. As the project is interested in the effect of aerodynamics, having drag as the second main perturbing acceleration was considered a good starting point for propagation. It is important to remember that the behaviour of the drag in Figure 3.1 is per m^2. Thus, if there is a large surface area the drag acceleration will increase significantly.

It should be pointed out that there could be further restrictions on the orbit, such as inclination. However, it was decided to not constrain other aspects in order to have a wider variety of possible missions to look into. As will be seen later on, the reference mission will constrain the project and generate new requirements.

3.1.2. Environment Requirements

In this section, the different models' requirements, such as atmospheric model, gravity and thermospheric wind are introduced and explained.

Earth's Gravitational Model

- **REQ-GRAV-01**: The gravity model shall be able to model the gravity field in the orbit altitude range (120 to 300 km).
- **REQ-GRAV-02**: The gravity model shall be able to model the gravity globally.
- **REQ-GRAV-03**: The gravity model shall be able to model gravitational perturbations which cause accelerations on the order of 1×10^{-7} m/s^2 or higher.

First of all, the requirements for the gravity model are given. The requirements for the altitude range and the location on Earth, **REQ-GRAV-01** and **REQ-GRAV-02**, can always be expected to be there. These two requirements are necessary in order to be able to fully describe the gravitational effect on the satellite at different points in orbit. Furthermore, the more detailed requirement of the perturbing accelerations, **REQ-GRAV-03** arises from the magnitude of the other perturbing accelerations. This can be seen in Figure 3.2 in which the perturbing accelerations are of magnitude 1×10^{-6} m/s^2 and above. Thus, by having a gravitational acceleration with an accuracy of an order of magnitude lower it will not neglect the effects of the other perturbing accelerations.

Earth's Atmospheric Model

- **REQ-ATMOS-01**: The atmospheric model shall be able to model the atmosphere in the orbit altitude range (120 to 300 km).
- **REQ-ATMOS-02**: The atmospheric model shall be able to provide the atmospheric composition at any altitude between 120 to 300 km.
- **REQ-ATMOS-03**: The atmospheric model shall be able to model the density of the atmosphere globally.
- **REQ-ATMOS-03-01**: The atmospheric model shall be able to model density variations at different latitudes and longitudes.
- **REQ-ATMOS-04**: The atmospheric model shall be able to model the density of the atmosphere for a range of F$_{10.7}$ between 50 and 480 sfu.
- **REQ-ATMOS-05**: The atmospheric model shall be able to model the density of the atmosphere for a range of a$_p$ between 0 and 400 nT.
- **REQ-ATMOS-06**: The atmospheric model shall be able to model the density of the atmosphere from November 10, 1957, to 30 days from the current date of analysis.

The atmospheric requirements come from the need to be able to model any orbit within the altitude range at any point in time. In order to fully achieve so, the six atmospheric requirements were generated. As previously mentioned, the NRLMSISE-00 model was used for this project. This is due to the fact that it can comply with all requirements presented in this section. It should be noted that there is not a precise date in **REQ-ATMOS-06**. This is due to the fact that the reference mission will have a number of different epochs of interest. These epochs have a wide range of values, thus generating a requirement for a precise range of dates could potentially result in not analysing important epochs. Thus, the epochs are fixed to those from the first initial epoch in the text file with the measured a$_p$ index to 30 days from the current date in which the analysis is carried out. Additionally, as will be seen later in Chapter 6, the density composition will be required in order to calculate the aerodynamic coefficients. This is the reason for **REQ-ATMOS-02** to be added to the requirement list.

Thermospheric Wind Model

- **REQ-TW-01**: The thermospheric wind model shall be able to model thermospheric winds in the orbit altitude range (120 to 300 km).
- **REQ-TW-01-01**: The thermospheric wind model shall be able to model thermospheric winds in northwards and eastwards directions from the position of the satellite.
- **REQ-TW-02**: The thermospheric wind model shall be able to model the winds globally.
- **REQ-TW-03**: The thermospheric wind model shall be able to model the winds for a range of a$_p$ between 0 and 400 nT.
- **REQ-TW-04**: The thermospheric wind model shall be able to model the thermospheric winds from November 10, 1957, to 30 days from the current date of analysis.

The thermospheric wind requirements come from the need to be able to model any orbit within the altitude range at any point in time. In order to fully achieve so, the four atmospheric requirements were generated. As previously mentioned, the HWM14 model was used. This is due to the fact that it can comply with all requirements presented in this section. Similarly to the atmospheric requirements, there is no precise date range in **REQ-TW-04**. The explanation follows that of the atmospheric model.

3.1.3. Aerodynamic Requirements

- **REQ-AERO-01**: The software shall be able to provide all six, three force and three moment, aerodynamic coefficients in a body frame reference system.
- **REQ-AERO-02**: The aerodynamic software shall be able to calculate the aerodynamic coefficient in the free molecular flow regime for Knudsen numbers above 10.
- **REQ-AERO-03**: The aerodynamic software shall be able to calculate the aerodynamic coefficient in the continuum flow regime for Knudsen numbers below 0.001
- **REQ-AERO-04**: The aerodynamic software shall be able to calculate the aerodynamic coefficients in the transition regime for Knudsen numbers between 0.001 and 10.
- **REQ-AERO-05**: The aerodynamic software shall be able to calculate the aerodynamic coefficients for a range of different input parameters.
- **REQ-AERO-05-01**: The aerodynamic software shall be able to calculate the aerodynamic coefficients for a range of angles of attack and sideslip angles.
- **REQ-AERO-05-02**: The aerodynamic software shall be able to calculate the aerodynamic coefficients for a range of atmospheric densities.
- **REQ-AERO-05-03**: The aerodynamic software shall be able to calculate the aerodynamic coefficients for a range of speed ratios between 1 and 14.

The aerodynamic requirements shown before are derived from a number of reasons. Firstly, **REQ-AERO-01** comes from the fact that all six coefficients are required to fully describe the effect of the aerodynamics on the object being analysed. Secondly, **REQ-AERO-02** and all its sub-requirements come from the fact that the aerodynamic analysis will have to be performed under different flow conditions. Finally, **REQ-AERO-03** arises because as the satellite will be experiencing different linear and angular accelerations, as well as altitude changes, different flight conditions will be experienced. Thus, it is important to be able to model nearly all possible flight conditions. In order to comply with this requirement, a database of all the coefficients under different conditions will be created. To create the database, a number of steps were taken, from the prediction of the densities to a sensitivity analysis of the behaviour of the coefficients to different inputs. The description of the creation of the database will be given in Chapter 6.

3.2. Reference Mission: Starlink Satellites

Now that the requirements of the project are clear, it is possible to look for a reference mission to use. It is of key importance to select the reference mission properly. This is due to the fact that the mission that is selected will be used to generate all the results from the project. If a mission that does not fit the goal of the project is chosen, the results could prove to not be of use. For this project, a number of possible missions were looked upon. From the research, it was concluded that the Starlink satellites were the best option.

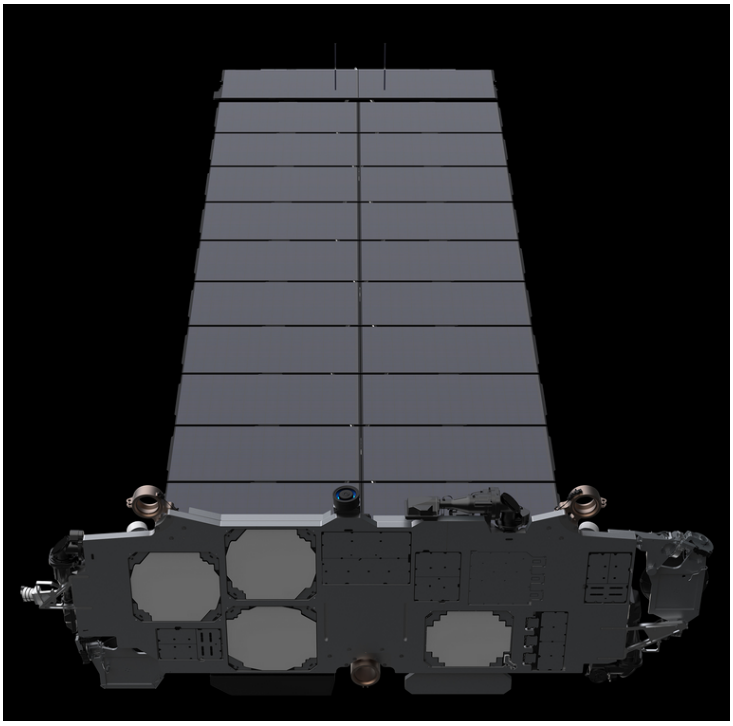

Figure 3.3: Starlink satellite as seen from below [1]

The Starlink constellation was first deployed in May 2019. As of 2023, there are more than 4,000 satellites in orbit. Each Starlink satellite has a mass of about 227-260 kg, depending on the version, and orbit between 340-1100 km in inclinations of 53°. There are a number of reasons for choosing this constellation.

Firstly, due to the large size of the constellation, there is a constant re-entry of satellites. This high number of re-entries allows for the opportunity to analyse more data. As the project focuses on the analysis of the satellite's last orbits before re-entering, a higher number of re-entries will result in a larger database to be used. This will prove useful as verification of the system can be performed using a larger number of samples. Additionally, this large number gives the project the opportunity to not only analyse and test previous re-entries but also allow for the prediction of future re-entries. It is key to be able to predict the re-entry of such numerous satellites due to the risk it poses to other satellites in the same altitude range.

Furthermore, there is the advantage that all satellites from the same generation have the same shape which means that the same model can be used in the predictions in SPARTA. This significantly reduces the effort required to analyse the satellite orbit as the same model can be used for multiple satellites at different times. Additionally, the shape of the Starlink satellite is rather interesting from an aerodynamic aspect. As can be seen in Figure 3.3 the shape of Starlink is like the letter L. It has a rather large solar panel in combination with a slender smaller body. This shape is interesting as it is possible that the Starlink starts to oscillate in a specific attitude due to the large solar panel acting as a stabilizer. It will be interesting to see the results and if there is a stable initial attitude for Starlink to oscillate around. Finally, the orbits of the Starlink satellites comply with the requirements set in the previous section. The TLEs that are selected for the analysis have an epoch smaller than 300 km to make sure that compliance with the requirements is achieved.

3.2.1. Starlink Sizing

As there is no official data on the dimensions of the Starlink satellite, the dimensions of the satellite have been taken from online sources. As will be seen later on, the actual shape of Starlink has been simplified in order to run SPARTA. The shape of Starlink has been simplified to two rectangles, which were named

---

[1] Source:`https://www.starlink.com/technology` (Last access: 15 April 2023)

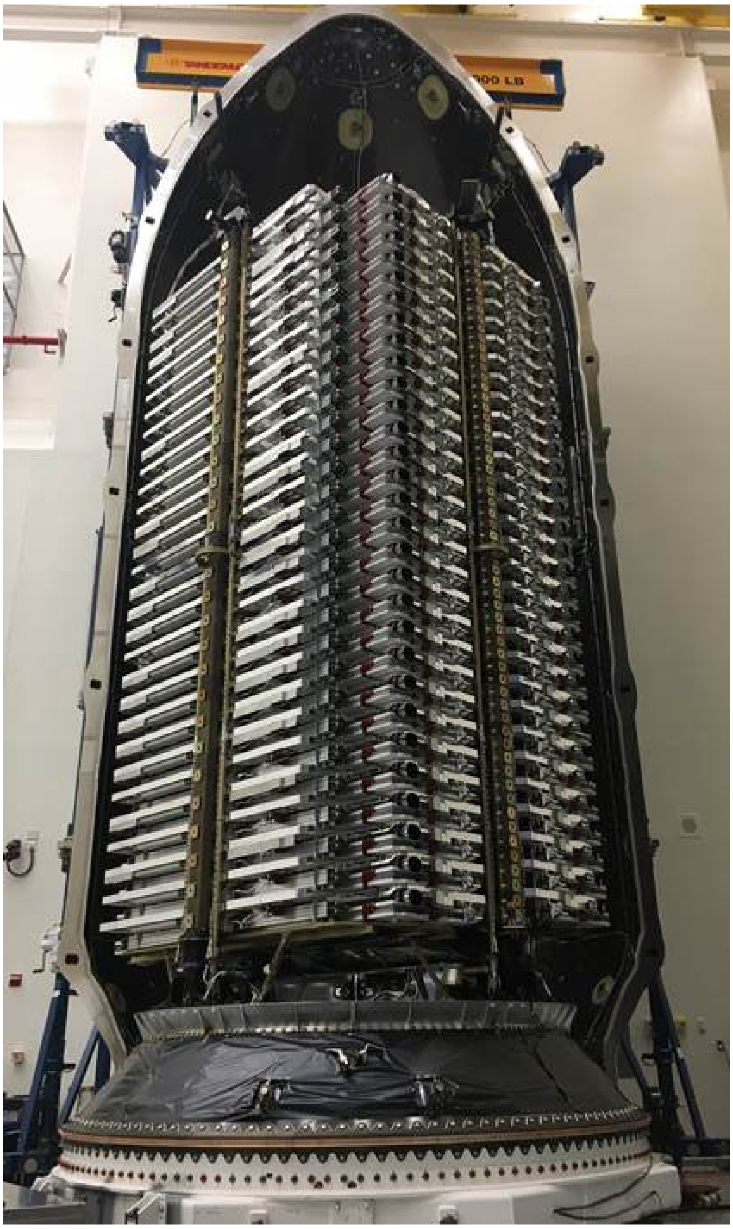

Figure 3.4: Starlink satellites loaded in a Falcon 9 [3]

the main body and solar panel. An explanation of how the dimensions were calculated is now given.

As it can be seen in Figure 3.4, the Starlink satellites are launched in a compact configuration to save space. In a single launch there are 60 satellites, and from the Falcon 9 manual[2] it is known that the height of the fairing of the Falcon 9 is of 6.7 m. Knowing that the satellites are stacked in pairs, it can be assumed that each satellite has a height of around 0.23 cm. This also accounts for the folded solar panel. Thus, it is decided to consider the height of the main body to be 0.2 cm. Additionally, it is also known that the fairing has a diameter for the payload of 4.6 m. However, it can be seen that there is some leftover space between the satellites and the fairing. Giving some room for error, say of 0.05 m, the satellite main body would have a dimension of 3.2 m by 1.6 m.

Next, the solar panel dimensions need to be estimated. As can be seen in Figure 3.3, the solar panels are composed of 24 segments, two alignments of 12. Assuming no borders, and an aspect ratio of 2 to 1, it can be approximated that each segment has a dimension of 1.6 m by 0.8 m. This means the final dimensions of the solar array would be 3.2 m by 9.4 m. The thickness of the solar panel is very hard to estimate. This is due to the fact that there is a lot of information lacking. However, as will be seen later on, a thickness is required in order to generate the mesh to input into SPARTA. Thus, it was decided to set a thickness of 0.02 m. This thickness was taken from literature as an initial estimate to the thickness of the solar panel.

---

[2] `https://www.spacex.com/media/falcon-users-guide-2021-09.pdf` (Last access: 17 April 2023)

[3] Source:`https://www.spacex.com/media/falcon-users-guide-2021-09.pdf` (Last access: 15 April 2023)

Finally, it is important to distribute the mass. As it was previously mentioned, the mass of the satellite is of 260 kg. From the previous dimensions, it is known that the solar array area is of 30.08 m^2. From Spectrolab[4], a manufacturer of solar panels for satellites and other space applications, the solar panels have a mass of 2.08 $\mathrm{kg\,m^{-2}}$. This means that the solar panel would have a mass of 62.6 kg. Assuming the rest of the mass is in the main body, the main body would have a mass of 197.4 kg.

---

[4] `https://www.spectrolab.com/photovoltaics.html` (Last access: 17 April 2023)

4

Satellite Dynamics

To be able to model the dynamics of the satellite in the atmosphere properly, it is necessary to understand the behaviour of the satellite. In this chapter, an introduction to Keplerian elements will be given in Section 4.1. This is then followed by an introduction to TLE data in Section 4.2. Then, the definition of reference frames and transformation of reference frames that will be required is given in Section 4.3. Along with the reference frames, Section 4.4 provides the definition of quaternions and their applications to orbit propagation. These previous sections will provide key understanding to be able to apply the Equations of Motion (EoM), which are introduced in Section 4.5. It is important to note that as the object in orbit is assumed to have six degrees of freedom, both the translational and rotational EoM are presented. Additionally, the perturbations which affect the EoM and will be taken into account in the project are also presented in the last section.

4.1. Keplerian Elements

The first way to describe the state of an object in orbit that will be explained is the Keplerian elements. It is important to have the Keplerian elements introduced here as they will be required further on. This is due to the fact that TLE data will be used to find the initial state of the object that will be propagated and said TLE data provides the information in Keplerian elements. It is thus important to have a brief notion of them. The state of the satellite can be described by the orbital elements. The elements required to define the position and velocity of a satellite in orbit are:

- e: eccentricity (0 $\leq$ e $<$ 1)
- a: semi-major axis (a > R_E)
- i: inclination (0° $\leq$ i $\leq$ 180°)
- ω: argument of pericenter (0° $\leq \omega$ < 360°)
- Ω: longitude of ascending node (0° $\leq \Omega$ < 360°)
- M: mean anomaly (0° $\leq \theta$ < 360°)

A visual representation of the first three elements can be seen in Figure 4.1 while the last three elements can be seen in Figure 4.2. Each of the Kepler elements can be related to each other by a series of equations shown in Wakker [2015]. For the purpose of this project, only elliptical and circular orbits will be considered, as the other two types of orbits do not orbit Earth but rather pass through it during its trajectory.

4.2. Two-Line Element

In order to be able to analyse the different dynamics of a satellite, or object in orbit, it is first necessary to know its orbital information. To do so, there are a number of different options that can be implemented, such as finding the object passing through the sky and measuring and analysing its different parameters. Another option is to look up the object in a database, or catalogue, where different objects in orbit are recorded. This is where the TLE data comes into play and thus will now be explained.

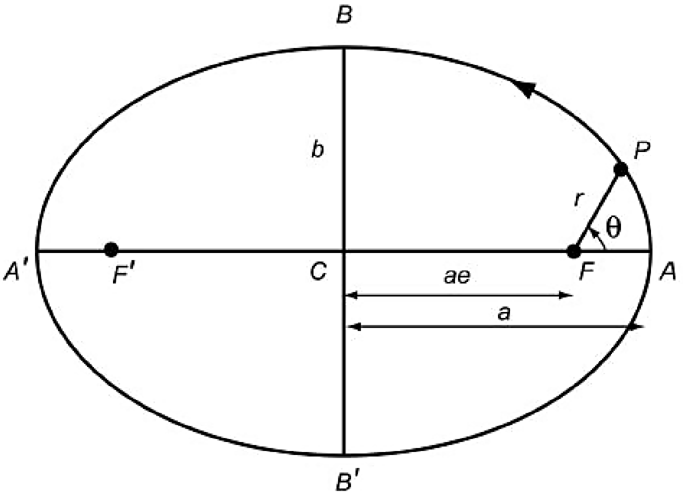

Figure 4.1: Geometry of an elliptical orbit [Wakker 2015]

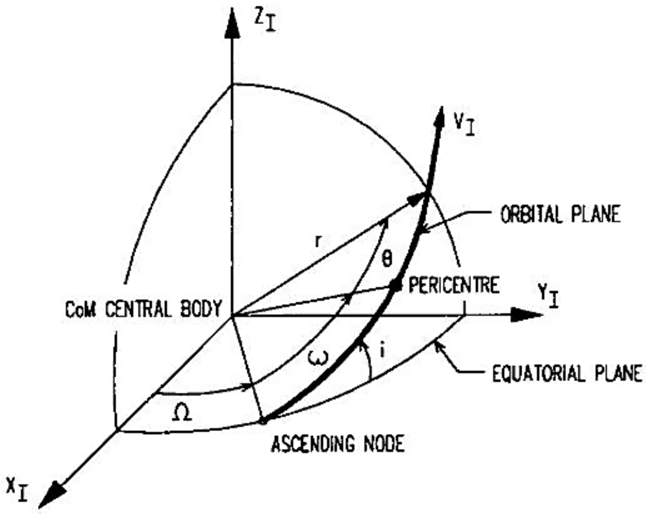

Figure 4.2: Definition of the orbital parameters ω, Ω and i [Mooij 1994]

This section will focus on TLEs. Firstly, what is a TLE is and how it is generated is given in Section 4.2.1. Then, in Section 4.2.2, a discussion of why TLEs are of interest for this project is given. It should be noted that, as with any other measurement, TLEs also have errors. An analysis of the different methods to process the TLE data and the errors and limitations this data type has will be performed in Section 7.5.

4.2.1. Generation of TLE

TLEs have been generated since the 1960s by the United States Strategic Command (USSTRATCOM) and they contain information on the orbit of the object of interest. The TLE have two lines of 69 characters each which contain the Keplerian elements and force model parameters of a given object. In Figure 4.3 a TLE example is given. For our project, the most interesting aspects of the TLE are the epoch, which is the fourth value of the first row, and the Keplerian elements of the orbit, which are the third to seventh values of the second row. These values are required to generate the initial state of the satellite. Additionally, in the results section, the calculated value of the ballistic coefficient of the simulation will be compared to the ballistic value of the TLE, which is the seventh value of the first row.

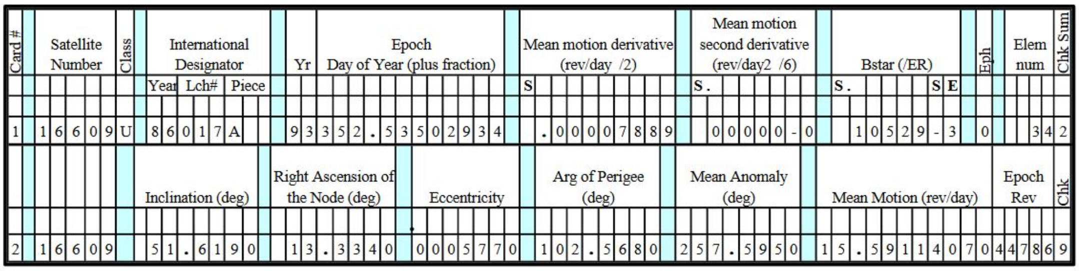

Card #	Satellite Number	Class	International Designator	Yr	Epoch Day of Year (plus fraction)	Mean motion derivative (rev/day /2)	Mean motion second derivative (rev/day2 /6)	Bstar (/ER)	Eph	Elem num	Chk Sum
			Year Lch# Piece			S	S .	S . S E			
1	16609	U	86017A	93	352.53502934	.00007889	00000-0	10529-3	0	34	2

		Inclination (deg)	Right Ascension of the Node (deg)	Eccentricity	Arg of Perigee (deg)	Mean Anomaly (deg)	Mean Motion (rev/day)	Epoch Rev	Chk
2	16609	51.6190	13.3340	0005770	102.5680	257.5950	15.59114070	44786	9

Figure 4.3: Example of TLE with descriptions of data fields [Vallado and Cefola 2012]

Of course, in order to obtain this data for a number of objects in orbit around Earth a specific and very standardised process needs to be followed. Such a process will now be explained. To generate the Keplerian elements and the force model parameters, an orbital model is used. In the case of LEO objects, the most common model is the Simplified General Perturbations 4 (SGP4) propagator. The SGP4 propagator is a simplified propagator in which instead of selecting a number of perturbations, a single perturbation is used. This perturbation has been generated by fitting thousands of different satellite decays over the years. As can be expected, this results in the SGP4 propagator having a number of errors, which, for instance, can cause a satellite to have a negative ballistic coefficient. For this project, the SGP4 is used only once to verify and validate the software generated in this thesis. For more information on the SGP4, the reader is directed to Hoots et al. [1980]. By fitting the SGP4 model to the tracking data it is possible to estimate the Keplerian elements and force parameters of the object. It should be noted that if the trajectory of the object from the TLE data wants to be reconstructed, the SGP4 model will have to be used [Vallado and Crawford 2008].

4.2.2. TLE Applications and Errors

Now that TLEs are explained it is important to mention why they are of relevance to the project at hand. In the current project, an object in orbit is propagated in time. In order to do so an initial state is required, both translational and rotational. As will be seen later on, one of the best methods for finding this initial state is to use TLE data. This is due to the fact that there not only exists a wide range of TLE data but TLE data is also updated at regular intervals. As it has been previously explained the TLE are generated using observations and an orbit propagation model. It can thus be expected that there are some errors in the TLE data and in the state they represent. This subsection will talk about such errors, what can be expected and their magnitude.

To begin with, Alarcón et al. [2005] found that in general the expected accuracy of TLE data is two orders of magnitude worse than real-time data. These results mean that it is necessary to analyse and quantify the errors in TLE data in order to be able to take them into account in orbit propagation. Doornbos [2011] performed an analysis on the TLE errors for the altitude of a satellite when compared to real-time data from the satellite. The results showed that the best-case scenario gave an altitude error of just below 200 m. And the worst-case scenario was a position error of more than 400 m. These results are in agreement with Alarcón et al. [2005]. Adding to these results, Boyce [2004] analysed the accuracy of TLE data against precise ephemerides data and found the TLE accuracy was about 100 m. Furthermore, it is important to also take into account the effect of the SGP4 propagator. Hartman [1993] found that the SGP4 propagator could be used only for a few days. These results come from using the SGP4 propagator and comparing results to TLE data in order to determine when the propagation error was more than 25 km.

Overall, it can be seen that the TLE are not the most precise method to use for the generation of the initial state of an object in orbit. However, as they are the most common data it is often used and a number of studies have been performed. Due to the previous research on TLE accuracy, it is possible to generate an error matrix such that a sensitivity analysis of the errors can be performed. Additionally, it is possible to reduce the errors in TLE data if compared to more accurate data, such as the GPS data of GOCE [Hoogendoorn et al. 2018]. A more detailed explanation of the error generation for TLE data will be given in Section 7.5.

4.3. Reference Frames

To fully describe the EoM it is necessary to understand the reference frames which could be potentially involved. Thus, in Section 4.3.1 an introduction to all possible required reference frames are given. It should be pointed out that all reference frames are right-handed. Finally, in Section 4.3.2 the transformation equations between different frames are given. These transformations will be key to being able to analyse the different forces on the system in a global reference frame.

4.3.1. Different Reference Frames

The following reference frames will be considered. These frames are defined as per Mooij [1994].

- **Celestial Reference Frame** [McCarthy et al. 1989], designated by C.

  This inertial frame is centred at the barycentre of the solar system. The X$_C$-axis points towards the vernal equinox. The Y$_C$-axis lays on the same plane as Earth's orbit around the Sun. Finally, the Z$_C$-axis completes the right-handed system.

- **Inertial Planetocentric Reference Frame**, designated by subscript I.

  The inertial frame has its origin located at the Center of Mass (CoM) of the central body. The Z$_I$-axis points north and coincides with the rotational axis of the central body. The reference meridian, which determines the direction of the X$_I$-axis, is defined by the zero longitude meridian at zero time. Finally, the Y$_I$-axis completes the right-handed system.

- **Rotating Planetocentric Reference Frame**, designated by subscript R.

  The rotating frame is fixed to the central body and it coincides with the inertial frame at zero time. Thus, the Z$_R$-axis points towards the north and is aligned with the rotation axis of the central body. The X$_R$-axis intersects the equator at zero longitude, and the Y$_R$-axis completes the system.

- **Vertical Reference Frame**, designated by subscript V.

  The origin of the vertical reference frame coincides with the CoM of the satellite and the Z$_V$-axis points towards the CoM of the central body, along the radial component of the gravitational acceleration. The X$_V$-axis is perpendicular to Z$_V$ and points to the northern hemisphere. Finally, the Y$_V$-axis completes the right-handed system.

- **RSW Reference Frame**.

  The RSW frame is similar to the Vertical frame but the axes are defined differently. The origin is located at the CoM of the satellite and the R-axis points opposite to the vector joining the CoM of the Earth and that of the satellite. The S-axis is perpendicular to the R-axis and in the direction of motion. This means that the S-axis does not always coincide with the velocity of the satellite, only in a circular orbit. Finally, the W-axis is normal to the orbital plane.

- **Body Reference Frame**, designated by subscript B.

  The body frame is fixed to the satellite, with the origin being located at the CoM of the satellite. For this reference frame, it is assumed that the XZ plane is a plane of symmetry on which the X$_B$-axis lies. The X$_B$-axis is defined as positive in the forward direction. The Z$_B$-axis also lies on the XZ plane of symmetry but is defined as positive downwards. Finally, the Y$_B$-axis completes the right-handed system.

- **Aerodynamic Reference Frame**, designated by subscript A.

  Similar to the body frame the origin of the aerodynamic frame is located on the CoM of the satellite. The X$_A$-axis points in the direction of airspeed relative to the atmosphere. The Z$_A$-axis points opposite to the aerodynamic lift force and the Y$_A$-axis completes the right-handed system.

It should be noted that the inertial frame is not a true inertial frame, it is a pseudo-inertial frame due to the motion of the central body. However, since this rotation of the central body only has a marginal effect on the results, it can be assumed to be inertial. Additionally, for the J200 frame, the X_I-axis is not aligned with the zero longitude meridian. There is a small offset that needs to be taken into account.

An explanation of why these frames are used is now given. Firstly, the celestial reference frame will be used to determine the position of the satellite with respect to the Sun. This position is required for the solar radiation pressure acceleration acting on the satellite. Then, the inertial frame is required for the EoM to be defined. Following this, the rotating planetocentric frame is required to know the position of the satellite with respect to the surface of Earth. Next, the vertical frame will be used to introduce the HWM14 thermospheric winds to the propagation. Furthermore, the RSW frame is required to generate the initial TLE errors. Finally, the body frame and aerodynamic frame are closely linked and are required for the generation of the aerodynamic coefficients.

4.3.2. Frame Transformation

Once the reference frames have been defined it is important to define how to change from one reference frame to the other. The relations for such transformation can be defined by unit axis rotation, which can be seen in Equations 4.1 to 4.3. Each one of these matrices corresponds to the rotation around the X, Y and Z-axis respectively.

$$\mathbf{C}_1(\theta) = \begin{bmatrix} 1 & 0 & 0 \\ 0 & \cos\theta & \sin\theta \\ 0 & -\sin\theta & \cos\theta \end{bmatrix} \tag{4.1}$$

$$\mathbf{C}_2(\theta) = \begin{bmatrix} \cos\theta & 0 & -\sin\theta \\ 0 & 1 & 0 \\ \sin\theta & 0 & \cos\theta \end{bmatrix} \tag{4.2}$$

$$\mathbf{C}_3(\theta) = \begin{bmatrix} \cos\theta & \sin\theta & 0 \\ -\sin\theta & \cos\theta & 0 \\ 0 & 0 & 1 \end{bmatrix} \tag{4.3}$$

Before this section continues, it is important to note that these frame transformations apply only if the transformation is a so-called reference-frame rotation. This is the case for all TUDAT transformations. However, for transformations in SPARTA, the so-called body rotations are used. This will be explained in Section 6.4 to avoid confusion.

These unit-axis rotation matrices have a couple of properties that are of interest to us. First of all, if more than one rotation around a different axis occurs it is possible to simply write the resulting transformation as a combination of the matrices. Furthermore, as each of the $\mathbf{C}_1$, $\mathbf{C}_2$, and $\mathbf{C}_3$ are orthonormal the product is also orthonormal. This means that the inverse of the matrix is the transpose. This, in turn, means that the transformation matrix from reference frame A to reference frame B is the transpose of B to A. Such property is illustrated by:

$$\mathbf{C}_{B,A} = \mathbf{C}_{A,B}^{-1} = \mathbf{C}_{A,B}^{T} \tag{4.4}$$

Using the previously mentioned equations in a specific order it is now possible to derive the transformations between frames which might be required. The following transformations have been taken from Mooij [1994].

Rotating planetocentric to inertial planetocentric

By definition, the rotating and the inertial planetocentric frame coincide when t=0. For this project, this is at J2000. As time goes by, the central body will rotate will an angular velocity ω_{cb} around the Z-axis. Thus, after a given time t, the angle rotated by the central body is $\omega_{cb}t$. Using the unit rotation matrix for the Z-axis the transformation matrix between the rotating to inertial planetocentric is described by Equation (4.5) and can be visualised in Figure 4.4.

$$\mathbf{C}_{I,R} = \mathbf{C}_3(\omega_{cb}t) = \begin{bmatrix} \cos\omega_{cb}t & -\sin\omega_{cb}t & 0 \\ \sin\omega_{cb}t & \cos\omega_{cb}t & 0 \\ 0 & 0 & 1 \end{bmatrix} \tag{4.5}$$

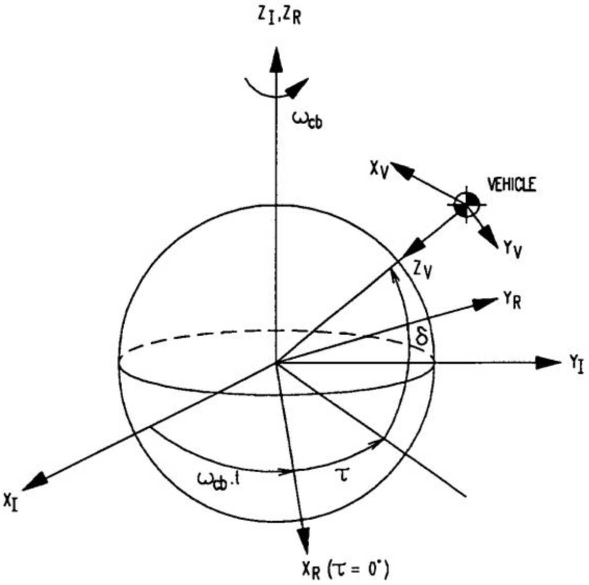

Figure 4.4: Relation between the inertial and rotating planetocentric frames and the vertical frame [Mooij 1994].

Vertical to rotating planetocentric
The rotating planetocentric reference frame and the vertical frame are related by two variables, the latitude, δ and the longitude, τ. The latitude is measured from the equator to the poles, positive in the north direction (−90 ° $\leq \delta \leq$ 90 °). The longitude is measured positively to the East from the prime meridian (−180 ° < τ < 180 °). As there are two variables that represent rotation on the Z and Y axes two of the unit axis transformations will be used for the final transformation. The transformation can be visualised in Figure 4.4 and the rotation matrix is given by:

$$\mathbf{C}_{R,V} = \mathbf{C}_3(-\tau)\mathbf{C}_2(\delta + \frac{\pi}{2}) = \begin{bmatrix} -\cos\tau\sin\delta & -\sin\tau & -\cos\tau\cos\delta \\ -\sin\tau\sin\delta & \cos\tau & -\cos\delta\sin\tau \\ \cos\delta & 0 & -\sin\delta \end{bmatrix} \tag{4.6}$$

Body to aerodynamic frame
The transformation between the body frame and the aerodynamic one depends on two variables, the angle of attack, α, and the sideslip angle β. The angle of attack is defined as positive for "nose up" attitude (−180 ° $\leq \alpha \leq$ 180 °). The sideslip angle is defined as positive for a "nose left" attitude (−90 ° $\leq \beta \leq$ 90 °). Once again, as there are two variables, two-unit axis transformations are used. First, one for the rotation around the Y-axis, caused by the angle of attack, and a second one for the rotation around the Z-axis due to the sideslip angle. The transformation matrix is given by:

$$\mathbf{C}_{A,B} = \mathbf{C}_3(\beta)\mathbf{C}_2(-\alpha) = \begin{bmatrix} \cos\alpha\cos\beta & \sin\beta & \sin\alpha\cos\beta \\ -\cos\alpha\sin\beta & \cos\beta & -\sin\alpha\sin\beta \\ -\sin\alpha & 0 & \cos\alpha \end{bmatrix} \tag{4.7}$$

Inertial to body frame
The last of the transformations that will be looked into is inertial to the body frame. This is due to the fact that it is necessary to have a transformation from the satellite frame to the inertial frame being used. For such a transformation three parameters are used. These are the yaw angle, Ψ, the pitch angle, θ, and the roll angle, ϕ. These first two angles are defined similarly to the aerodynamic ones, the angle of attack and the sideslip angle. However, instead of being with respect to the velocity vector, it is with respect to the inertial reference frame. Thus, the yaw angle is defined positively for a "nose right" attitude (−180 ° $\leq \Psi$ < 180 °) and the pitch angle is defined positively for a "nose up" attitude (−180 ° $\leq \theta$ < 180 °). As for the roll angle, it is defined as the rotation along the X$_B$-axis with a positive roll to the right. As there

are three transformations to take into account, three-unit matrices will be used. The final transformation matrix is the following:

$$\mathbf{C}_{B,I} = \mathbf{C}_1(\phi)\mathbf{C}_2(\theta)\mathbf{C}_3(\Psi) \tag{4.8}$$

4.4. Quaternions

This section focuses on quaternions. So far, all reference frames are based on Cartesian coordinates, which work great for translational parameters, such as position and velocity. However, to define attitude and rotation rates, a different notation is used. There are a number of different formulations for the attitude and rotation, such as the unified state model, the Rodrigues parameters and quaternions. For this project, quaternions were chosen. The reason for choosing quaternions is that quaternions do not have any geometric singularity and have a simple form. Additionally, quaternions are the standard propagator for the rotational model of TUDAT. The constraint that is presented is that quaternions need to be normalized. However, due to the use of numerical integration, small noise will be generated. This means that a solution needs to be found. The two most common ones are, to add a correction factor in the differential equation or to normalise the state after every integrator step [Dirkx and Mooij 2019]. As will be seen in Chapter 7, the quaternions in TUDAT are normalised after every integration step. Thus, that is what will be used for the current project. The quaternions are defined as follows [Mooij 1994]:

$$\begin{aligned}
q_4 &= \frac{1}{2}\sqrt{1 + \mathbf{C}_{I,B}(1,1) + \mathbf{C}_{I,B}(2,2) + \mathbf{C}_{I,B}(3,3)} \\
q_1 &= \frac{1}{4q_4}\left[\mathbf{C}_{I,B}(2,3) - \mathbf{C}_{I,B}(3,2)\right] \\
q_2 &= \frac{1}{4q_4}\left[\mathbf{C}_{I,B}(3,1) - \mathbf{C}_{I,B}(1,3)\right] \\
q_3 &= \frac{1}{4q_4}\left[\mathbf{C}_{I,B}(1,2) - \mathbf{C}_{I,B}(2,1)\right]
\end{aligned} \tag{4.9}$$

The quaternions shown here represent and define the attitude of the body frame with respect to the inertial planetocentric. This is the starting step to defining the initial rotational state of the object in orbit. In case a different set of parameters wants to be used to define the quaternions or to find a set of angles, for instance, the aerodynamic angles, a frame transformation will have to be performed. However, as the input for the software is the three Euler angles, pitch, yaw and roll, the inverse of the Equation (4.8) will be used. To find the relation between Euler angles and the quaternions, the following relation is used [Mooij 1994]:

$$\mathbf{C}_{I,B} = \begin{bmatrix} q_1^2 + q_4^2 - q_2^2 - q_3^2 & 2\left(q_1 q_2 + q_3 q_4\right) & 2\left(q_1 q_3 - q_2 q_4\right) \\ 2\left(q_1 q_2 - q_3 q_4\right) & q_2^2 + q_4^2 - q_1^2 - q_3^2 & 2\left(q_2 q_3 + q_1 q_4\right) \\ 2\left(q_1 q_3 + q_2 q_4\right) & 2\left(q_2 q_3 - q_1 q_4\right) & q_3^2 + q_4^2 - q_1^2 - q_2^2 \end{bmatrix} \tag{4.10}$$

Once all the angles and transformations are properly defined it is then possible to propagate the rotational state. For each new propagated rotational state, it is then possible to find the new corresponding angles and the properties of such an angle. The rotational state can be propagated by integrating the following equation over the time period it spawns:

$$\begin{pmatrix} \dot{q}_1 \\ \dot{q}_2 \\ \dot{q}_3 \\ \dot{q}_4 \end{pmatrix} = \frac{1}{2}\begin{bmatrix} q_4 & -q_3 & q_2 \\ q_3 & q_4 & -q_1 \\ -q_2 & q_1 & q_4 \\ -q_1 & -q_2 & -q_3 \end{bmatrix} \begin{pmatrix} \omega_1 \\ \omega_2 \\ \omega_3 \end{pmatrix} \tag{4.11}$$

4.5. Equations Of Motion

Since the object that will be analysed in the project is in a state of motion it is important to be able to describe such a motion. To do so, the Equations of Motion (EoM) of the satellite are described in this section. There are two main sets of equations, the translational and the rotational EoM. In Section 4.5.1 the translational EoM are given. This is followed by Section 4.5.2 where the rotational EoM is provided. Finally, in Section 4.5.3 the environment and the perturbing forces acting on the satellite will be expanded on.

It should be noted that two main assumptions are used for this section. These two assumptions are performed in order to simplify significantly the EoM. These are taken from Mooij [1994]:

- The mass of the object will be constant. This is done in order to simplify the EoM and eliminate all the mass-varying terms from the equations.
- The object is assumed to be a rigid body. Thus, no internal changes in the configuration of the model will be modelled.

It is important to point out that the assumption about the constant mass might not hold in some cases. Some satellites will use propellant to compensate for the altitude loss over time. However, as the study focuses on the last stages of the mission, it will likely hold for most simulations.

4.5.1. Translational EoM

The movement of a satellite, or object, can be described by a set of equations based on Newton's second law. Such a law can describe the motion of an object in any reference frame. It should be noted that if the reference frame is rotating there would be an introduction of new forces which are apparent. For the project at hand, it was decided to use an inertial planetocentric reference frame to define the equations of motion. The reason to use this frame is that it is an inertial frame thus the apparent forces do not need to be taken into account. It should be noted that technically the inertial planetocentric frame is a pseudo-inertial frame because the Earth itself is under acceleration due to the Sun and moving through space. However, since this effect is minimal it can be assumed to be an inertial frame. The EoM can be expressed in Cartesian coordinates as follows:

$$\frac{d\mathbf{r}}{dt} = \dot{\mathbf{r}} \tag{4.12}$$

$$\frac{d\dot{\mathbf{r}}}{dt} = \ddot{\mathbf{r}} \tag{4.13}$$

where $\mathbf{r}$ is the position vector of the satellite, $\dot{\mathbf{r}}$ is the velocity vector of the satellite and $\ddot{\mathbf{r}}$ is the acceleration vector of the satellite. If we focus on the acceleration term, it can be divided into two main aspects. The first one is the gravitational acceleration due to the main body, in this case, Earth, and the second term of perturbing accelerations. It is then possible to write the acceleration equation caused by the gravity of an object as seen below:

$$\frac{d\dot{\mathbf{r}}^I}{dt} = \nabla U + \ddot{\mathbf{r}}^I_{pert} \tag{4.14}$$

where the superscript I represents the accelerations inertial frame. The perturbing accelerations and how to model them will be described on Section 4.5.3.

It should be noted that there are multiple different ways to describe the EoM. For this project, the Cartesian coordinates have been chosen. The reasoning behind this decision is linked to the choice of the propagator to use in TUDAT. As it will be seen in Section 7.4, there are different representations of the equations of motion and each representation can be propagated differently. The advantage of using the Cowell propagator for the Cartesian coordinates is that the whole state is propagated. While this might result in a less computationally efficient method it is very robust. Additionally, representing the EoM in Cartesian coordinates tends to be more intuitive to understand than using other representations.

4.5.2. Rotational EoM

In comparison to the translational EoM which describes the satellite movement the rotational EoM describes how the rotation of the satellite is affected by momentum perturbations. The general equation of rotational motion as given by Mooij [1994] can be seen in the following equation:

$$\dot{\boldsymbol{\omega}} = \mathbf{I}^{-1}\left(\mathbf{T} - \boldsymbol{\omega} \times \mathbf{I}\boldsymbol{\omega}\right) \tag{4.15}$$

where $\mathbf{I}$ is the inertia matrix of the satellite, which is represented around the body axes, and $\mathbf{T}$ are the external perturbation moments. The disturbance torques could be caused by a number of reasons, both externally and internally. The main disturbance torques that an object could potentially experience are the gravity torque, the aerodynamic toque, the gravity torque and the solar radiation pressure torque. In order to know which torques are of relevance for the project an analysis will have to be made on these torques, their magnitudes and their influences on the object. This will be done in the next section.

4.5.3. Perturbing Forces and Torques

As mentioned in the previous subsection there are some perturbing forces and torques that affect the satellite. These perturbations will be described in this subsection along with the different ways of modelling them.

Gravitational Field

The gravitational field of a planet is not a perfect sphere thus the acceleration deviates from that shown in Equation (4.14) as this equation assumes it is the gravitational acceleration of a point-mass. To model the uneven gravitational acceleration spherical harmonics can be used. The gravitational potential of the spherical harmonics can be described as did Montenbruck and Eberhard [2013]:

$$U = \frac{\mu}{r} \sum_{n=0}^{\infty} \sum_{m=0}^{n} \frac{R^n}{r^n} P_{n,m}(\sin\phi)\left(C_{nm}\cos(m\lambda) + S_{nm}\sin(m\lambda)\right) \tag{4.16}$$

$$C_{nm} = \frac{2-\delta_{0m}}{M}\frac{(n-m)!}{(n+m)!}\int \frac{s^n}{R^n} P_{n,m}\left(\sin\phi'\right)\cos\left(m\lambda'\right)\rho(s)d^3s \tag{4.17}$$

$$S_{nm} = \frac{2-\delta_{0m}}{M}\frac{(n-m)!}{(n+m)!}\int \frac{s^n}{R^n} P_{n,m}\left(\sin\phi'\right)\sin\left(m\lambda'\right)\rho(s)d^3s \tag{4.18}$$

where R is the mean equatorial radius, λ is the longitude and ϕ is the latitude. Next, the terms C_{nm} and S_{nm} are coefficients to describe the dependence on Earth's internal mass distribution which are known to a very high degree [Wakker 2015]. Finally, $P_{n,m}$ is the associated Legendre function. One of the main takeaways from the spherical harmonics perturbation is the fact that they depend on the position of the satellite with respect to the centre of the Earth. This means that a change of reference frames will have to be applied to transform such an effect into the correct inertial reference frame. Additionally, as found in the literature study, for the project a degree and order of 24 will be used. This is done in order to make sure the accelerations due to the individual coefficients of the spherical harmonics all have a magnitude of 2×10^{-7} m/s^2 or higher.

It should be pointed out that due to the shape of the satellite, the gravity gradient will have different effects on different parts of the satellite. This will in turn create an external gravity gradient torque. However, the external torque that is created is, usually, relatively small in comparison to other external torques and thus can be ignored [Mooij 1994; Wertz et al. 2011].

Third Bodies

As the Earth is not the only mass in the universe the object in orbit will experience the gravitational effect of other celestial bodies. As stated by King-Hele [1964] the two main effects are from the Sun and the Moon. Thus, it is important to take these two effects into account. The effect of another body on the object as described by Wakker [2015] is:

$$\ddot{\mathbf{r}}_{tb} = \sum_{i=1}^{n} \mu_i \left(\frac{\mathbf{s}_i - \mathbf{r}}{\|\mathbf{s}_i - \mathbf{r}\|^3} - \frac{\mathbf{s}_i}{\|\mathbf{s}_i\|^3} \right) \tag{4.19}$$

where n is the number of third bodies, i is the current third body being analysed, and $\mathbf{s}_i$ is the distance from the third body to the centre of the main body. The first term then represents the effect of the third body on the satellite, and the second term represents the effect of the third body on the main body. When doing it this way the resultant acceleration of the satellite due to the third body is with respect to the main body, thus no corrections to the reference frame are required.

For the project, the only two cases that need to be considered for the third body perturbations are the effect of the Sun and the Moon [King-Hele 1964]. The other planets in the solar system do not have an influence that needs to be taken into account. The values for other planets tend to be 4 orders of magnitude smaller than that of the Sun or the Moon. For instance, Venus has an effect of around 1×10^{-10}-1×10^{-11} m/s^2 [Noomen 2019].

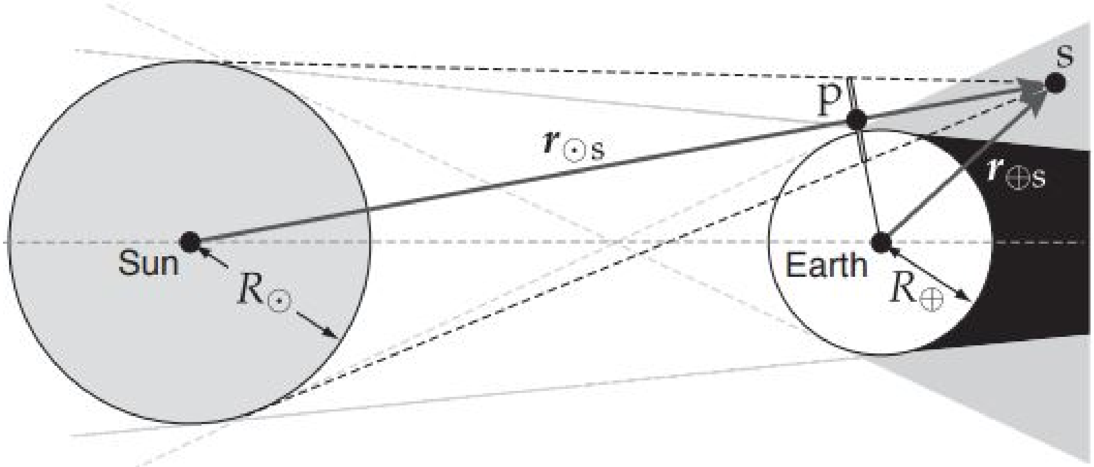

Figure 4.5: Penumbra and umbra of a satellite orbit [Doornbos 2011]

Solar Radiation

Solar radiation pressure occurs due to the transfer of momentum between the photons and the spacecraft. The effect of this phenomenon is modelled as per Wertz et al. [2011] by the following equation:

$$\ddot{\mathbf{r}}_{rad,B} = S_{sun} \frac{\mathbf{r}_{sun,sc}}{||\mathbf{r}_{sun,sc}||} \frac{A_{sun} C_{rad}}{m\ c} \tag{4.20}$$

where S_{sun} is the mean solar flux at a distance of 1 au, $\mathbf{r}_{sun,sc}$ is the position vector between the Sun and the satellite, A_{sun} is the area of the satellite facing the Sun, C_{rad} is the reflectivity coefficient of the satellite, c is the velocity of light and m is the mass of the satellite. It should be noted that the solar radiation acceleration is in the body frame. Thus, a change of coordinate system will have to be applied. Additionally, as the Earth is rotating around the Sun, the value of the mean solar flux will vary depending on the time of the year. This change is of less than 3% [Vielberg and Kusche 2020] and thus can be ignored and a constant value of S_{sun} is used.

Furthermore, it should be noted that for the solar radiation acceleration to have an effect the satellite must be in a direct line of sight of the Sun. This means that if the satellite is in the shadow of the Earth the value of $\ddot{\mathbf{r}}_{rad,B}$ will be zero. Figure 4.5 shows the penumbra and umbra of an object in orbit and describes the geometric relationships. It should be noted that the effect of the atmosphere on the refraction and absorption of light from the Sun will not be taken into account. For very precise orbit determination purposes this might play a role but for the current project, it can be ignored [Doornbos 2011].

Finally, the albedo and infrared radiation of the Earth could also be taken into account. However, as the solar radiation acceleration is already smaller than the other discussed perturbations here, and the albedo and infrared radiation are only a fraction of the solar radiation pressure they will be ignored [Wertz et al. 2011]. This is based on the fact that the albedo and infrared radiation of Earth can be modelled by two sources of 450 and 250 $\mathrm{W\,m^{-1}}$ at cloud altitude that decreases quadratically with altitude [Wakker 2015]. Assuming an altitude for clouds of around 12 km for an orbit at 120 km the total radiation would be 1/100 of the initial value. Thus, it was decided to ignore the radiation from Earth. In a future study of the sensitivity of the results of the project, this effect could be added for specific shapes of satellites but for now, it will be ignored.

Aerodynamic Perturbations

The perturbing acceleration due to the atmosphere of the Earth also needs to be taken into account. The acceleration due to aerodynamic perturbation is described as follows [Mooij 1994]:

$$\ddot{\mathbf{r}}_{aero,B} = \frac{1}{2} \frac{\rho V_A^2 S_{ref}}{m} \begin{pmatrix} C_X \\ C_Y \\ C_Z \end{pmatrix}_B \tag{4.21}$$

where ρ is the density of the atmosphere, V_A is the airspeed, S_{ref} is the aerodynamic reference area and the coefficients C_X, C_Y and C_Z are the force coefficients in the body frame of the satellite. Thus, once again, a change of coordinates will have to be performed when taking the aerodynamic perturbations into account. The values of the density will be found using the atmospheric model while the coefficients will be obtained from the SPARTA software, as will be explained in Chapter 6.

It is worth noting that the airspeed velocity is dependent on the velocity of the atmosphere. This means that the velocity of the satellite depends both on the angular velocity of Earth and on the airspeed at that point in time. As will be seen later on in Section 7.1 a thermospheric wind model will also be included. The HWM14 model provides the thermospheric winds in a horizontal plane defined by an ellipsoid. There are two components, one northwards and one eastwards. These two components can then be implemented into the velocity vector of the satellite to take into account the effect of the thermospheric winds.

Finally, the last effect that needs to be taken into account is the aerodynamic torque. This torque is created due to the offset between the centre of pressure and the centre of mass. It can thus be described as seen by Equation (4.22) where $\mathbf{r}_{cm}$ is the distance between a location at which the moments will be calculated and the point of action of $\ddot{\mathbf{r}}_{aero}m$. The magnitude of this torque is very dependent on the shape of the object. This means that larger objects usually tend to have larger aerodynamic torques.

$$\mathbf{T}_{aero,B} = \mathbf{r}_{cm} \times \ddot{\mathbf{r}}_{aero}m \tag{4.22}$$

The generation of the coefficients for the $\mathbf{T}_{aero,B}$ will be generated using SPARTA too. An analysis, similar to that performed for the aerodynamic force coefficients, will be performed for the torque coefficients in order to be able to use them in TUDAT. More information regarding the generation of the torque coefficients is given in Section 6.5.

5

Aerodynamic Modeling

One of the main goals of the project at hand is to propagate the orbit of the object that is being analysed. To do so accurately, the aerodynamics of the object must be understood. This is due to the fact that small changes in aerodynamics could result in a different force, or moment, experienced by the object. This would in turn affect the propagation of the orbit and if not modelled correctly it would give unrealistic results. Thus, special emphasis is placed on the different aspects of the aerodynamics of the object.

As will be seen in Chapter 6, all the aerodynamic coefficients will be generated using SPARTA. However, it is important to understand the mathematics behind the results in order to be able to fully comprehend the results and make sure they are correct. Thus, all of the analytical solutions shown in this chapter will be used for the verification and validation of the results, shown in Chapter 8. The chapter is divided into two sections. First of all, the different flow regimes which the object might experience and which methods for calculating the pressure and shear coefficients can be used are introduced and explained in Section 5.1. Finally, the transformation from the shear and pressure coefficients to aerodynamic coefficients is explained in Section 5.2.

5.1. Flow Regimes

Three flow regimes are present in the atmosphere. These are a continuum, transition and free-flow regime. Due to the atmosphere having a variable and decreasing density as the altitude increases, the aerodynamic analysis of the objects has to vary to take these changes into account. In the upper atmosphere, starting at around 100 km, the atmosphere starts to behave as a rarefied gas. This means that the effect of collisions between particles becomes less important and the flow cannot be considered a continuum any more.

As expected, each regime has specific characteristics and a different analysis needs to be performed for each one. A brief introduction of each regime and how their analysis is performed will be given in the subsections to follow. It should be pointed out that to define these different regimes, the Knudsen (Kn) number is used. The Knudsen number measures the ratio of the relaxation distance to the dimension of the flow field. It is described as follows [Regan 1993]:

$$\mathrm{Kn} = \frac{\lambda}{L} \tag{5.1}$$

$$\lambda = \frac{1}{N\sigma^2\sqrt{2\pi}} \tag{5.2}$$

where L is the characteristic length, λ is the mean free path of molecules, N is the number density of the gas and σ is the effective diameter of the gas particles.

5.1.1. Continuum Flow Regime

Continuum flow happens when the density is high enough that all the particles collide with each other at a high frequency. This means that Kn requires a rather small value, usually defined as Kn « 0.01 [Regan 1993]. During continuum flow, the gas dynamics are dominated by the inter-collision of particles within the gas. This means that the gas can be assumed to be ideal and the Navier-Stokes equations can be used to analyse the behaviour of the vehicle in the continuum regime.

However, the low Kn means that the continuum flow usually happens at the lower altitudes of the atmosphere, usually below the 100-120 km range, and thus not much analysis was performed on continuum flow during this project. Nonetheless, as it was previously mentioned, it is important to fully understand the physics behind the results from SPARTA. Thus, it is relevant to go over and be able to analyse the current flow regime.

During the continuum flow regime, the stresses and pressures experienced by the body highly depend on its velocity. There are five different subdivisions of the continuum flow which are defined by the Mach number. These categories are [Regan 1993]:

- Subsonic incompressible flow, when $M_\infty \leq 0.3$
- Subsonic compressible flow, when $0.3 < M_\infty < 1$
- Transonic flow, when $0.8 < M_\infty < 1.2$
- Supersonic flow, when $1 \leq M_\infty < 5$
- Hypersonic flow, when $M_\infty \geq 5$

For the current analysis, as the altitude for the continuum flow is relatively low, it is likely that the object only experiences hypersonic flow. This is due to the fact that the object will be travelling at velocities much larger than the local speed of sound. In order to analyse the continuum flow, it is possible to use SPARTA. However, as will be seen later on, the computational time required to run the simulations for the lower densities in SPARTA was rather high.

5.1.2. Free Molecular Flow Regime

Opposite to the continuum flow, in the free molecular flow regime, there are few collisions between particles. A very high Kn, defined as Kn»10 [Regan 1993], represents the free flow regime. Due to the small number of collisions between particles, the gas dynamics are dominated by surface-particle collisions. As expected, this flow regime will be common in the upper atmosphere, above 150 km, and most of the analysis of the project was to focus on this regime.

A number of factors need to be taken into account when modelling molecule-vehicle collisions. The main two factors are the following:

- Energy accommodation coefficient (α_E)
- Particle reflection model

To begin with, the energy accommodation coefficient has to be analysed. The energy accommodation coefficient is a measurement of the kinetic energy lost by molecules during the collision with surfaces. The equation to describe said coefficient is the following:

$$\alpha_E = \frac{E_i - E_r}{E_i - E_w} = \frac{T_i - T_r}{T_i - T_w} \tag{5.3}$$

where E_i is the energy transported to the unit area of the satellite surface by incident molecules, E_r is the energy carried away by the reflected molecules and E_w is the energy that would be carried away if the reflected molecule had adjusted to the surface temperature [Moe et al. 1998]. Equivalently, the temperatures of said molecules could also be used for the analysis.

As can be seen, the value of α_E depends on a number of factors, and the exact value for α_E is not known. Discussion and analysis of the actual value of α_E is going on right now. Based on analysis performed by Pilinski et al. [2010; 2016] the accommodation coefficient for satellites at altitudes of about 250 km is between 0.93 and 0.98. Additionally, studies by Doornbos [2011] show that at around 200 km the accommodation coefficient approaches a value of 1. However, in the analysis performed by March [2020] it is found that GOCE and CHAMP accommodation coefficients of around 0.85 to 0.80 fit the data significantly better. This is supported by March et al. [2021] where for the Swarm satellites it was found that an accommodation coefficient of 0.85 maximizes the consistency of the Swarm density observations. As previously stated, the altitudes of these three satellites are above 250 km. For simplicity, and some SPARTA limitations, the project uses an accommodation coefficient of 1. This matches previous studies and agrees with the evidence for the lower altitude regime, which is where the focus of the project was.

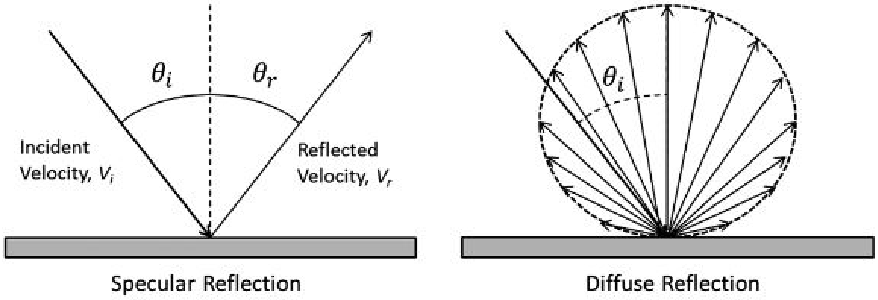

Figure 5.1: Different gas-surfaces interactions. Adapted from [Mehta et al. 2014]

The second aspect to be analysed is the reflection model of the particles with the surface of the satellite, or object. There are two main forms of reflection, specular and diffuse reflection, as seen in Figure 5.1. There is a third form of reflection, quasi-specular, which is a combination of the two previously mentioned reflection forms. In specular reflection, the particle transfers only momentum in the direction perpendicular to the surface while the parallel component stays the same. This results in a reflection that has a very similar angle to the incidence angle. In order to have specular reflection, it is suspected that the particle needs to hit a clean surface. If the surface is coated with atomic oxygen and other reaction products, which is the case at altitudes bellow 300 km, as observed by Moe et al. [1998], and Moe and Moe [2005], the reflection tends to be diffuse. This means that the reflected particle can assume any magnitude and direction of velocity given by a Maxwell-Boltzmann distribution. For the project at hand, it was decided to use the diffuse reflection as Saltsburg et al. [1966], and Moe and Moe [2005] found that at around 300 km and at lower altitudes, this interaction happens to be the most common one. Additionally, it was decided to use diffuse reflection because the analysis focuses on the end of life of the object. This means that the object has been in orbit for a large number of orbits which would result in increased coverage of the surface due to absorbed particles.

To be able to fully model the free molecular flow SPARTA will be used. Nonetheless, there is an analytical method that will be explored. The method, developed by Chambre and Schaaf [1961] and explained by Hart et al. [2014] could be considered the equivalent of the local inclination method for hypersonic continuum flow but for the free molecular flow. These are a set of equations to calculate the pressure and shear coefficient of a panel with a specific inclination to the free flow. These equations are the following:

$$\begin{aligned} C_{p,i} = \frac{1}{s^2}\Bigg[&\left(\frac{2-\sigma_N}{\sqrt{\pi}} s\sin\theta_i + \frac{\sigma_N}{2}\sqrt{\frac{T_w}{T_\infty}}\right) e^{-(s\sin\theta_i)^2} \\ &+ \left\{(2-\sigma_N)\left((s\sin\theta_i)^2 + \frac{1}{2}\right) + \frac{\sigma_N}{2}\sqrt{\frac{\pi T_w}{T_\infty}} s\sin\theta_i\right\}(1+\mathrm{erf}(s\sin\theta_i))\Bigg] \end{aligned} \tag{5.4}$$

$$C_{\tau,i} = -\frac{-\sigma_T\cos\theta_i}{s\sqrt{\pi}}\left[e^{-(s\sin\theta_i)^2} + \sqrt{\pi}s\sin\theta_i(1+\mathrm{erf}(s\sin\theta_i))\right] \tag{5.5}$$

where T_w is the wall temperature, T_∞ is the free stream temperature, erf() is the error function, defined as:

$$\mathrm{erf}(x) = \frac{2}{\sqrt{\pi}}\int_0^x \exp\left(-\chi^2\right) \mathrm{d}\chi \tag{5.6}$$

Finally, the last parameter of Equations 5.4 and 5.5 is s, the molecular speed ratio, given by:

$$s = \frac{V_\infty}{\sqrt{2RT_\infty}} = M_\infty\sqrt{\frac{\gamma}{2}} \tag{5.7}$$

It should be noted that the value of σ_N and σ_T is approximately one. This is due to the fact that these two parameters are the normal and tangential momentum accommodation coefficients, which will be 1 if the diffusion reflection is used.

One of the variables that have not been touched upon yet is the wall temperature T_w. The exact value of the wall temperature is not known. Thus, an approximation will have to be used. For this project, a value of 400 K will be used based on March et al. [2019]. It should be noted that since T_w « T_∞ the sensitivity in the free molecular flow regime to this parameter is expected to be low according to Doornbos [2011] and March [2020]. This is supported by a sensitivity analysis carried out by Toonen [2021] which showed a negligible change in the C_D of the satellite when the wall temperature was changed by 400 K.

It is also important not only to analyse the equations but also the accuracy of the method. As can be expected, the method will likely not be as consistent as the SPARTA simulations, as it is an analytical method for a numerical problem. Nonetheless, a number of studies have been performed on the accuracy of said method. Firstly, simple shapes such as a flat panel, a cube, a sphere and a cylinder have been tested not only by Hart et al. [2014] but also by a number of different studies such as Toonen [2021], Doornbos [2011], March [2020], Mehta et al. [2014] with very high success. The results of these shapes when compared to Monte Carlo methods, not only SPARTA but also the NASA-developed DSMC Analysis code (DAC), are in agreement with the aerodynamic coefficients.

For more complex shapes, less analysis is available. March [2020] performed an analysis on CHAMP, GRACE and GOCE. In said research, he calculated the different C_D and C_L of the satellites for different attitudes and speed ratios. The conclusion of the research was that the results were very dependent on the attitude and speed ratios. In some cases, the discrepancies between the analytical and the SPARTA simulations were around 2% or less, while in other cases there were discrepancies of up to 32%. However, as for the current project these equations were used only for the verification of the simulations of SPARTA these variations were not taken into account.

5.1.3. Transition Regime

The final flow regime that will be analysed is the transition regime. This regime is defined as 10^{-3} < Kn < 10 [Regan 1993], and is, out of all the regimes, the hardest one to analyse. The behaviour of the gas in this regime is not very well understood yet thus there are no theoretical equations that describe the behaviour in this regime. This means that a bridging function is usually used. The bridging function relates the coefficients on the continuum flow and the free flow regimes and creates a range of values to be used in the transition regime. Of course, this is not a very accurate description of the behaviour. Thus, for the current project, SPARTA was used once again.

The use of SPARTA for the transition regime is not new. It has been previously done by a number of researchers like Toonen [2021]. The main problem that arises when using SPARTA for the transition regime is the verification of the results. As there are no governing equations, it is difficult to find accurate data for the verification of the results. As will be seen in Chapter 8, verification of the results in the transition regime was performed against results from the literature.

Another factor that affects the analysis of the transition regime is that there is no fixed altitude for which the transition regime occurs. It highly depends on the object's characteristics and state, such as size and velocity, thus different objects enter the transition regime at different altitudes. As shown in Moe et al. [1998] the altitude range can be from about 130 km for smaller satellites to 165 km for larger vehicles, like the space shuttle. Fortunately, SPARTA only uses number density values as input, thus the behaviour of the transition regime should be properly modelled in the SPARTA simulation.

5.2. Aerodynamic Coefficients

The last aspect that needs to be covered is the generation of the aerodynamic coefficients. As previously mentioned, SPARTA will output pressure and shear coefficients, and so do the equations for the free-flow regime explained in this section. In order to calculate the aerodynamic coefficients, it is necessary to transform from one coefficient to the other. To do so all that is required is to integrate the pressure and shear coefficients over the surface of the body and in the case of the moment coefficients to multiply by the vector distance to a centre point. In order to do so, derived equations from [Hart et al. 2014] can be used to explain how it is performed. It is important to note that these equations are derived for the free-flow regime but should work for all regimes. The equations are the following:

$$d\mathbf{f} = (C_p\hat{\mathbf{n}} + C_\tau\hat{\mathbf{t}})dA \tag{5.8}$$

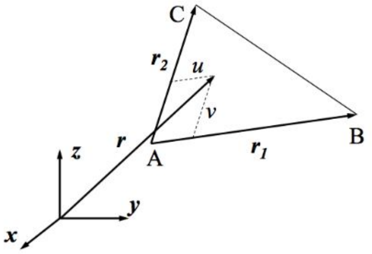

Figure 5.2: Surface parametrization of triangular panel [Hart et al. 2014]

$$\begin{pmatrix} C_X \\ C_Y \\ C_Z \end{pmatrix} = \frac{1}{A_{ref}} \int \int_S d\mathbf{f} \tag{5.9}$$

$$\begin{pmatrix} C_l \\ C_m \\ C_n \end{pmatrix} = \frac{1}{A_{ref} l_{ref}} \iint_S \boldsymbol{r} \times d\mathbf{f} \tag{5.10}$$

where dA is the differential area which is being analysed, $\hat{\mathbf{n}}$ and $\hat{\mathbf{t}}$ are the unit normal and unit tangential vector of the differential area being analysed, C_p and C_τ are the pressure and shear coefficients of the current area being analysed, A_{ref} is the total area of the object, l_{ref} is the total length of the object and **r** is the vector between the centre of the current area being analysed and the centre point for the calculation of the moment coefficients. As can be seen from the previous equations, the process is rather straightforward once the vectors are known. The equations to find the normal and tangential vectors are given by Hart et al. [2014]:

$$\hat{\mathbf{n}} = \frac{\mathbf{r}_u \times \mathbf{r}_v}{\|\mathbf{r}_u \times \mathbf{r}_v\|_2} \tag{5.11}$$

$$\hat{\mathbf{t}} = \frac{\hat{\mathbf{n}} \left(\hat{\mathbf{V}}_\infty \cdot \hat{\mathbf{n}}\right) - \hat{\mathbf{V}}_\infty}{\sqrt{1 - \left(\hat{\mathbf{V}}_\infty \cdot \hat{\mathbf{n}}\right)^2}} \tag{5.12}$$

$$\sin\theta = -\hat{\mathbf{V}}_\infty \cdot \hat{\mathbf{n}} \tag{5.13}$$

where $\mathbf{r}_u$ and $\mathbf{r}_v$ are the vectors defining the area being analysed, which for a triangular area are depicted in Figure 5.2, and $\hat{\mathbf{V}}_\infty$ is the normalised velocity vector defined as the following:

$$\hat{\mathbf{V}}_\infty = - \begin{bmatrix} \cos\alpha\cos\beta & \sin\beta & \sin\alpha\cos\beta \end{bmatrix}^T \tag{5.14}$$

As will be seen in Section 6.2, the Starlink satellite will be generated in a mesh that is composed of triangles, as it is the required input for SPARTA. Thus, for the verification of the free-flow regime, the equations explained in this chapter can be used with the same mesh. Additionally, the process of calculating the normal, tangential vector and then integrating the coefficients over the area must be performed for each of the triangles in the object mesh. Finally, for the process to find the coefficients using SPARTA a slightly different process is performed. This is due to the fact that SPARTA provides the pressure and shear vectors in the aerodynamic frame of SPARTA already. A more in-depth explanation for the generation of the coefficients from the SPARTA data will be given in Section 5.2.

Part II

Software Architecture

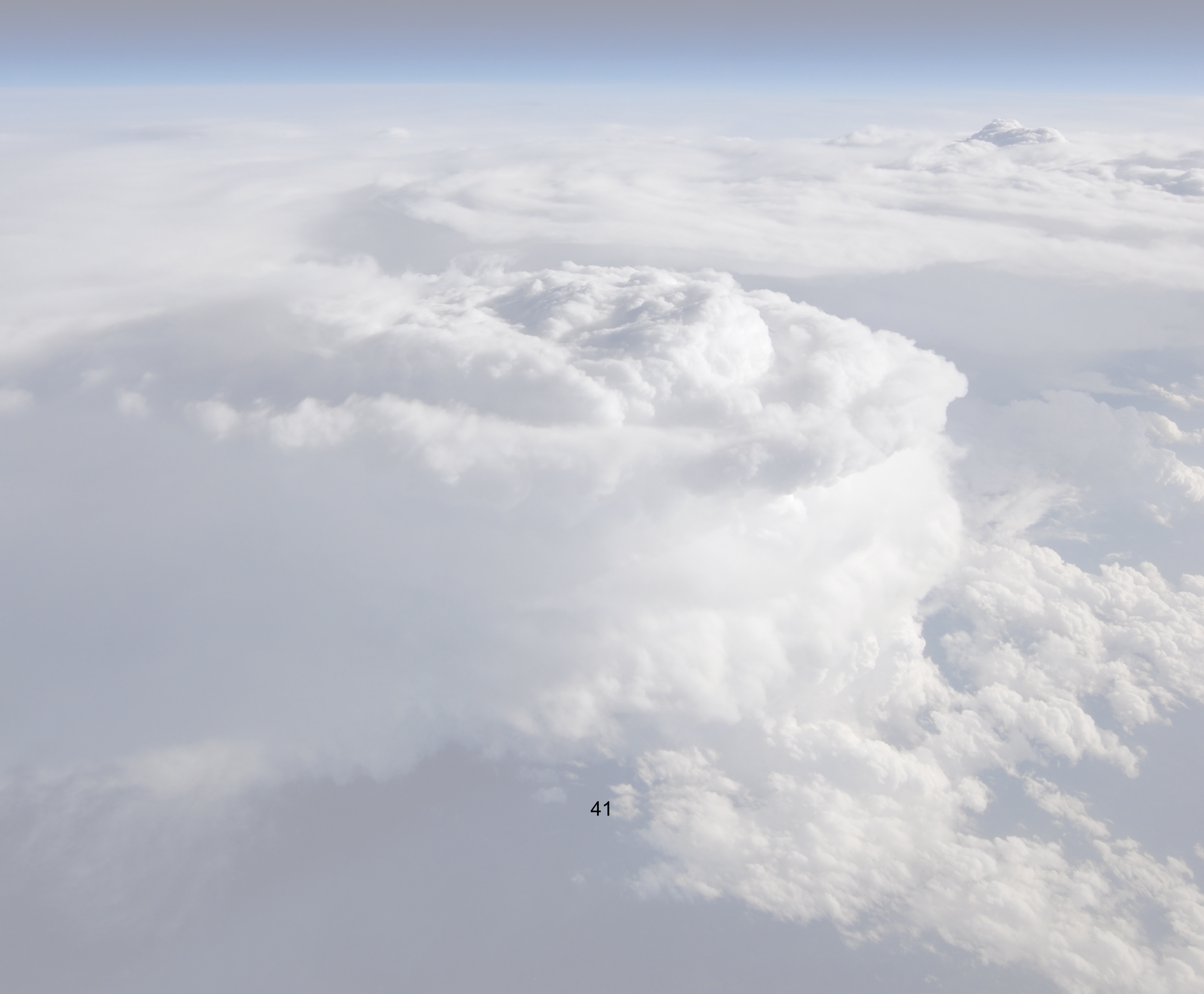

6

SPARTA Set-Up

As previously explained, the primary disturbance in the orbit that is being propagated is the aerodynamic one. The forces and moments experienced by the satellite, due to the aerodynamic perturbations, are higher than all the other perturbations. Thus, it is of key importance to be able to understand and properly model the aerodynamic properties of the object being analysed. This is due to the fact that small changes in aerodynamics could result in a completely different trajectory of the object. In order to perform this aerodynamic analysis, the SPARTA[1] software will be used.

However, before SPARTA can be introduced, it is important to understand the architecture of the complete software used for this thesis. Thus, in this chapter, an introduction to the software architecture will be first given in Section 6.1. Then, once all the architecture is clear, each section of this chapter will explain the components in the Aerodynamic Coefficient Database block of the software architecture, seen in Figure 6.1. Thus, firstly, an explanation of the satellite shape and the mesh that is used as input in SPARTA is given in Section 6.2. Following this, in Section 6.3, an explanation of how SPARTA works, the set-up, required inputs and outputs are given. Once the whole set-up is clear, there is a special focus on the link between SPARTA and TUDAT and how the different aerodynamic angles are defined. This is done in Section 6.4. Then, once the link between both pieces of software is clear, the post-processing of the SPARTA output is explained and performed in Section 6.5. The main focus of the section is on the transformation between shear and pressure coefficients to aerodynamic force and moment coefficients. Finally, in Section 6.6 an explanation of how the database with all the aerodynamic coefficients which will be used in TUDAT is generated is given. As will be explained in Section 6.1, the verification and validation of SPARTA is given in Chapter 8.

6.1. Software Architecture

As can be seen in Figure 6.1, there is a high number of interactions between the different aspects of the code. An introduction to the different areas of the code will now be given. A more in-depth explanation will be given in the following chapters. Firstly, the aerodynamic coefficient database block is present on the left side. As can be seen in the architecture figure, it is compromised of three components. The first component is about the SPARTA software, which will be explained in Section 6.3. Then, the other two components are, one for the post-processing of the SPARTA output and aerodynamic coefficient generation and one for the generation of the database of said coefficients. Each of these blocks is explained in Section 6.5 and Section 6.6 respectively. Additionally, the inputs for the aerodynamic coefficient database are also pointed out. It should be noted that the satellite mesh is only used once, in the SPARTA software block. Once the post-processing has been performed and the aerodynamic database generated, the satellite mesh is not used any more.

The second block to be covered is the Environment Set Up block. In said block, there are only two components, the thermospheric wind model, HWM14, and the atmospheric wind model, NRLMSISE-00. Each of these two aspects of the simulation environment is explained more in-depth in Section 7.1. Additionally, the inputs and outputs are once again clear. A number of location parameters, along with

---

[1] `https://sparta.github.io/`

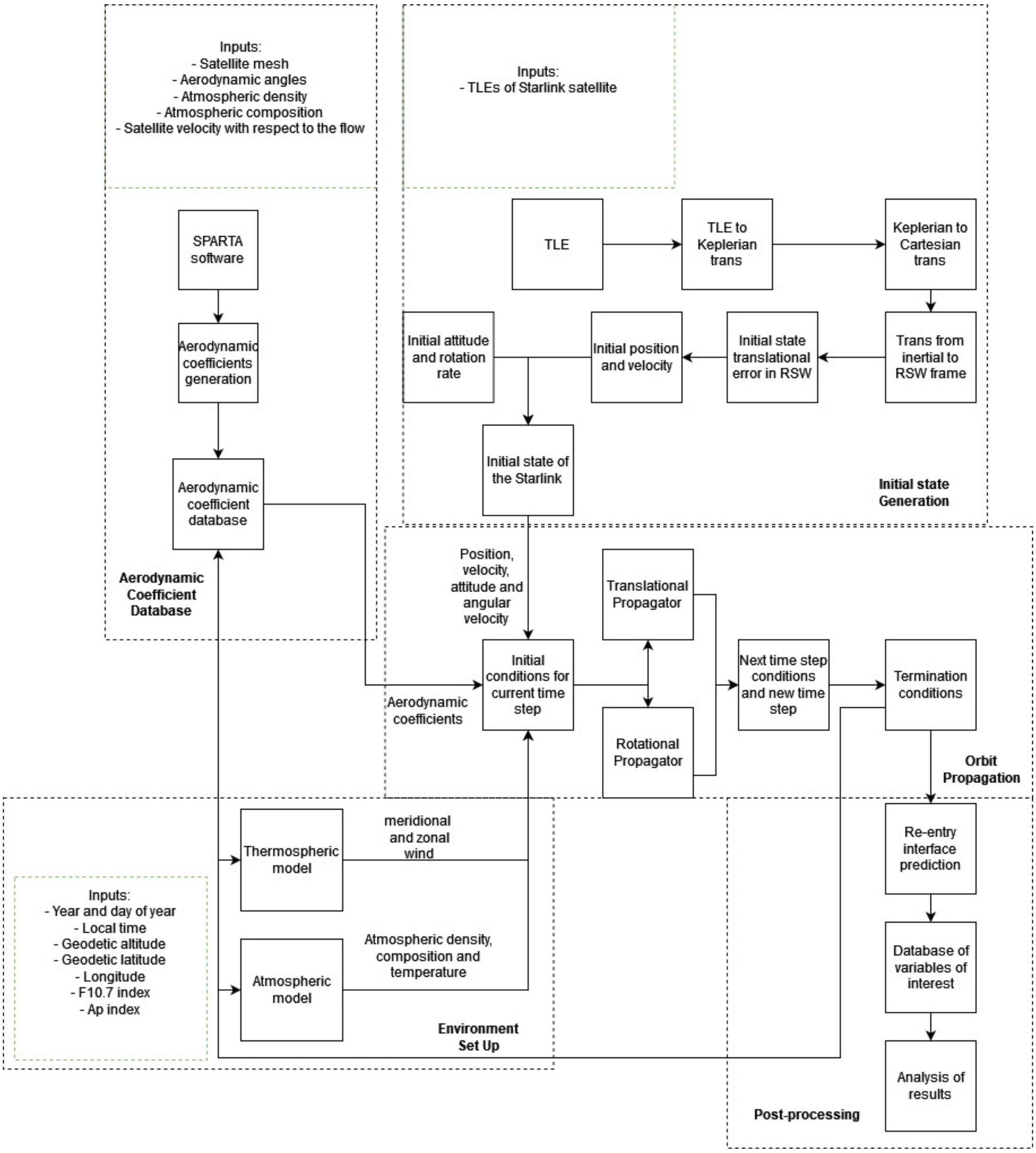
Inputs:
- Satellite mesh
- Aerodynamic angles
- Atmospheric density
- Atmospheric composition
- Satellite velocity with respect to the flow
Inputs:
- TLEs of Starlink satellite
SPARTA software
Aerodynamic coefficients generation
Aerodynamic coefficient database
Aerodynamic Coefficient Database
TLE
TLE to Keplerian trans
Keplerian to Cartesian trans
Trans from inertial to RSW frame
Initial state translational error in RSW
Initial position and velocity
Initial attitude and rotation rate
Initial state of the Starlink
Initial state Generation
Position, velocity, attitude and angular velocity
Aerodynamic coefficients
Initial conditions for current time step
Translational Propagator
Rotational Propagator
Next time step conditions and new time step
Termination conditions
Orbit Propagation
Inputs:
- Year and day of year
- Local time
- Geodetic altitude
- Geodetic latitude
- Longitude
- F10.7 index
- Ap index
Thermospheric model
meridional and zonal wind
Atmospheric model
Atmospheric density, composition and temperature
Environment Set Up
Re-entry interface prediction
Database of variables of interest
Analysis of results
Post-processing

Figure 6.1: Software architecture

geomagnetic and solar activity and dates, are required for both of the models to work as intended. If the inputs are delivered correctly, then the output of the HWM14 model is meridional and zonal winds while for the NRLMSISE-00 the atmospheric density, its composition and temperature are provided as output. The third block to be covered is the Initial State Generation. This block consists of a number of different components whose main aspect is to generate the initial position, velocity, attitude and angular velocity of the satellite. From the input, which is a TLE of the desired Starlink satellite, a number of processes provide an initial translational state which can also include an error term based on the TLE errors. This process is explained more in-depth in Section 7.5.

The fourth block to be covered, and one of the most extensive ones, is the Orbit Propagation. In this block, all previously mentioned blocks converge for the orbit propagation to take place. This block is the main block of the thesis and is explained very thoroughly in Chapter 7. In order for the software architecture to fit in this thesis, a number of processes that take place within this block have been removed from the image. The most important aspects have been kept to illustrate the process which takes place. Once the initial state is ready, the environment has been linked to the translational and rotational propagation and the aerodynamic coefficients of the satellite, along with other properties of the satellite, have been

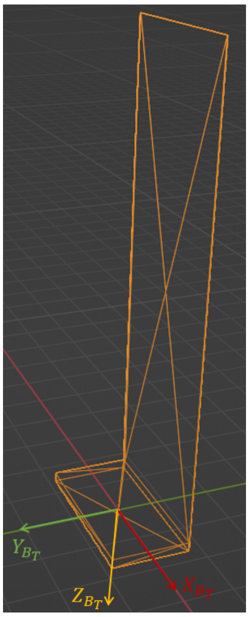

Figure 6.2: Starlink mesh

generated, the orbit propagation can take place. In order for this to happen, a propagator and integrator need to be selected. Said process is explained in Section 7.4. Once the orbit propagation is set up, different termination conditions can be set and the states of the satellite when these conditions are met are recorded and saved.

Finally, the post-processing of all the data is performed in order to see if the results answer the research question postulated at the beginning of this thesis. This post-processing takes place in the results chapter, Chapter 9. It should be noted that like any other project, a verification and validation for the whole software has been performed. The verification and validation process is placed in a separate chapter in order to keep all the acceptance tests, verification tests and validation tests together to make it easier to follow. Said verification and validation are performed in Chapter 8.

6.2. Mesh

Before any analysis is performed on the aerodynamics of an object, the shape of the object must be defined. As previously mentioned, the case study for the thesis is the Starlink satellite. Defining the shape of the satellite has been previously done in Chapter 3. Now it is important to translate the shape of the satellite into a useful model. In order to do so, a number of simplifications need to be performed such that a mesh can be generated.

A mesh is a collection of vertices, edges and faces that describe an object. Each face is then divided into subsections, called panels. For the aerodynamic analysis, this will be a key aspect. A mesh will be used to define the Starlink satellite in SPARTA such that the aerodynamic analysis can be performed. SPARTA requires an input mesh with specific characteristics for it to run properly. Thus, it is important that the mesh of the satellite is generated in such a way that it fits within SPARTA. In order to do so, there are two main parameters that need to be taken into account.

First, there is the shape of the mesh panels. There are multiple different ways to define a panel. The number of points and edges on each panel can vary, and different shapes can be used. However, for SPARTA, all panels need to be triangular. This means that each panel will have 3 points, and each point must connect to the other two points with 1 edge. The second aspect that needs to be taken into account is that the mesh needs to be ”watertight”. This means that all points need to be, at least, part of two faces. The method to check that this condition is complied with will be explained further down.

To generate the mesh, the program that will be used is Blender. Blender is an open source for 3D modelling. Due to Blender being one of the most popular tools for 3D modelling, there is a high number of sources for learning. This is one of the reasons that Blender was chosen. The second reason is the fact that it is possible to save the file as an STL file. This means that a mesh with triangular panels is created instantly for the surface of the object. This surface mesh can then be used for the aerodynamic analysis. This is a very helpful feature which reduces the time of generating the meshes by a significant amount. It should be noted that to run SPARTA, an extra step needs to be taken. As previously explained, in order for SPARTA to run, it is necessary to check that the mesh is watertight. In order to do so, an internal file provided in the SPARTA package is run. This file transforms the STL file into a SPARTA surface file and checks that the mesh is watertight and all panels are triangular.

Additionally, it is important to point out that the complexity of the shapes of the objects is limited. This is due to the fact that for very complex shapes, SPARTA will take longer to run and could also crash. This error and the steps to move around it are explained in more detail by Hładczuk [2022]. To prevent this error, and due to the fact that the exact geometry of the Starlink is not known with high accuracy, a simple mesh will be used for the Blender models. A simple mesh consists mostly of flat surfaces without sharp edges and convex or concave elements [Hładczuk 2022]. The number of triangular panels defining the mesh is not relevant to the definition of a simple mesh. In Figure 6.2 the mesh used for the Starlink can be seen. The body frame of Starlink is also defined in said image. This body frame is centred around the geometric centre of the main body of the satellite.

One further remark is to be made about Blender. It is also possible to add different material properties to the mesh. However, the effect of the materials on the aerodynamics of the object is out of the scope of the material. What will be done with the material properties function is to assign colours to the different parts of the object which might be of interest. For instance, for the shape used for the verification and validation of SPARTA, each side of the shape had a different colour such that it is easier to identify the rotation of the shape inside of SPARTA.

6.3. SPARTA

”SPARTA is a Direct Simulation Monte Carlo code that models rarefied gases using collision chemistry and boundary conditions models” [Plimpton and Gallis 2022]. This brief, but concise description of SPARTA gives the user a great explanation of what can be expected of the software. SPARTA can simulate and model the behaviour of millions of particles in a simulation. Said behaviour is based on the kinematic theory of gases. As can be expected, due to computational costs, the actual simulation uses a smaller number of particles in the simulation than in real life, based on an input ratio one provides. This means that the results of the simulation are an approximation, but the results closely agree with experimental results. This is the prime reason to use SPARTA, the outstanding behaviour when compared to experimental results. It is a great accomplishment given that the simulation of SPARTA has a number of constraints, such as the finite number of particles, the non-zero mesh sizes and the step sizes used in the analysis.

In order to fully explain how SPARTA will be implemented, a brief introduction to SPARTA will now be given. Firstly, the set-up conditions for the simulation, such as time step and box size, among others, that will be required to run SPARTA are given in Section 6.3.1. This will be followed by the simulation inputs, such as density and velocity, among others, required inputs are introduced and explained in Section 6.3.2. Once the inputs and simulation set-up is clear, a little trick on how the simulation is performed will be performed is explained in Section 6.3.3. The results and post-processing will be explained separately in Section 6.5 due to the complexity of the post-processing.

6.3.1. Set-up conditions

In order for the simulation to run properly and produce reliable output, a proper set-up needs to be performed. This subsection will cover how to generate the most important parameters for the simulation. We will begin with the number of particles used in a simulation, denoted f_{num}. This parameter is a ratio between the simulated particles to the real particles, and it is of key importance as too many particles will lead to excessive CPU time, while not having enough would lead to results that do not represent real-life situations. In order to calculate f_{num}, the following equation is used [Hładczuk 2022]:

$$f_{num} = \frac{nrho * box\_size}{part\_cell * cell\_num} \tag{6.1}$$

where $nrho$ is the number density in kg m^{-1}, box_size is the simulation domain, $cell\_num$ is the number of grid cells and $part\_cell$ is the number of simulated particles an individual cell contains. Studies showed that as long as the value of box_size is sufficiently large, for a given value of $nrho$ the values of box_size

and $cell\_num$ do not influence the convergence of the simulation. Additionally, it was also found that for $part\_cell$ the range of values between 1 and 15 provide the best results. For the current project, the following values will be used in agreement with Hładczuk [2022]:

- box_size = 12^3
- $cell\_num$ = 50^3
- $part\_cell$ = 8

These values were chosen for a number of reasons. Firstly, the box_size is constrained by the physical shape of the mesh. As previously explained, the solar array of Starlink has a length of 9.6 m, thus the box size must have, at least, those dimensions. It is possible to change the dimensions of the box as one only gets 9.6 m of length where the solar array is. However, for the simplicity of the input script, it was decided to keep the shape of the box constant. As for the other two values, they were chosen in order to reduce the CPU time of the simulation. Results for a $cell\_num$ = 50^3 and $cell\_num$ = 100^3 had consistent results, and the same goes for the different $part\_cell$.

The next important set-up parameter to take into account is the $timestep$. This value determines how often the results are saved. A large $timestep$ will provide correct results but at the cost of a very high CPU time while the opposite can be said for a short $timestep$. In order to find the optimum $timestep$ value the following equation is used:

$$timestep = \frac{box\_side}{V_{rel} * cell\_side * factor} \tag{6.2}$$

where V_{rel} is the relative velocity of the object being analysed and box_side is the length of a side of the simulation box. It is important to not confuse box_side with box_size as the former refers to the along-track dimension of the box. The same applies to $cell\_side$ and $cell\_num$ where the former is the number of cells in the along-track direction.

For the $timestep$ a $factor$ of 10 was chosen based on Hładczuk [2022]. Simulations with different steps were carried out and it was concluded that a value of $factor$ 10 would provide a fast enough simulation without sacrificing the reliability of the results. This means that for the different relative velocities which are used in the simulations, which will be explained in Section 6.3.3, the time steps will range between 4.71×10^{-5}-1.68×10^{-6}.

Finally, the last set-up parameter that should be mentioned is the selection of inter-molecular collision. In the free flow regime, there are no inter-molecular collisions, thus they can be turned off for these simulations in order to reduce the simulation time. However, for the transition regime and the continuum flow, these collisions must be taken into account. In order to take these collisions into account, SPARTA offers two possible models. These are the variable hard sphere (VHS) and the variable soft sphere (VSS) models. For this thesis, the VSS is used. The reason for such a decision is that the VSS takes into account the viscosity coefficients of the different air components [Koura and Matsumoto 1992] which has been proved to be the more realistic representation of the inter-molecular collision behaviour [Morokoff and Kersch 1998].

6.3.2. Simulation Inputs

Like for any software, in order to run SPARTA the appropriate inputs need to be used. The inputs that are required for SPARTA are the following:

- Geometry of object to be analysed
- Attitude of the object with respect to the free stream
- Number density
- Temperature of gas
- Wall temperature
- Accommodation coefficient
- Velocity of free stream
- Air composition

A brief explanation of what each input is will now be given. First of all, the Geometry of the object to be analysed needs to be generated. The process to generate said mesh has been previously explained in Section 6.2. Next, the attitude of the object with respect to the free stream needs to be defined. In this case, there are two main angles of interest, the angle of attack and the angle of sideslip. As will be explained in Section 6.4 there is a link between the angle of attack and the angle of sideslip between SPARTA and TUDAT that needs to be taken into account when defining the inputs. Following the attitude of the object, the number density which needs to be simulated is also required. As a number of altitudes will be simulated in order for the database to be generated, a changing density will be required. The boundaries set for the density analysis are 10^{16} to 10^{20} m^{-3}. As it will be seen later on in Figure 8.4, an analysis was performed on the behaviour of the aerodynamic coefficients with respect to changes in the number density. It can be seen that for number densities smaller than 10^{16} m^{-3} the coefficients are constant. Thus, for the propagation, if the number density is lower than 10^{16} m^{-3} the coefficients for the 10^{16} m^{-3} case are used. The higher bound of 10^{20} m^{-3} was taken as the number density at 100 km altitude on a high solar activity day. This way the density should never be any higher than 10^{20} m^{-3} at the altitude of 120 km which is when the re-entry phase has been decided to start.

Then, there is the temperature of the gas, wall temperature and accommodation coefficient. For the current project, both temperatures are kept constant at 1000 K and 400 K, respectively, while the accommodation coefficient has been set to one. This is done in order to keep the accommodation coefficient constant. SPARTA has a limitation in that one can only input a 1 or 0 for the accommodation coefficient and the solution to changing the accommodation coefficient is changing the wall temperature. However, because for this thesis the accommodation coefficient is 1 there is no need to change the values of the temperature.

Finally, there is the free stream velocity and the air composition. In order to fully simulate the behaviour of the object in the atmosphere an air composition needs to be given. However, as will be explained in the next subsection, it is not as simple as defining an input file with a given percentage of each molecule that is in the air. This method could be done but then for each different number density, a different percentage would have to be used. Instead, what will be done is define the air composition as full oxygen and change the stream velocity to simulate different particle behaviour. This little trick is performed in order to reduce the simulation time.

6.3.3. Speed Ratio Simulation Trick

As previously mentioned, a small trick will be performed with the simulations in SPARTA. To reduce the simulation time the air composition is set to be 100 % atomic oxygen and the velocity of the free stream is changed. In order to be able to fully proceed with this technique, the speed ratio, as defined in Equation (5.7), will be used. For the current project, a speed ratio range of 1 to 14 will be applied. This is due to the fact that speed ratios above 14 are very unlikely to occur, particles need to be very light, and speed ratios below 1 require a correction factor [Hładczuk 2022]. Using this technique, the database that will be generated will now have one more variable, the speed ratio of the simulation. How the aerodynamic coefficients are generated from this data will be further explained in Section 6.5.

The main concern that comes from using this technique is the accuracy of the results. In her thesis, Toonen [2021] found that the errors from using a constant atomic oxygen air composition in relation to a complete description of the composition are less than 1 % for the C_D in the free molecular flow regime. In the case of the transition regime, the errors in the C_D go up to 2.8 %. Additionally, the results from Toonen are supported by those from Mehta et al. [2014]. Thus, for this project, the technique of the speed ratio will be used.

6.3.4. Input Files for SPARTA

Now that the set-up is properly introduced, let us take a look at what an input file would look like. An example of the input file can be seen in Figure 6.3. In this screenshot, only the beginning of the file is present, where the variables are defined. These variables are then used as per Hładczuk [2022]. In said file, firstly the grid size is generated. This grid size is constant for all the simulations. Then, the number density value is varied to get the whole range of values required for the thesis. Additionally, as previously explained in this section, the values for f_{num} are also varied to fit with the corresponding number densities. Once those parameters are defined, the speed ratios and the corresponding velocities are also added to the input file. Once again, the speed ratios are selected from 0.5 to 14 in order to be able to model all possible particle speeds. It should be noted that the $timestep$ values are also modified

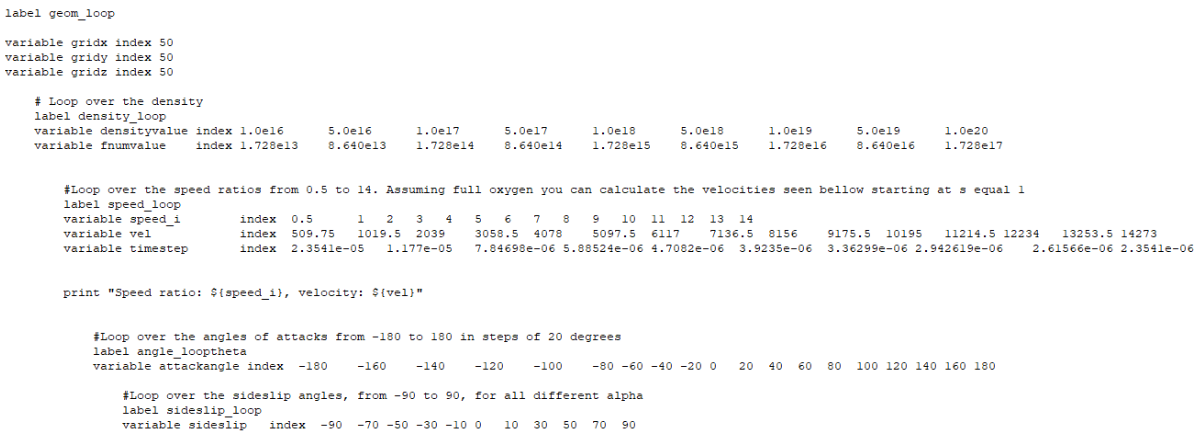

```
label geom_loop

variable gridx index 50
variable gridy index 50
variable gridz index 50

    # Loop over the density
    label density_loop
    variable densityvalue index 1.0e16      5.0e16      1.0e17      5.0e17      1.0e18      5.0e18      1.0e19      5.0e19      1.0e20
    variable fnumvalue    index 1.728e13    8.640e13    1.728e14    8.640e14    1.728e15    8.640e15    1.728e16    8.640e16    1.728e17

        #Loop over the speed ratios from 0.5 to 14. Assuming full oxygen you can calculate the velocities seen bellow starting at s equal 1
        label speed_loop
        variable speed_i        index  0.5      1   2   3   4   5   6   7   8   9   10  11  12  13  14
        variable vel            index  509.75   1019.5  2039    3058.5  4078    5097.5  6117    7136.5  8156    9175.5  10195   11214.5 12234   13253.5 14273
        variable timestep       index  2.3541e-05   1.177e-05   7.84698e-06 5.88524e-06 4.7082e-06  3.9235e-06  3.36299e-06 2.942619e-06    2.61566e-06 2.3541e-06


        print "Speed ratio: ${speed_i}, velocity: ${vel}"


            #Loop over the angles of attacks from -180 to 180 in steps of 20 degrees
            label angle_looptheta
            variable attackangle index  -180    -160    -140    -120    -100    -80 -60 -40 -20 0   20  40  60  80  100 120 140 160 180

                #Loop over the sideslip angles, from -90 to 90, for all different alpha
                label sideslip_loop
                variable sideslip   index  -90  -70 -50 -30 -10 0   10  30  50  70  90
```

Figure 6.3: Example of an input file in SPARTA

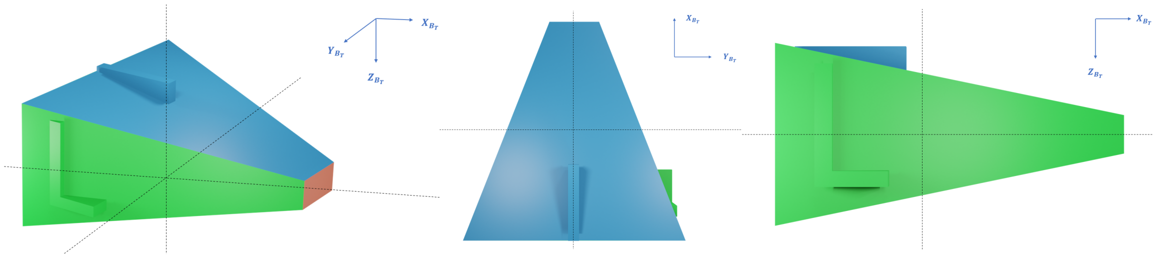

(a) 3D view **(b)** XY plane **(c)** XZ plane

Figure 6.4: Shape used for verification at different views

to the corresponding relative velocity as per Equation (6.2). Finally, the aerodynamic angles are also defined.

6.4. SPARTA and TUDAT rotation angles

SPARTA and TUDAT use different reference frames and different angle transformations. Thus, a given angle of attack in TUDAT does not necessarily represent the same rotation around the y-axis in SPARTA. It is of key importance to find the relationship between the pair of angles. In order to do so, the following process was performed. First, the object being analysed was defined in TUDAT reference frames. This is done in order to be able to set up the initial reference frame and angle definitions. Then, the object was input into SPARTA and a rotation inside of SPARTA was performed. Finally, the rotation in SPARTA was linked to a rotation in TUDAT following the expected force definition. More in-depth detail of the process will now be given. It is important to note that the method described here was applied to verify SPARTA. Thus, a different shape is used rather than the actual satellite. However, the method applies to all objects as long as the definitions used by TUDAT are consistent, and the shape is imported into SPARTA in the same way as described in this section.

6.4.1. Set up of object in TUDAT

Firstly, it is of key importance to understand how TUDAT defined the aerodynamic angles and frames. In TUDAT, the body frame is defined as seen in Figure 6.4. Additionally, the aerodynamic angles α_T and β_T are defined such that a positive angle results in a force in the negative axis. For instance, a positive rotation around the Y$_{A_T}$ axis would result in a ”pitch up” movement, which creates a force in the negative Z$_{B_T}$ axis and a force in the negative X$_{B_T}$. Thus, a positive α_T is defined as a positive rotation around the Y$_{A_T}$ axis. The same logic applies to the definition of β_T. A positive rotation around the negative Z$_{A_T}$ axis would result in a force in the negative X$_{B_T}$ and in the negative Y$_{B_T}$. Thus, a positive β_T is defined as a positive rotation around the negative Z$_{A_T}$ axis. The angle definitions can be seen in Figure 6.5.

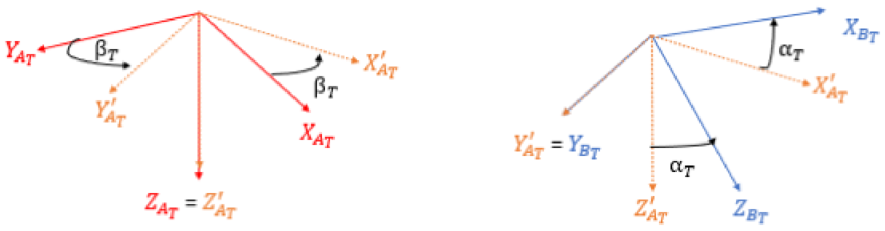

Figure 6.5: Definition of aerodynamic angles in TUDAT

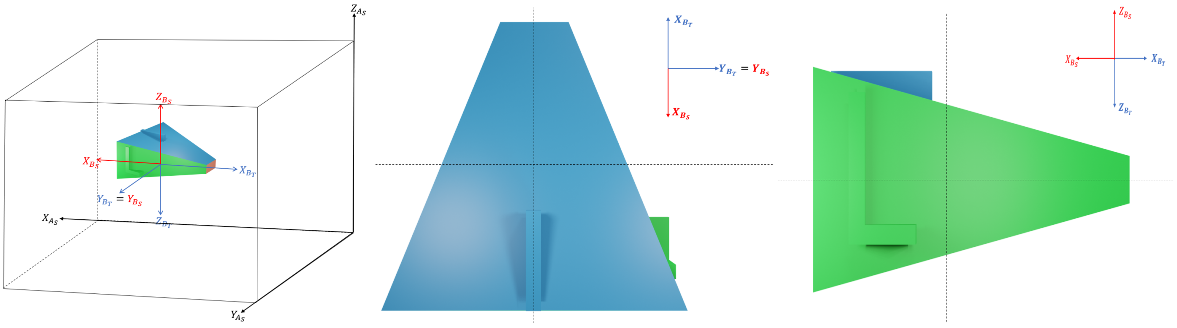

(a) 3D **(b)** XY plane **(c)** Shape used for verification in the XZ plane

Figure 6.6: Shape used for verification with SPARTA and TUDAT body frames

6.4.2. Set up of object in SPARTA

Now that the object definition in TUDAT is clear, it is important to describe how it is imported into the SPARTA simulation. The object is imported into SPARTA using an STL file. It is of high importance to set up the object in the correct axes position before importing it into SPARTA. Otherwise, the process described here will not apply. For this project, the object is imported as seen in Figure 6.6. In the images, there are 3 reference frames present. The first one, with subscript B_T, refers to the body frame of TUDAT. The second one, denoted by B_S, refers to the body frame of SPARTA. Finally, the third one, denoted by A_S, refers to the aerodynamic frame of SPARTA. As it can be seen, the B_T frame and the B_S frame have an offset of 180 degrees around the Y axis. Additionally, if there are no rotations in SPARTA, the B_S and the A_S are the same frames. All these axes will be of key importance when describing the transformations and axes' relations.

6.4.3. SPARTA rotations

Before getting into the relationship between angles, let us first explain how rotations in SPARTA work. When you rotate a body in SPARTA, you perform a body rotation. This means that if you perform more than one rotation, the following rotations will be performed on the original axis of SPARTA. This is different from TUDAT which uses reference frame rotations, as explained in Section 4.3. In order to analyse the rotations of SPARTA, it is first required to be able to describe them. A body rotation is expressed by Equation (6.3).

$$\mathbf{R}_{A_S(rot),A_S} = \mathbf{R}_z(\beta_s)\mathbf{R}_y(\alpha_s) \tag{6.3}$$

$$\mathbf{R}_y(\theta) = \begin{bmatrix} \cos\theta & 0 & \sin\theta \\ 0 & 1 & 0 \\ -\sin\theta & 0 & \cos\theta \end{bmatrix} \tag{6.4}$$

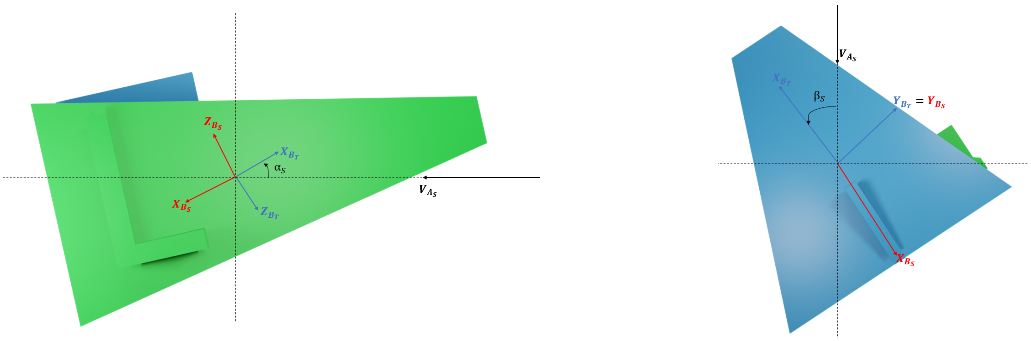

(a) Angle α_s around Y$_{A_S}$

(b) Angle β_s around Z$_{A_S}$

Figure 6.7: Rotations of verification shape

$$\mathbf{R}_z(\theta) = \begin{bmatrix} \cos\theta & -\sin\theta & 0 \\ \sin\theta & \cos\theta & 0 \\ 0 & 0 & 1 \end{bmatrix} \tag{6.5}$$

where $\mathbf{R}_z$ corresponds to a rotation around the Z$_{A_S}$ axis and $\mathbf{R}_y$ to a rotation around the Y$_{A_S}$ axis, see Equation (6.5) and Equation (6.4). The values of β_S and α_S are the rotation angles around the corresponding axis, which are used in SPARTA. It should be noted that the rotation is denoted by **R** instead of **C** as the latter represents a reference frame rotation while rotation in SPARTA is from the original axis. Additionally, the subscript $A_S(rot), A_S$ means the rotated points by the body transformation are still expressed in the SPARTA aerodynamic frame. Finally, it is important to point out that the rotations around an axis in SPARTA are positive in the counterclockwise direction.

6.4.4. SPARTA and TUDAT link

Once the shape and rotation are defined in SPARTA, all that is left is to look at the relationship between the angles in TUDAT and SPARTA. To do so, we will first analyse a rotation around the Y$_{A_S}$ only and then a rotation around Z$_{A_S}$. Based on TUDAT angles and the rotations in SPARTA, it is expected that a positive rotation around Y$_{A_S}$ will result in a positive force in the X$_{B_S}$ and Z$_{B_S}$ axis. However, as previously explained, these two axes have an offset of 180 degrees with respect to the TUDAT axes. This behaviour can be seen in Figure 6.7a. Thus, in the B_T frame, this is a negative force. Which, as previously explained, is a positive α_T. Thus, we know for now that for a positive, α_S we can expect a positive α_T of the same magnitude.

The same analysis can be performed for a rotation around the Z$_{A_S}$ axis. A positive rotation around Z$_{A_S}$ axis results in a positive force along X$_{B_S}$ and a negative force in the Y$_{B_S}$ axis. Once again, looking at the B_T frame, this corresponds to a negative force on both X$_{B_T}$ and Y$_{B_T}$ axis. This behaviour can be seen in Figure 6.7b. Thus, we know that for a positive β_S we can expect a positive β_T of the same magnitude. With this, it is now known that the same angles apply to both SPARTA and TUDAT. With this clear, it is then possible to define the rotation between the TUDAT body frame and the SPARTA aerodynamic frame. This rotation is the following:

$$\mathbf{C}_{B_T,A_S} = \begin{bmatrix} -1 & 0 & 0 \\ 0 & 1 & 0 \\ 0 & 0 & -1 \end{bmatrix} \mathbf{C}_2(\alpha)\mathbf{C}_3(\beta) \tag{6.6}$$

where the unit matrix with inputs 1,1 and 3,3 are negative to account for the opposite direction of the axis and the matrices $\mathbf{C}_2$ and $\mathbf{C}_3$ are the standard matrices described in Section 4.3. The last two matrices correspond to the inverse of $\mathbf{R}_{A_S(rot),A_S}$.

6.5. SPARTA Output Post-Processing

Now that the inputs of SPARTA have been explained, and the link between the TUDAT and SPARTA angles is clear, it is time to talk about the outputs. As previously mentioned, the input for TUDAT is a look-up table from which the aerodynamic coefficients are taken from. However, the output from SPARTA is the pressure and shear vectors for each of the triangles in the mesh. Thus, there are a number of steps that need to be taken in order to reach the final aerodynamic coefficients. The steps will be similar to those described for the analytical expression in Section 5.2 . The first step is to transform the pressure and shear vectors into a force vector. In order to do so, the following equation is used:

$$d\mathbf{f} = \frac{1}{q_\infty}(\mathbf{p} + \boldsymbol{\tau})dA \tag{6.7}$$

$$\begin{pmatrix} C_X \\ C_Y \\ C_Z \end{pmatrix}_{A_S} = \sum_{n=1}^{s} d\mathbf{f} \tag{6.8}$$

where $d\mathbf{f}$ is the force coefficient per triangle in the mesh,q_∞ is the dynamic pressure, $\mathbf{p}$ and $\boldsymbol{\tau}$ are the pressure and shear vector values for each triangle in the mesh and dA is the area of each triangle in the mesh. Once all the forces are added together, for s triangles in the mesh, the aerodynamic force coefficients in the aerodynamic frame of SPARTA are found.

Once the force coefficients are found in the aerodynamic reference frame of SPARTA, all that is left is to transform the force coefficients into the aerodynamic frame of TUDAT. The same process as per the explanation given in the previous section will be performed. In order to do the transformations, Equation (6.6) is used. Now that the force coefficients have been explained, it is time to talk about the moment coefficients. These coefficients will be generated using a similar process as that used for the force coefficients. The only difference is that the moment coefficients will have an extra step in which the output from force coefficients is multiplied by the vector distance between the centre of the current triangle and the point of interest, which as previously mentioned is the origin of the body frame of both SPARTA and TUDAT. In order to calculate the moment coefficients, the following equation is used:

$$\begin{pmatrix} C_l \\ C_m \\ C_n \end{pmatrix}_{B_T} = \sum_{n=1}^{s} \mathbf{r}_{B_T} \times \mathbf{C}_{B_T,A_S} \cdot d\mathbf{f} \tag{6.9}$$

where $\mathbf{r}_{B_T}$ is the distance vector between the centre point of the triangle and the origin of the body frame, C_{B_T,A_S} is the transformation matrix between the SPARTA aerodynamic frame and the TUDAT body frame, as described by Equation (6.6), and $d\mathbf{f}$ is the force coefficient per triangle in the mesh. It should be noted that a small trick was used for calculating $\mathbf{r}_{B_T}$. As all the triangle positions in the body reference frame are the same, the distance vector can be calculated only once for the satellite mesh and used for all the different results. Additionally, it is important to note that consistency in the reference frames used is of key importance. The wrong reference frames will lead to results that do not correspond to the actual values.

One last important detail needs to be pointed out. In both, Equation (6.8) and Equation (6.9), the coefficients that come have a unit in them. This is due to the fact that the force coefficients are not normalised with respect to the area and the moment coefficients are not normalised with respect to the area and moment arm. This is due to the fact that in TUDAT a single reference area and length has to be used. This means that if the coefficients are normalised, it would not be possible to add them into TUDAT properly. Additionally, by having the area and moment arm added into the coefficients, the problem of having to recalculate all the drag, lift and side areas for the different aerodynamic angles is evaded. Thus, it was decided to maintain the post-processing such that the body force coefficients have units of m^2 and the body moment coefficients have units of m^3. For the verification and validation, in some cases the coefficients will be normalised in order to be able to compare them to other values. If this is the case, it will be clearly stated.

6.6. SPARTA Database

Now that the reference frames, the conversion between them and the post-processing of the results from SPARTA are clear, it is time to look into the database generation. Once the input files are generated, and the different SPARTA outputs are processed, it is necessary to somehow mix all these different aerodynamic coefficients into a database. To do so, a number of steps need to be taken.

Firstly, it is important to note that once all the output files have been read and post-processed, there is already a database. However, this database is rather scarce. This is due to the fact that the input files

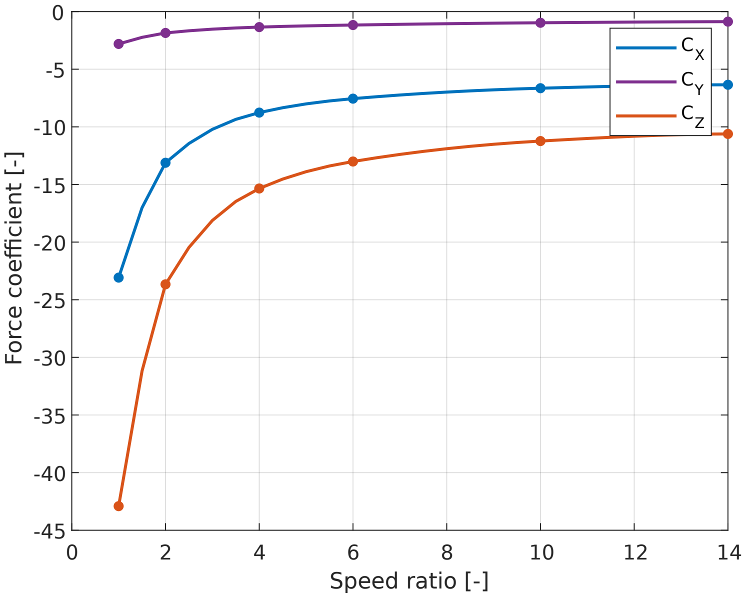

Figure 6.8: Force coefficient behaviour for different speed ratios

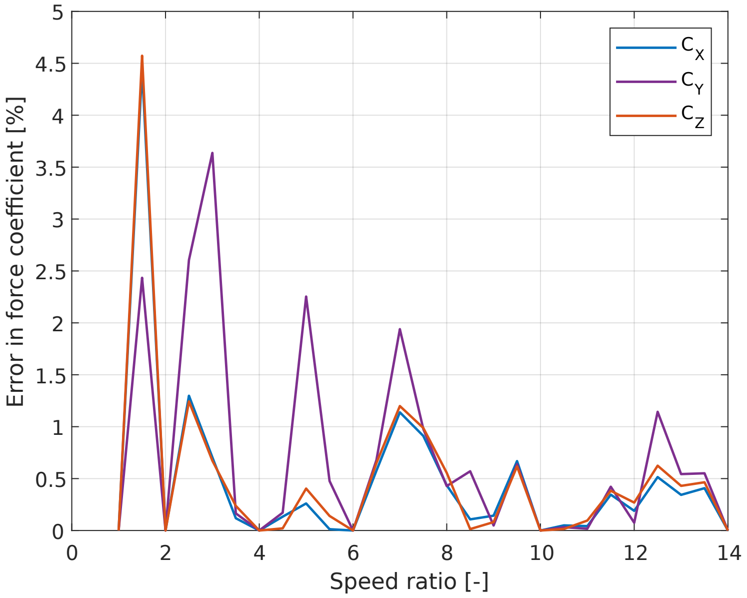

Figure 6.9: Error force coefficient behaviour for different speed ratios

for SPARTA have the aerodynamic angles in steps of 20° and the speed ratios used for the simulation were 1,2,4,6,10 and 14. Thus, the aerodynamic coefficients are only available for a specific number of parameters. In order to solve this problem, a spline interpolation was used. To be more precise, a Piecewise Cubic Hermite Interpolating Polynomial (PCHIP) method was used. The details of how PCHIP works will not be explained in detail in this thesis. What is important to note is that PCHIP uses cubic polynomial splines in order to be able to generate the missing data points. This means that there is an inherent error in the interpolated data. Thus, the more the number of points in the database, the smaller the error from the interpolation, but the longer the simulation time in SPARTA. This meant a trade-off had to be performed on the step size used for the aerodynamic angles and the speed ratios in the input files of SPARTA.

Two aspects should be pointed out. Firstly, it should be noted that the process explained in the next subsections is shown for the force coefficients only. This was due to the fact that the moment coefficients will have similar behaviour to the force coefficients, only with different magnitudes due to the cross product with the distance vector. Thus, the same analysis is valid for both sets of coefficients. Additionally, as will be seen inSection 8.2, the coefficient behaviour for the different densities is either constant during the free flow regime, or linear during the different aspects of the transition regime. Thus, for the initial files the densities were sampled at steps of factor 10 between 10^{16} m^{-3} and 10^{20} m^{-3}.

6.6.1. Speed Ratio Selection

Let us begin with the speed ratios. Instead of simulating 28 speed ratios, from 1 to 14 in steps of 0.5, it would be nice to reduce the number of simulations. To do so, an analysis of the aerodynamic coefficient's behaviour for different speed ratios was performed. As can be seen in Figure 6.8, the force coefficients have a logarithmic behaviour with an increasing speed ratio. This means that it should be possible to reduce the number of speed ratio points in the simulation. In order to check how many points can be used, a benchmark simulation of the force coefficients was generated using speed ratios with a step size of 0.5. Then, the number of speed ratios was reduced.

Finally, it was decided to use the 1,2,4,6,10 and 14 speed ratios. The error behaviour for this set can be seen in Figure 6.9. It can be seen that the error spikes in between the values used, as expected from the PCHIP method. However, the maximum spikes are less than 4.5 % which is a very reasonable value for the maximum error taking into account that the number of simulations has been decreased from 28 to 6.

It should be noted that for this simulation, the other parameters, in this case, the angle of attack, the sideslip angle and the number density, were chosen at random. The simulation for the different speed ratios was run a total of three times for different random values of the previously mentioned parameters. This was done in order to ensure that the results being shown here were not only for a specific case but for the general project. The same applied to the aerodynamic angle selection.

6.6.2. Aerodynamic Angles Selection

The next trade-off that had to be performed was on the steps of the aerodynamic angles. Similar to the process performed for the speed ratios, the first step was to look at the behaviour of the force coefficients versus the aerodynamic angles. The behaviour of the coefficients with respect to the angle of attack can be seen in Figure 6.10a, which was used as a benchmark. As can be seen, each force coefficient has a different behaviour. For this plot, a step of 5° was used. Once again, different steps were tested, and it was concluded that the best step to be used was of 20°. The results from said time step can be seen in Figure 6.10b and Figure 6.11. As it can be seen in Figure 6.10b, the curves fit the benchmark cases in a very concise manner. Additionally, as it can be seen in the error behaviour, the majority of the errors stay below 6 %. There are some peaks for the C_X and C_Z coefficients. However, this is due to the fact that at these locations, at around −90° and 90° for the C_X, and at around 4° and 177° for C_Z, these coefficients approach a value of 0. Thus, when normalizing the error with respect to the original coefficient value, it shoots up due to the small denominator.

Finally, it is important to look at the behaviour of the force coefficients with respect to the sideslip angle. Once again, the benchmark, with steps of 5° for the sideslip angle, can be seen in Figure 6.12a. Following the previous logic, different time steps were looked into and the results from the 20° were the best. The error behaviour and interpolation results can be seen in Figure 6.13 and Figure 6.12b respectively. For the case of the sideslip, the errors are a bit larger than for the angle of attack and speed ratios, with almost up to 8.5 %. Additionally, there are two spikes. Similar to the previous behaviour, these spikes occur when the coefficient goes towards zero, thus the normalisation of the error increases due to the low denominator. It should be noted that for the sideslip, it was decided to take into account the 0° situation. This was due to the fact that the 0° sideslip is considered a nominal condition, thus it is important to have an exact value for those nominal cases.

Now that the analysis of PCHIP has been completed, it is possible to define the inputs for the simulation in SPARTA. The speed ratio will consist of six speed ratios, 1,2,4,6,10 and 14, while both angle of attack and sideslip angle will have step sizes of 20°, with the sideslip also having a data point at 0°. Now that this is clear, it is possible to move into how the final database is generated.

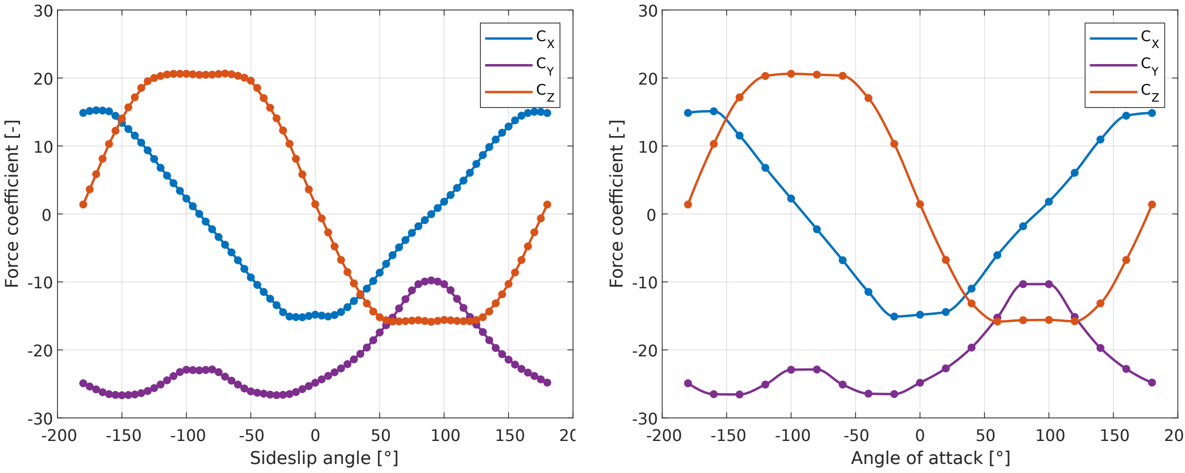

(a) Steps of α = 5°

(b) Steps of α = 20°

Figure 6.10: Force coefficient behaviour for the complete range of α with different α step sizes and interpolated using PCHIP

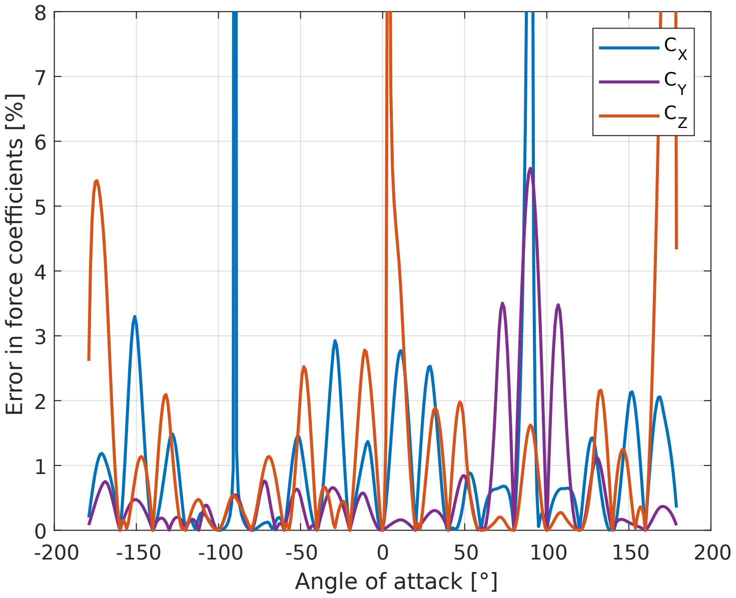

Figure 6.11: Force coefficient error behaviour for different angles of attack

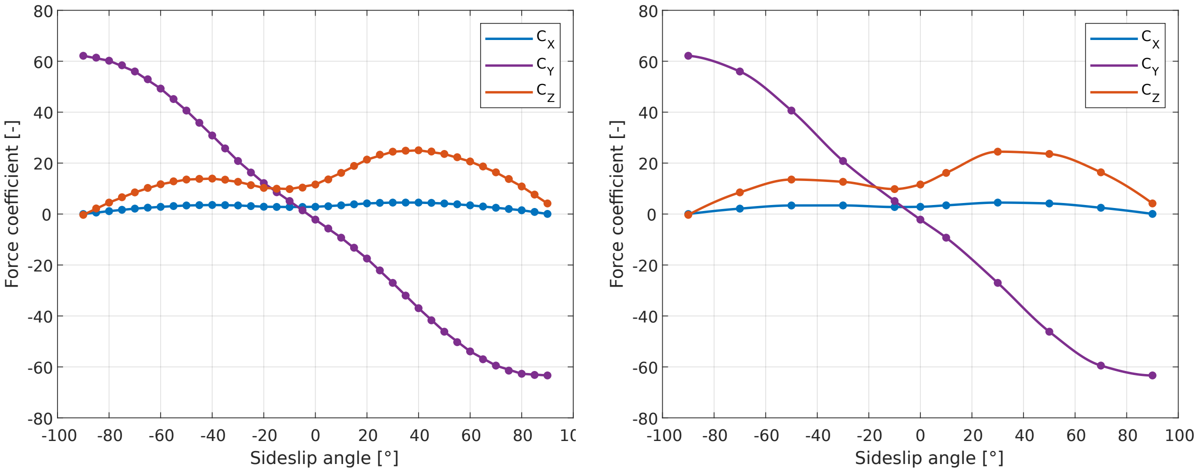

(a) Steps of β = 5°

(b) Steps of β = 20°

Figure 6.12: Force coefficient behaviour for the complete range of β with different β step sizes and interpolated using PCHIP

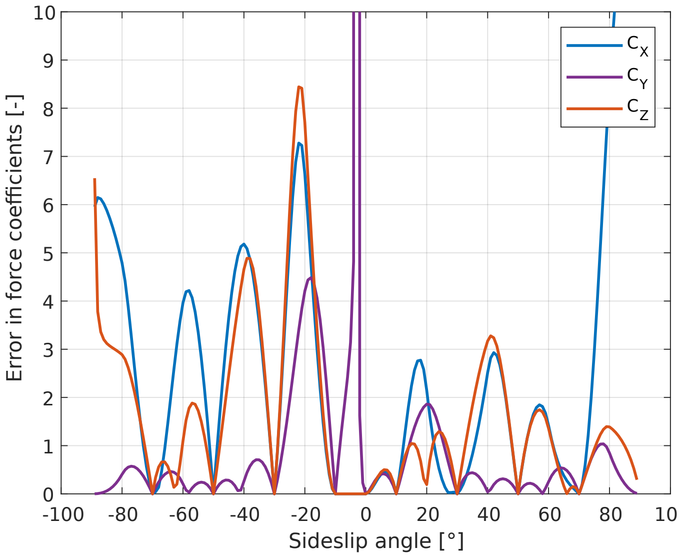

Figure 6.13: Force coefficient error behaviour for different angles of sideslip

Table 6.1: Example of part of the database for aerodynamic moment coefficients

nrho	s	α	β	C_l	C_m	C_n
1e+16	1	-180	-90	-568.966376057741	-0.871839801859918	-0.259630489805085
1e+16	1	-180	-88	-567.906143410428	10.5082863618185	1.77164914950241
1e+16	1	-180	-86	-565.835350504573	21.5850555290544	3.74839729614389
1e+16	1	-180	-84	-562.860880082562	32.333766986224	5.66609813556865
1e+16	1	-180	-82	-559.089614886783	42.7297200197034	7.52023585322596
1e+16	1	-180	-80	-554.628437659624	52.7482139158686	9.30629463456513
1e+16	1	-180	-78	-549.584231143472	62.3645479610957	11.0197586650354
1e+16	1	-180	-76	-544.063878080715	71.5540214417608	12.6561121300862
1e+16	1	-180	-74	-538.17426121374	80.29193364424	14.2108392151666
1e+16	1	-180	-72	-532.022263284934	88.5535838549094	15.679424105726
1e+16	1	-180	-70	-525.714767036685	96.3142713601451	17.0573509872138

6.6.3. Database Generation

The final step in database generation is to generate the database. In order to do so, the output files from SPARTA are post-processed and, as previously mentioned, a scarce database is created. Then, using PCHIP again, the database was interpolated from the broader steps to smaller steps. For the current project, the final steps were the following. For the speed ratios, the grid spacing was 0.5, and for the aerodynamic angles, angle of attack and sideslip angle, the grid spacing was of 2°. The decision to choose these values was based on two aspects. Firstly, the behaviour of the coefficients. As previously explained, in TUDAT interpolation is done during each 20 time step in order to find the aerodynamic coefficients for a given set of conditions. This interpolation done in TUDAT is a linear interpolation in order to reduce computational time. Thus, the grid size must allow for the linear behaviour of the aerodynamic coefficients to be shown. This is why the grid spacing of 0.5 for the speed ratio and 2° for the aerodynamic coefficients was chosen. Different grid spacings were tested and the results from TUDAT were compared, and it was decided to stick to the previously mentioned grid.

Secondly, it is also important to take into the computational time. The larger the database, the longer it takes to load and look up the values for the TUDAT interpolation. As was seen during the testing of the software, the slowest part of the software was due to the interpolation of the aerodynamic coefficients. Thus, it was of high priority to reduce this computational time. In order to do so, different grid sizing was tested. The results showed that the computational time different between the 5°, 2° and 1° grid size was minimal. Thus, it was concluded that the determining factor was linear behaviour and the 2° grid sizing was chosen. However, it was found that splitting the databases into two, one for force coefficients and one for moment coefficients, did result in a reduction in computational time. Thus, two databases were generated.

It should be noted that for the densities, no interpolation was done for generating the database. This was due to the fact that the coefficients that were generated using the initial steps proved to be well within their linear regime. Thus, there was no need to increase the size of the database. An example of part of the database for the force coefficients can be seen in Table 6.1.

7

TUDAT Set-Up

As the main object of the project at hand is to analyse the orbit decay, it is of crucial importance to have an orbit propagator. There are multiple orbit propagators available. However, it was decided to use the TU Delft Astrodynamics Toolbox (TUDAT)[1] [Kumar et al. 2012]. The main reasons for choosing this propagator were, firstly, the fact that it has been used before for similar projects such as Torrente [2021], Moreno Gonzalez [2020] and Lith [2020] among others. This also means that TUDAT has been verified and validated, only acceptance tests would have to be run to make sure proper implementation of the functions. Additionally, the author of this project has previously used this toolbox already, which will reduce the required time to set it up and have the propagation running. Furthermore, as it has been used before, it is known that the toolbox is able to model all the required perturbations and dynamics for the current project at hand. Finally, as DUT develops TUDAT it is possible to ask for assistance in case there is a problem that the author cannot solve.

The chapter will be structured following the boxes in the flow diagram. Firstly, the set-up of the environment, which consists of the modelling of the Earth, the wind model and the atmospheric model, is explained in Section 7.1. Then, once the environment is set up, the perturbing forces and moments acting on the satellite are explained in detail in Section 7.2. Next, the properties of the Starlink that are required for the propagation, such as the mass and the inertial tensor, are calculated inSection 7.3. After all the set-up is ready, the propagator and model state which is propagated, along with the integrator trade-off and selection are given in Section 7.4. Finally, the generation of the initial state based on TLE data is explained in Section 7.5.

7.1. Environment Set-Up

In order for the propagation to be as similar to the real world as possible, it is of key importance to be able to model the environment in which the satellite will be as accurate as possible. To do so, a number of different aspects need to be covered. In this section, the initial decisions made based on the requirements that will be used in this project are presented. Each subsection is based on a different aspect of the modelling.

7.1.1. Earth Modelling

For the current project, the modelling of the Earth was based on the following criteria:

- **AS-EARTH-01**: The Earth is an oblate spheroid that is defined by the equatorial, with value of 6 378 137 m, and flattening of 1/298.257223563 [Defense Mapping Agency 1987].
- **AS-EARTH-02**: The polar axis is the axis of symmetry of the oblate spheroid and also the axis of rotation.
- **AS-EARTH-03**: The rotation of Earth is assumed to be constant, with an angular velocity of $72.921\,15\times10^{-6}$ rad/s [Defense Mapping Agency 1987].

---

[1] `https://github.com/Tudat` (Last accessed: 11 April 2023)

- **AS-EARTH-04**: The centre of mass of the Earth and the origin of the Planetocentric Reference Frame are assumed to be in the centre of the spheroid.

First, it was necessary to decide how to model the geometrical aspect of Earth. For this, the previously mentioned assumptions are made. Of course, there is a reasoning behind these decisions. First of all, it was decided to model the Earth as an oblate spheroid rather than a sphere, as the atmospheric models usually require an ellipsoidal altitude. If you were to plug in a spherical altitude, the error could be up to 21 km for polar orbits [Archinal et al. 2011]. If it is possible to reduce such an error by a simple change in the shape of the Earth, it should be performed. Furthermore, it was decided to assume that the rotation axis of Earth is the same as the polar axis. In reality, the rotation axis is off by about 0.2°. However, when looking at the effect of the offset on the position on Earth, it is negligible. Secondly, the rate of change of the rotation axis is about 500 milliarcseconds, or about $1{\times}10^{-4}$°, in about 10 years [Archinal et al. 2011]. As the simulation time will not spawn centuries, the change in the rotation axis is negligible too. Additionally, the rotation of the Earth is assumed to be constant. Of course, this is not the case. However, once again, in a period of 10 years the change in the rotation causes a delay of about 5 ms. This will have a negligible effect on the simulations. Finally, it is assumed that the centre of mass of the Earth and the origin of the reference frames are the same. This is a simplification such that the calculations of the gravitational acceleration are simplified. In order to be able to perform these calculations an Earth Centre, Earth Fixed (ECEF) reference frame can be used.

7.1.2. Thermospheric Winds Model: HWM14

As the thermospheric winds are not the main focus of the project, their effect and modelling is not fully investigated, but instead the information is taken from previous studies. The main takeaways from these studies led to the following assumptions:

- **AS-TW-1**: The vertical thermospheric wind is assumed to be zero.
- **AS-TW-2**: The horizontal thermospheric wind is divisible into two components, along-track and cross-track.
- **AS-TW-3**: Thermospheric winds will be modelled using the HWM14 model.

Firstly, it can be assumed that the vertical thermospheric wind is zero. This is due to the fact that the magnitudes of vertical winds are significantly smaller than those of horizontal winds, and the effect on the satellite dynamics are much smaller. For reference, Visser et al. [2019] found that the vertical winds usually have an order of magnitude of 50 m s^{-1}. Assuming an orbital velocity of 7.5 km s^{-1}, this would induce an angle of attack of 0.4°. This is a negligible value. Thus, the vertical winds can be ignored and not applied to the project.

The second observation that is made is that the horizontal wind can be split into two components, cross-track and along-track. This is done in order to be able to quantify their effect individually. As found by Toonen [2021], the cross-track wind effect on the drag experienced by the satellite depends on the surface area of the facing the flow. In her analysis, it was shown that in a worst case scenario, the cross-track wind meant an increase in the C$_D$*A$_{ref}$ of up to 15% from the nominal value. This was due to the change of the direction of the object with respect to the atmosphere. This means that for objects that have a wide variety of possible projected areas, such as the Starlink satellite that has a solar panel significantly larger than the body, the thermospheric winds can greatly influence the experienced drag. Thus, cross-track winds should be taken into account. The second component, the along-track wind, has a much smaller effect on C$_D$*A$_{ref}$ but it has a similar effect on the overall drag experienced by the satellite. This is due to the fact that in the drag equation, the velocity of the satellite relative to the ambient air needs to be taken into account. Thus, along-track winds will also be needed to be taken into account.

Finally, it was decided to use the HWM14 model instead of other models or in-situ measurements in order to comply with the requirements previously mentioned. The in-situ measurements do not cover the whole Earth and do not reach altitudes of 300 km. This means that they cannot be used. Additionally, as explained by Toonen [2021] in her thesis, the HWM14 model is used instead of other models, such as the TIE-GCM, due to the fact that it is less computationally expensive. One reason for this can be attributed to the fact that the TIE-GCM model calculated a number of extra parameters, such as the variability of plasma density, which are not relevant for this study[2]. Furthermore, the HWM14 mode has been proved to be in good agreement of thermospheric wind values for GOCE and CHAMP [March 2020]. It should be noted that the HWM14 model underestimates the values of the thermospheric wind when compared to in-situ measurements from Earth, especially at high altitudes. However, for the 75 % percentile, both the HWM14 model and in-situ data have very similar values. Additionally, the HMW14 model does not take into account the solar activity influence. From research, it is still not clear, but it is believed that solar activity have an effect on the thermospheric winds. Nonetheless, during the duration of the project, the HWM14 was the best model that was available and thus was used. A brief introduction to the inputs and outputs of the HWM14 model will now be given.

---

[2] `https://kauai.ccmc.gsfc.nasa.gov/CMR/view/model/SimulationModel?resourceID=spase://CCMC/SimulationModel/TIE-GCM/2.5` (Last access: 17 April 2023)

The inputs for the HWM14 model are the following:

- Year and day
- Time of day
- Geodetic altitude
- Geodetic latitude
- Longitude
- Daily magnetic index

While the outputs are the following:

- Zonal and meridional wind velocity

As will be seen later on, the inputs for the HWM14 model are very similar to those of the NRLMSISE-00. Thus, the same input file will be used, the one provided by CelesTrack[3]. As the HWM14 model is implemented in Fortran, a wrap needs to be used. Fortunately, a wrap to Python was found[4] thus there was no to do it for the project. The HWM14 model was then implemented in TUDAT using the personalised thermospheric wind function provided by TUDAT. As will be seen later on, the HWM14 output was verified against results from online sources and that the transformation between the vertical frame of the output and the inertial frame was correct in TUDAT.

7.1.3. Atmospheric Model: NRLMSISE-00

In this subsection, an introduction to how to the set-up of the NRLMSISE-00 model, along with required inputs, expected outputs and data for verification is given. First of all, the NRLMSISE-00 model has been implemented in TUDAT. This means that the software is ready to be used. As the NRLMSISE-00 model works like a function, a set of inputs are required in order to get an output. The inputs required by the model are the following:

- Year and day
- Time of day
- Geodetic altitude
- Geodetic latitude
- Longitude
- Local apparent solar time
- 81-day average of $F_{10.7}$ solar flux
- Daily $F_{10.7}$ solar flux for previous day
- Daily magnetic index

To be able to use the model, a number of steps need to be taken. First, as the state propagation is performed on Cartesian elements, as will be later seen, a change from the inertial coordinates to Earth-fixed coordinates, from which the geodetic latitude, altitude and longitude can be obtained is required. Furthermore, a data file with the $F_{10.7}$ values will be required. TUDAT has implemented a data file from CelesTrack which contains observed values from 1957 until the current day. Additionally, complete predictions for one month since the current day are also implemented. After one month, the predictions do not include a 3-hour a_p index, instead, they use a monthly predicted a_p value as the daily value. This means that it is possible to propagate the orbit until 2 years into the future. However, for a more accurate propagation, it is recommended to propagate only until the 3-hour a$_p$ values are generated, so one month into the future.

---

[3] `https://celestrak.com/SpaceData/sw19571001.txt` (Last access: 15 April 2023)

[4] `https://github.com/rilma/pyHWM14` (Last access: 15 April 2023)

Now that the inputs have been introduced, the outputs will be explored. The outputs of the NRLMSISE-00 model are the following:

- Helium (He) number density
- Oxygen (O) number density
- Oxygen (O2) number density
- Nitrogen (N) number density
- Nitrogen (N2) number density
- Argon (Ar) number density
- Hydrogen (H) number density
- Total mass density
- Anomalous oxygen number density
- Exospheric temperature
- Temperature at altitude

These outputs will be required for a number of processes in the software. Firstly, the total mass density is required for the propagation of the orbit, as it directly affects the aerodynamic forces. Additionally, the density compositions and temperature will be key for the calculation of the aerodynamic coefficients. This will be explained in further detail in Chapter 6. These outputs will be key to correctly modelling the aerodynamic coefficients and forces and their effect on the propagation of the orbit.

7.2. Orbital Perturbations

Once the environment has been generated, it is important to define the forces and moments that will act on the satellite. As was seen in Section 4.5, a number of perturbations were introduced. In this section, these perturbations have been added to the propagation in TUDAT and an explanation on how is provided.

7.2.1. Gravitational Field of Earth

The model of the gravity field of Earth will be modelled using the following degree and order:

- **AS-GRAV-1**: The gravity field of the Earth is defined using spherical harmonics of degree and order 24.

For the gravitational field of Earth, it was decided to use a spherical harmonic model of degree and order 24. This decision is done in order to be able to meet the minimum required accuracy of the perturbing accelerations described by **REQ-GRAV-03**. When choosing a 24x24 model, one makes sure the single coefficient effect on gravity have an effect of 2×10^{-7} m/s^2 or higher. Additionally, if it was desired to increase the accuracy of the model, say using degree and order 70, the increase in accuracy would be less than 7 % [Vallado 2013]. The increase in computational time would not outweigh the small increase in accuracy. The specific mathematical equations describing the model are present in Section 4.5.

7.2.2. Third Body Perturbations

As it is known, the Earth is not the only body in the Solar System. Thus, similar to Earth, other bodies also have a gravitational acceleration that can affect the satellite. Fortunately for us, all other planets are too far away and are too small to have a significant effect. However, the Sun and the Moon do play an important role. In TUDAT it is possible to add third body perturbations to the satellite in the propagation. For the current project, the Sun and the Moon were added to the perturbations. The mathematical process TUDAT implements to model these forces is explained in Section 4.5. As will be seen in Chapter 8, acceptance tests were carried out to make sure the application in TUDAT was done correctly. It should be noted that for these third body perturbations, the gravity field of both the Sun and the Moon are set to be point masses. The difference between a point mass and a spherical harmonics plays a very small role for the third body perturbations. Thus, for a reduced complexity and computational time, the point mass gravity will be used to model those two gravity fields.

7.2.3. Solar Radiation Pressure

The other perturbation that is due to the Sun, is the solar radiation pressure. As previously explained, this perturbation is due to the transfer of momentum between the photons and the spacecraft. In the case of TUDAT, the acceleration due to the solar radiation pressure is modelled as a cannonball. This means the effective acceleration is co-linear with the vector connecting the source of radiation and the target. This model is not perfect, as it does not take into account the shape of the object. However, for the lower altitudes, this model has proven to be a very good approximation to real life. In order to fully define the solar radiation pressure, three parameters from the satellite properties are required. These are, the mass, the reference area facing the sun and the radiation pressure coefficient of the satellite, as seen in Equation (4.20). In order to define these parameters, a number of assumptions were made.

First, for the mass, it was assumed to be 260 kg. This value is taken from public sources of Starlink. The solar radiation pressure coefficient was assumed to be 1.0. This is based on the results for the Copernicus satellite, which has a similar shape to the Starlink [Peter et al. 2020]. Finally, the reference area of the Starlink was taken to be 20.6 m. To get this value, the area of the solar array of the Starlink was averaged over a sinusoidal wave. As the satellite is in free rotation, it is expected that during an orbit it will encounter different attitudes, and thus different reference areas facing the Sun. It was decided that an average of the possible orientations would be a good initial estimate.

It should be noted that in TUDAT it is possible to set an occulting body to the solar radiation pressure settings. What this means is that when the satellite is not in direct view of the Sun, the solar radiation pressure is set to zero. This option was also set on in the TUDAT settings, with the Earth as the occulting body.

7.2.4. Aerodynamic Perturbations

The last of the perturbations to be modelled in TUDAT is the aerodynamic ones. The explanation on how the generation of the database of the force and moment coefficients is generated is given in Section 6.6. For the TUDAT set-up, what is required to know is how the database of the coefficients is analysed such that the correct coefficients are selected. For now, it is important to know that the database which is used as input in SPARTA is made up of a number density column, a speed ratio column, an angle of attack column, a sideslip angle column and three columns which correspond to the force, or moment coefficients, for the previously mentioned parameters. An example of a section of the database can be seen in Table 6.1. The explanation on how the reading and interpolation of the database was done will be performed for the force coefficients, but the moment coefficients follow the same logic. The only difference is which coefficients are selected for the interpolation.

The first step is then to load the database. Once this is done, an interpolator had to be generated. This is due to the fact that the mesh which the database uses is rather sparse. For instance, the angle of attack has steps of 5°. In order to interpolate the values for the current values required for the given time step, a number of inputs are required. These inputs are the current number density of the simulation, the specific composition of the density, the molar mass of the components of the density and the angle of attack and sideslip angle. The first two components are taken from the NRLMSISE-00 atmospheric model output, the molar mass list of the densities is loaded once at the beginning of the simulation and the current angle of attack and sideslip angle are taken from TUDAT. Once all the values are known, for each of the inputs a lower and upper bound is found. Then, a linear interpolation between these values takes place. A visual representation of the selection of coefficients for the interpolator can be seen in Figure 7.1. These coefficients are then interpolated to the current value of each of the corresponding variables. For instance, Coefficients_U_U_U_U and Coefficients_U_U_U_L are interpolated to the current angle of attack. The same is done for Coefficients_U_U_L_U and Coefficients_U_U_L_L. Then, the output from these two interpolations is interpolated for the current value of the sideslip angle. This process is repeated until all the coefficients are interpolated for all the current variable values. These steps are repeated for the lower density value too, although not shown in the figure. The interpolation is repeated every 20 time steps during the orbit propagation. Meaning that the aerodynamic coefficients stay constant for 20 time steps.

As can be expected, there are boundary constraints that need to be set up. Firstly, the aerodynamic coefficients are constant when the number density is smaller than 10^{16} m^{-3}. As will be later explained, at higher altitudes, when the density is so small, the aerodynamic coefficient values are constant. Thus, if at any point in the simulation, a number density smaller than 10^{16} m^{-3} is found, the coefficients are not interpolated for the density. The same applies to the highest number density of 10^{20} m^{-3}. This density

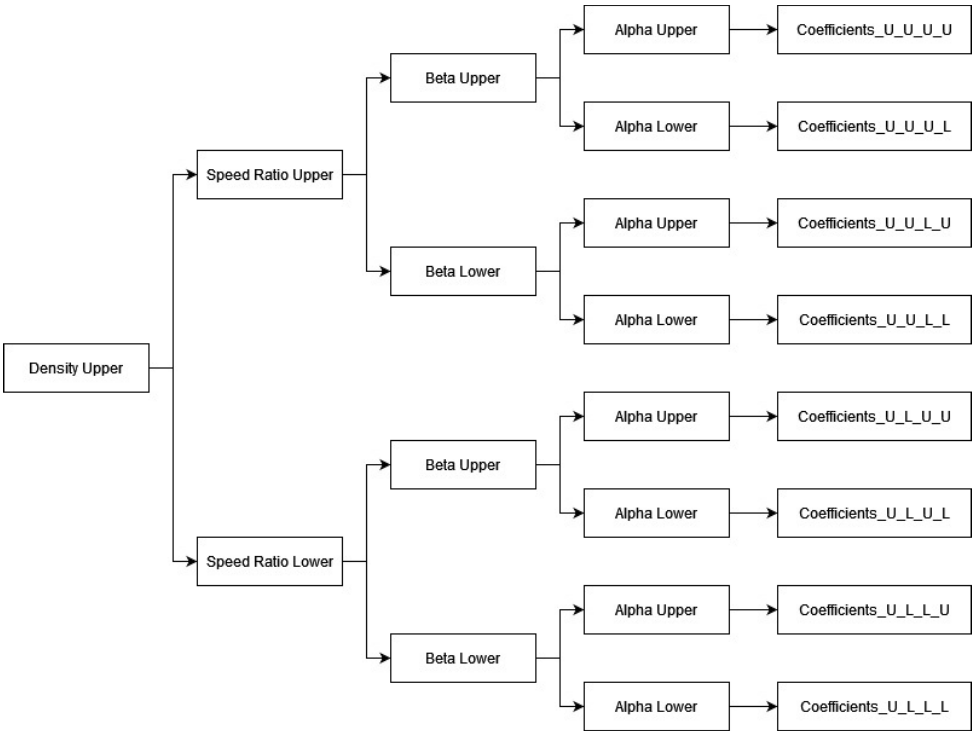

Figure 7.1: Example of aerodynamic coefficient selection for interpolation

corresponds to an altitude of around, 100 km which should never happen. In case it does due to some specific atmospheric conditions, it is also set as a boundary constraint. A similar case is done for the speed ratios. A lower bound of 1 and a higher bound of 14 have been set. In case these values are breached, the interpolator simply takes 1, or 14, as the boundary conditions for the interpolation. The upper bound of 14 should not be a problem unless the simulation goes into very low altitudes, of less than 100 km, which should not be the case.

Once the interpolator is set, the aerodynamic coefficients can be added to TUDAT. Using the custom aerodynamic force and moment coefficients function of TUDAT it is possible to apply the previously mentioned interpolator to the simulation. It should be noted that the reference length and reference area in the TUDAT function are set to 1 as the aerodynamic coefficients have the area, and length in the case of the moment coefficients, added to their values. Additionally, as will be explained further on, the moment reference point is set to the origin of the body frame of the satellite. Finally, it is important to note that both the force and moment aerodynamic coefficients are in the body frame and in the positive axis direction. This is required to be specified in TUDAT such that the correct signs and reference frame transformations are done, and the coefficients are applied properly.

7.3. Starlink Properties

The last aspect of the environment to define is the Starlink properties. In TUDAT it is required to define a mass and inertial tensor for the satellite in order for the rotational dynamics to be propagated. In this section, the calculations of the moment of inertia of the satellite will be performed. For the mass, a constant mass of 260 kg is set. For the inertial tensor, the classical calculations will be used. Before the calculations are given, it should be noted that the centre of mass of the main body and the solar panel are assumed to be in their geometrical centre. Additionally, the origin of the body reference frame is defined to be centred at the centre of mass of the main body.

The moment of inertia around the centre of mass of each of the components, which are rectangular, is defined by:

$$\mathbf{I} = \begin{bmatrix} \frac{1}{12}m\left(y^2+z^2\right) & 0 & 0 \\ 0 & \frac{1}{12}m\left(x^2+z^2\right) & 0 \\ 0 & 0 & \frac{1}{12}m\left(x^2+y^2\right) \end{bmatrix} \tag{7.1}$$

where m is the mass of the component and x, y, z correspond to the dimension in the corresponding axis. The axis definition can be seen in Figure 6.2. Following that equation, it is known that for the main body and the solar panel the moment of inertia around their centre of mass are the following:

$$\mathbf{I}_{body} = \begin{bmatrix} 42.77 & 0 & 0 \\ 0 & 169.11 & 0 \\ 0 & 0 & 210.56 \end{bmatrix} \text{kgm}^2 \tag{7.2}$$

$$\mathbf{I}_{panel} = \begin{bmatrix} 460.99 & 0 & 0 \\ 0 & 514.36 & 0 \\ 0 & 0 & 53.42 \end{bmatrix} \text{kgm}^2 \tag{7.3}$$

Now, it is required to calculate the moment of inertia of both of the parts around a specific point. As it was explained in the previous section, the aerodynamic moment coefficients are defined with respect to the origin of the body frame. Thus, for consistency, the moment of inertia of the satellite needs to be calculated around that point too. In order to do so, the Huygens-Steiner theorem is used. The theorem states that it is possible to calculate the moment of inertia of a rigid body about any axis, given the moment of inertia of the body around its centre of mass and the distance between the axes. The equation describing this theorem is the following:

$$\mathbf{I}'_{ij} = \mathbf{I}_{ij} + m(|\Delta\mathbf{x}|^2\delta_{ij} - \Delta\mathbf{x}_i\Delta\mathbf{x}_j) \tag{7.4}$$

where $\mathbf{I}_{ij}$ is the moment of inertia around the ij axis around the object's centre of mass, $\Delta\mathbf{x}$ is the distance vector between the original centre of mass and the new point of interest, and δ_{ij} is the Kronecker delta, which equals 1 if $i = j$ and 0 otherwise. For the current case, Equation (7.4) will be used twice, once for the main body and once for the solar panel. For the main body, as the new point of interest is the same as the centre of mass of the main body, the second part of Equation (7.4) is zero. The calculations for the whole satellite are then as follows:

$$\Delta\mathbf{x}_{panel} = [0, -0.8, -4.8]\text{m} \tag{7.5}$$

$$\mathbf{I}'_{panel} = \mathbf{I}_{panel} + 62.6 \begin{bmatrix} 23.68 & 0 & 0 \\ 0 & 23.04 & -3.84 \\ 0 & -3.84 & 0.64 \end{bmatrix} \text{kgm}^2 \tag{7.6}$$

$$\mathbf{I}'_{panel} = \begin{bmatrix} 1943.3 & 0 & 0 \\ 0 & 1956.7 & -240.4 \\ 0 & -240.4 & 93.5 \end{bmatrix} \text{kgm}^2 \tag{7.7}$$

$$\mathbf{I}_{Sat} = \mathbf{I}_{body} + \mathbf{I}'_{panel} = \begin{bmatrix} 1986.1 & 0 & 0 \\ 0 & 2125.9 & -240.4 \\ 0 & -240.4 & 304.1 \end{bmatrix} \text{kgm}^2 \tag{7.8}$$

7.4. Propagator and Integrator

The next aspect to be considered is the propagator and integrator selection that is used for the current project. A propagator is an algorithm that numerically simulates the motion of a satellite, or object, in orbit during a period of time. All the environment conditions previously mentioned need to be taken into account by the propagator. Thus, it is of key importance to choose a propagator that can properly model the case at hand. In addition to the propagator, an integrator is also required in order to integrate the current state to the next time step. A brief explanation of the propagator and integration selection for TUDAT will now be given. However, before this is the case, an introduction to a number of numerical methods which are used for the propagator and integrator behaviour are explained.

7.4.1. Numerical Methods

Before diving any further into the project it is important to first introduce a number of numerical methods which were of use. This is due to the fact that numerical methods can be used to solve a wide range of problems and often reduce required computational capabilities if applied correctly. The first method that will be introduced is averaging.

Average

The first numerical method to be introduced is averaging. An average is a single number considered to be representative of all numbers of a data set. There are different definitions of an average. The most common one is a weighted average, which is described by the following equation:

$$\bar{x} = \frac{\sum_{i=1}^{n} w_i x_i}{\sum_{i=1}^{n} w_i} \tag{7.9}$$

where $\bar{x}$ is the weighted average value of the data, n is the number of data points being taken into consideration, w_i is the weight of the i of the data points and x_i is the value of the i data point.

Integration

The second numerical method to be introduced is integration. Numerical integration is necessary to propagate the initial state of the object in orbit to a future time. In this thesis, the numerical integrator will integrate the equations of motion introduced in Section 4.5. These EoM have the following form:

$$\ddot{\boldsymbol{x}} = f(t, \boldsymbol{x}) \tag{7.10}$$

To integrate these equations, a number of different numerical integrators can be used. As can be expected, each method will have its advantages and disadvantages. The main differences between the different methods are the step-size that each method uses, it can be fixed or variable, and the number of function evaluations used, also called the order. As it can be expected, the fix step-size methods tend to produce results with less computational cost than those methods with variable step size. However, these results tend to be less accurate results, as the dynamics of the function being evaluated might not be fully noted. Additionally, the higher order methods tend to give more accurate integrations at the expense of being more computationally intensive. As it will be seen later in this section there are a number of different numerical integrators that can be used with each one having its own properties. An analysis on the behaviour of the different methods was performed during the thesis work to choose the integrator that best fits this project.

Differentiation

The third method numerical method is differentiation. The basic concept is to compute the derivative of a function. To calculate the derivative, the differentiation techniques use a method called finite differences. These finite differences are based on the Taylor expansion of the function being differentiated. In general, three main finite difference techniques are used. These are forward differentiation, backwards differentiation and central differentiation. Figure 7.2 shows a visual representation of these techniques. As it can be seen from the image, when differentiating at a given point, forward differentiation only looks at points after the point of interest, backwards differentiation only looks at points before the point of interest and central differentiation looks at points both before and after the point of interest. Central differentiation is usually the most used method as it takes information from both sides of the function, which provides a more accurate approximation of the derivative. Equation (7.11) shows the equation used for the central differentiation.

$$f'(x) = \frac{f(x+h) - f(x-h)}{2h} + O\left(h^2\right) \tag{7.11}$$

where h is a step-size taken for the analysis. It should be noted that sometimes information after a point does not exist. If this is the case, backward differentiation is a good technique to use. Additionally, it is possible to use differentiation to find the derivative of a function with more than one variable.

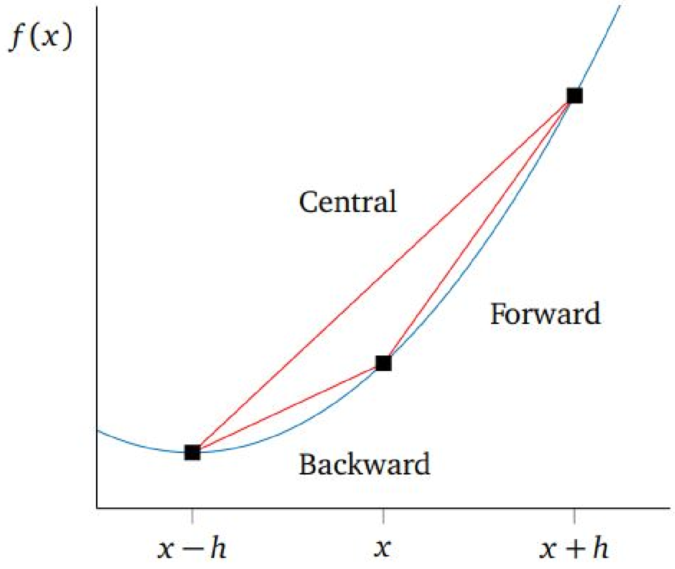

Figure 7.2: Forward, backward and central difference techniques [Wilmott et al. 1995]

Interpolation

The last numerical method to be introduced is interpolation. This method is applied when there are a number of data points but no function defining those points. Interpolation is the process of fitting a curve to those data points in order to be able to find intermediate values. There are a number of different methods, and TUDAT[5] implements the following ones:

- Piecewise constant interpolation
- Linear interpolation
- Cubic spline interpolation
- Hermite spline interpolation
- Lagrange interpolation

As for the integrators, every interpolation technique has its own properties, advantages and disadvantages. During this project, a number of interpolation methods were used. A brief explanation of each of the methods is given when used.

7.4.2. Propagator

now that the numerical methods are clear, it is time to look into the propagators to be used in the simulations. The set of translational and rotational dynamics can use any combination of propagators wanted. The translational propagator available from TUDAT are the following:

- Cowell
- Encke
- Gauss-Keplerian
- Gauss Modified Equinoctial
- Unified State Model (USM)
- Unified State Model (USM) with Rodrigues parameters
- Unified State Model (USM) with exponential map

While the rotational propagators available are

---

[5] `https://py.api.tudat.space/en/latest/interpolators.html` (Last accessed: 17 April 2023)

- Quaternions

All propagators have different advantages and disadvantages. Let us begin with the translational dynamics and the propagators that fit it. First of, the Cowell propagator propagates the full Cartesian state of the object, and the Encke propagates the difference between the state of the body and a reference Keplerian orbit. It can thus be expected that the Encke propagator performs better than when the perturbations are small [Dirkx and Mooij 2019]. Thus, for this project, it can be expected that the Cowell behaves better than the Encke. This is due to the fact that the orbit will decay due to the perturbations, thus the magnitude of these perturbations will not be small. Additionally, the Keplerian propagator might also not be suited for this project. This is due to the fact that there is a singularity for the zero eccentricity case, which could affect this project as the eccentricity of orbits decrease due to the effect of the drag. Furthermore, the USM propagators tend to perform very well. The main concerns with the USM propagators is that there are still singularities, which can be accounted for with different tricks, at the cost of increase complexity when compared to the simple Cartesian formulation. Additionally, as the orbit will be highly perturbed, specially when the altitude is close to the 120 km, the properties of the previously mentioned propagators might not hold. Thus, it is advise to use a Cowell propagator [Dirkx and Mooij 2019], which in the high perturbation cases tends to work well.

For the rotational dynamics, quaternions will be used. In Section 4.4, quaternions and their behaviour were explained. For the current project in TUDAT, the initial state of the satellite will be defined in quaternions, which represent the rotation from body to inertial frame. Additionally, it should be noted that TUDAT defines quaternions differently than those described in Section 4.4. In TUDAT, the dimensionless quaternion, Q_4 is the first one in the sequence of quaternions as per the TUDAT documentation[6]. It is important to keep this in mind to prevent any errors when setting up the initial conditions.

7.4.3. State Model

now that the propagation method is clear, it is necessary to know which state we are propagating. The state being propagated must have all the variables that are of importance to us. Thus, the state to propagate consists of the following variables:

$$\mathbf{X} = \begin{bmatrix} \mathbf{r}_R^T & \mathbf{V}_R^T & \mathbf{q}^T & \boldsymbol{\omega}^T \end{bmatrix} \tag{7.12}$$

where $\mathbf{r}_R$ and $\mathbf{V}_R$ are the position and velocity vectors of the object in the Earth fixed frame. These two parameters represent the translational dynamic. Then, the rotational dynamics are described by **q** which are the 4 normalised quaternions and $\boldsymbol{\omega}$ is the rotational velocity of the object.

7.4.4. Integrator Selection

Finally, in order for the propagation to run, it is necessary to select an integrator. In order to do so, a trade-off had to be performed. This trade-off is performed mainly because of a computational time constraint. A very high degree and low tolerance integrator can be used to get more accurate results, but it is more computationally expensive. Thus, a trade-off is performed to look for an integrator that provides a faster integration time while maintaining a low error. For this trade-off to be performed, first a benchmark orbit was generated. This benchmark orbit was generated using a high-order integrator with variable step size and low tolerances. The benchmark integrator used was a Runge-Kutta 8 (7) with variable step size and tolerance of 1×10^{-14}. The use of this integration precision is limited to the benchmark due to the high computational times. Next, a set of integrators were chosen in order to be analysed.

The integrators to be analysed are the following:

- Runge-Kutta 4 fixed step size
- Runge-Kutta 4(5) variable step size with variable tolerances
- Runge-Kutta 5(6) variable step size with variable tolerances
- Runge-Kutta 7(8) variable step size with variable tolerances

A brief remark on this set of integrators. It is clear that only the Runge-Kutta integrators are used. Other integrators, such as the Bulirsch-Stoer integrator or the Adams-Bashforth-Moulton integrator, were

---

[6] `https://docs.tudat.space/en/latest/_src_user_guide/state_propagation/environment_setup/frames_in_environment.html` (Last access: 17 April 2023)

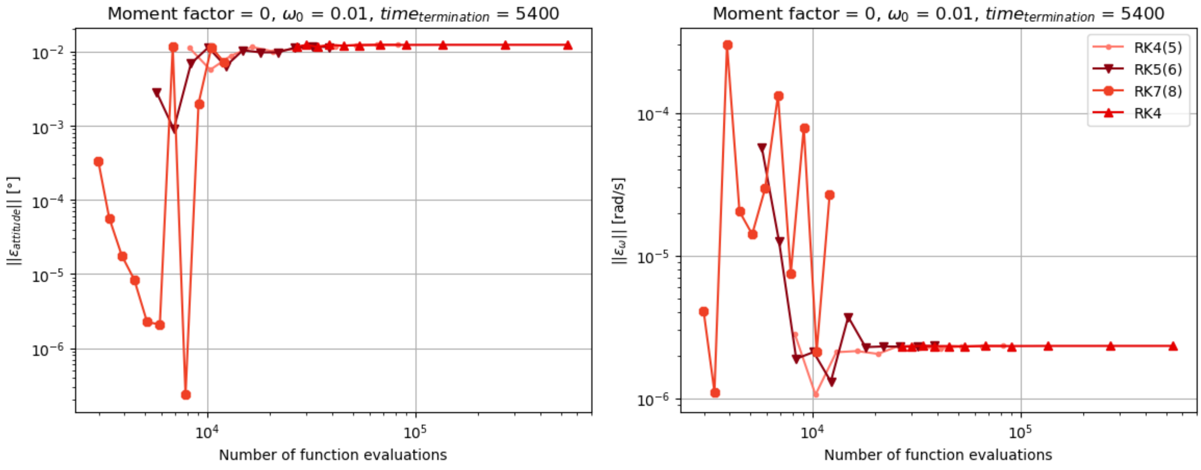

(a) Attitude error **(b)** Angular velocity

Figure 7.3: Behaviour of different integrators with different tolerances for the initial angular velocity of 0.01 rad s^{-1}

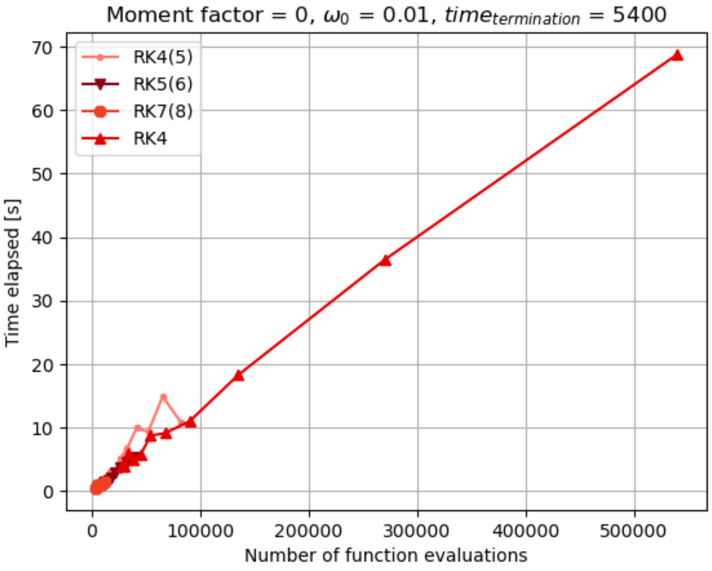

Figure 7.4: Computational time of different integrators with different tolerances for the initial angular velocity of 0.01 rad s^{-1}

left out of the comparison due to the fact that from the literature it is known that the Runge-Kutta tends to perform better [Dirkx and Cowan 2019]. For the trade-off, the simulation that was run was the following:

- Rotational dynamics only
- No atmosphere
- No thermospheric winds
- No moment perturbations
- Initial attitude in Euler angles is zero
- Initial rotational rate of 0.01 rad s^{-1}

As can be seen, the trade-off focused on the rotational dynamics. This is because, from previous simulation runs, it was discovered that the rotational dynamics were significantly faster than the translational ones. This meant that the critical case that the integrator had to model was the rotational dynamics one. The results can be seen in Figure 7.3. A couple of conclusions can be reached. Firstly, as seen in Figure 7.4, the computational time of the Runge-Kutta 4 fixed step size is significantly larger than the rest

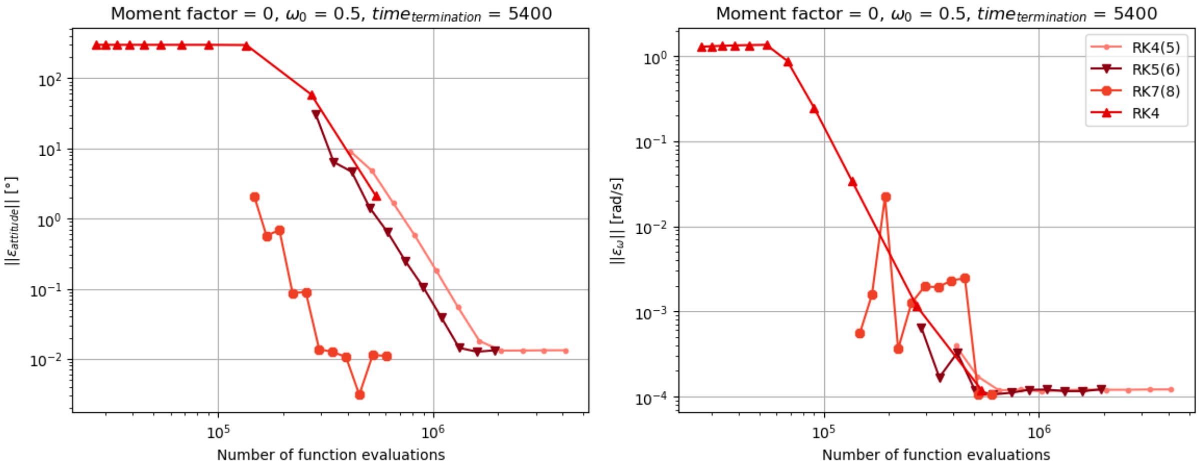

(a) Attitude error

(b) Angular velocity

Figure 7.5: Behaviour of different integrators with different tolerances for the initial angular velocity of 0.5 rad s^{-1}

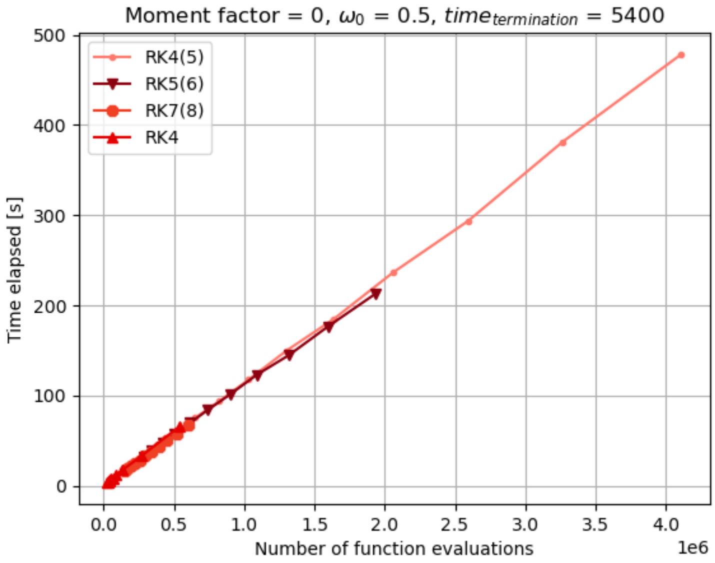

Figure 7.6: Computational time of different integrators with different tolerances for the initial angular velocity of 0.5 rad s^{-1}

of the integrators, with no evident improvement in accuracy. Thus, it can be concluded that the Runge-Kutta 4 is not the integrator for this project. Additionally, the Runge-Kutta 7 (8) error behaviour is chaotic. The error, both for angular velocity and attitude, jumps up and down for the different tolerances. Thus, the Runge-Kutta 7 (8) is also discarded. Finally, between the Runge-Kutta 4 (5) and Runge-Kutta 5 (6) the computational time is fairly similar and so is the error behaviour. Thus, in order to decide which one to use, a look into a more extreme case, with higher angular velocities of 0.5 rad s^{-1}, was used. In this case, seen in Figure 7.5, the Runge-Kutta 5 (6) proved to have a smaller error than the Runge-Kutta 4 (5) for the same tolerance. Thus, the Runge-Kutta 5 (6) was chosen for this project. To be more specific, a Runge-Kutta 5 (6) with variable step size and tolerance of 10^{-10} was selected. Additional cases were then run for different initial conditions of the simulation, such as a random starting attitude, a random initial angular velocity and aerodynamic perturbations activated. The results from these simulations also agree with the previous conclusion that the Runge-Kutta 5(6) with variable step size and tolerance of 10^{-10} had the best behaviour.

Table 7.1: Initial standard deviation of errors at TLE epoch [Geul et al. 2017]

σ_{r_R} [km]	σ_{r_S} [km]	σ_{r_W} [km]	σ_{v_R} [ms^{-1}]	σ_{v_S} [ms^{-1}]	σ_{v_W} [ms^{-1}]
0.46	6.2	0.14	7.6	0.46	0.13

7.5. Initial State Generation

Finally, the only missing parameter for the simulation to be ready is the initial state of the satellite. For the current project, we are interested in both translational and rotational dynamics. This means that the initial state depends on four components. The first two components are the translational position and velocity. These two components will be taken from the TLE data. The other two, initial attitude and initial rotational velocity, will be randomly generated in the simulations. A bit more in-depth explanation of the two components will now be given.

7.5.1. Initial Translational State

As previously mentioned, the translational state will be taken from TLEs. In Section 4.2 the components of the TLE and the information stored in them are explained. For TUDAT, due to the propagator used, the initial translational state needs to be in a cartesian coordinate system with the origin at the centre of Earth. In order to do so, the TLE data needs to be transformed from the Keplerian elements to the cartesian state. Unfortunately, the TLE applications in TUDAT are very limited. Thus, a different tool was used.

The package of Skyfield[7], for Python, was used for the generation of the initial translational state. The usage of Skyfield is straightforward and all the documentation can be found on the website. Of course, verification of the Skyfield output of position and velocity for a given epoch was performed. This was done by looking online at the position and velocity of different satellites at different epochs and verifying that the values of Skyfield and the ones online matched. It should be noted that Skyfield has a wider range of applications, as it also has the SGP4 propagator implemented. However, for the current project at hand, it was only used to generate the initial position and velocity of the satellite for a given epoch in the TLEs.

7.5.2. TLE Errors

Once the TLE has been read and the initial translational state generated, the only thing that is left is to add the errors to the TLE. As the TLE measurements are not exact an error in the initial state is generated. Two options are thus presented in order to introduce the errors into the analysis. The first option is to use pre-calculated errors for TLE data. Papers like those from Flohrer et al. [2009], Yim and Chung [2012] and Geul et al. [2017] provide error distributions and values for the standard deviation of TLEs at different altitude ranges. These values could be used directly in the analysis. The main disadvantage of this method is the fact that each TLE has a different error behaviour. Thus, using the previously calculated errors for all TLE data might not represent the errors accurately enough. The second option that could be considered is to do a process similar to what Geul et al. [2017] did. It could be possible to analyse the TLEs in order to generate error distribution and values for given sets of TLE data. The second option would likely provide more accurate error values as the analysis is performed for the specific TLEs being used in the project.

It was decided to follow with the first option. The main reason is that the amount of time it would take to generate the TLE errors for a specific set of TLEs would be too large for the current project. During the project, a number of different TLEs were used. Generating the TLE error behaviour for each set of data would significantly increase the time spent on the project at hand. Thus, the error behaviour found by Geul et al. [2017] is used. Based on Geul et al. [2017] it is assumed that the errors from the TLEs have a multivariate normal distribution. The errors and their correlation values are in Table 7.1 and Table 7.2.

It should be noted that the previously mentioned analysis will yield errors only for the translational components, position and velocity, and in the RSW frame. As previously mentioned, the initial translational state of the satellite needs to be given in the inertial frame. This means that in order to be able to apply the TLE errors to the initial translational state a reference frame transformation will be applied.

---

[7] `https://rhodesmill.org/skyfield/` (Last accessed: 11 April 2023)

Table 7.2: Correlation matrix for classic TLEs [Geul et al. 2017]

	r_R	r_S	r_W	v_R	v_S	v_W
r_R	1.00	0.04	0.25	-0.02	-0.98	0.06
r_S	0.04	1.00	0.04	-1.00	-0.09	-0.11
r_W	0.25	0.04	1.00	-0.04	-0.30	0.00
v_R	-0.02	-1.00	-0.04	1.00	0.07	0.12
v_S	-0.98	-0.09	-0.30	0.07	1.00	-0.03
v_W	0.06	-0.11	0.00	0.12	-0.03	1.00

This is done in TUDAT by applying the following process:

1. Generate initial position and velocity in inertial frame from a TLE using Skyfield.
2. Generate initial position and velocity errors in the RSW frame using the standard deviation and correlation matrix.
3. Transform the initial position and velocity from the inertial frame to the RSW frame using TUDAT.
4. Add the initial errors in the RSW frame to the initial position and velocity in the RSW frame.
5. Transform back from the new RSW position and velocity to the inertial frame.

Once this process is performed, the initial translational state of the satellite has been fully defined and the only missing aspect would be the initial attitude and rotational rate of the satellite. It is important to note that if a nominal run, which is defined as a run with zero initial error, is desired, the errors from the TLE are simply not generated and the same inertial state is used.

7.5.3. Initial Rotational State

The initial rotational state of the satellite is defined in a more simple way than that of the translational state. The initial attitude is defined by the three Euler angles, pitch, yaw and roll. Once the angles are defined, the $\boldsymbol{C}_{B,I}$ is calculated. Then, the transformation to quaternions is applied. This is done using a function in TUDAT that follows the steps highlighted in Section 4.4. It is important to note that the use of quaternions and the use of $\boldsymbol{C}_{B,I}$ is used as it was decided to use quaternions for the integrator in TUDAT. For the rotational rates, the initial rotational rate is defined per axis with the value of interest in rad s^{-1}.

8

Verification and Validation

The last step before the software is ready to be used is the Verification and Validation of the software. This is done in order to make sure that the system performs its intended purpose properly. As previously seen, there are two main aspects to the software, the TUDAT part and the SPARTA one. Thus, the verification will be split into parts too. Firstly, Section 8.1 will cover the different aspects of TUDAT that required verification. Then, Section 8.2 goes over the verification of SPARTA and aerodynamic coefficient generation. Finally, in Section 8.3 the validation of the whole software is performed.

8.1. Verification TUDAT

Let us start with the verification of TUDAT. As it was previously mentioned, TUDAT is developed by DUT and is used by a number of students. This means that it has already been verified and validated. All the functions of TUDAT have been checked and their outputs validated. This means no verification and validation need to be performed on the output from TUDAT. However, that the functions have been verified and validated does not mean that the user knows how to use them. Thus, acceptance tests need to be performed. These acceptance tests are made in order to make sure that the user is applying the correct use of the previously verified functions. As most of the functions used in TUDAT have been previously developed, it is important to perform these tests. Thus, the first part of this section will focus on acceptance tests. Once these tests have been performed, verification of a function generated by the use of the NRLMSISE-00 will be performed. Next, the thermospheric wind model, which was taken from a wrap online, will also be tested and verified. Finally, the interpolator used for the aerodynamic coefficients is verified.

8.1.1. Acceptance Tests

As previously mentioned, acceptance tests need to be performed to make sure the functions in TUDAT are used as intended. A number of acceptance tests have been performed for the current project. An explanation of these tests will now follow. The results from the tests can be seen in Table 8.1, where a green colour in the compliance column indicates a pass and a red one indicates a fail.

AT-01:Earth Shape

The first acceptance test to be carried out is on the shape of the Earth. As previously mentioned in Section 7.1, the Earth is not a perfect sphere. It is an oblate spheroid with an equatorial radius of 6 378 137 m and a flattening of 1/298.257223563. Thus, it was important to check that when generating the Earth in TUDAT the correct sizing was performed. In order to check that correct sizing was applied, the altitude of a polar orbit with zero eccentricity was checked. The altitude of a satellite in a polar orbit with an oblate sphere should increase as it approaches a latitude of ±90° as the radius of the Earth decreases. Thus, the altitude was saved and compared to analytical results.

AT-02: Earth Gravity Field

The second acceptance test to be carried out is on the gravity field of Earth. The Earth will be modelled with spherical harmonics with degree and order 24, as explained in Section 7.1. Thus, it is of key importance to make sure that TUDAT recreates the desired environment correctly. In order to check that the acceleration is as expected, a simulation is carried out with an orbit at an inclination of 53°, with zero eccentricity and altitude of 300 km. The spherical harmonics accelerations for specific terms are saved, and then the results are compared versus accelerations calculated based on Equation (4.16).

AT-03-01:Solar Radiation Pressure Acceleration

The third acceptance test to be carried out is for the solar radiation pressure. The formulation of solar radiation pressure used in TUDAT is that of a cannonball, which is described in Section 4.5. Thus, in order to check that the force applied is correct for the given reference area and radiation pressure coefficient, all that needs to be checked is the distance vector between the Sun and the Earth is correct. The simulation is performed for an orbit at an inclination of 53°, with zero eccentricity and altitude of 300 km. The distance vector is saved, and the calculations are performed to check if the results agree with the saved acceleration values.

AT-03-02:Solar Radiation Pressure Occulting Body

The fourth acceptance test is also in regard to solar radiation pressure. However, this time it is in relation to the occulting body. At some point in the orbit, the Sun will be ”behind” the Earth, as explained in Section 4.5. Thus, the solar radiation pressure acceleration is expected to be zero for some parts of the orbit. The simulation is performed for an orbit at an inclination of 53°, with zero eccentricity and altitude of 300 km. The solar radiation pressure acceleration is saved, and the values are examined to see if the acceleration is zero at some point in the orbit.

AT-04-01: Third Body Perturbations - Sun

The next acceptance test is in regard to the third body perturbations of the Sun and the Moon on the satellite. As the gravitational attraction of the Sun and the Moon will have an effect on the orbit, it is important to make sure these are applied correctly. Once again, an orbit with an inclination of 53°, with zero eccentricity and altitude of 300 km is used. First, the Sun effect is tested. The distance vector to the Sun is saved along with the standard gravitational parameter, and the analytical calculations are performed to check for the values.

AT-04-02: Third Body Perturbations - Moon

Similar to **AT-03-01**, the same test is performed for the effect of the Moon. Once again, the same orbit is used, but this time the standard gravitational parameter of the Moon and the distance vector to the Moon are saved. The analytical results are compared to the saved accelerations.

AT-05: Aerodynamic Perturbations

The next acceptance test to be carried out is for the aerodynamic perturbations on the satellite, both forces and moments. It is of key importance that not only are the aerodynamic coefficients properly generated, which will be verified further down, but that they are applied correctly to the dynamics. For TUDAT, the *custom_aerodynamic_force_and_moment_coefficients*[1] function was used. In said function, you need to specify not only the aerodynamic coefficients to be used, but also the frame they are in and their positive definition. For the current project, the aerodynamic coefficients are defined in the body frame of the satellite and in the positive axis direction. This means that the equivalent of drag, lift and side force are all negatively defined in the body frame. Once again, a simulation with an inclination of 53°, with zero eccentricity and altitude of 300 km and aerodynamic perturbations activated is run, and the coefficients used are saved. Then, both, the sign and the magnitude, of the aerodynamic coefficients are then checked against the expected aerodynamic coefficients for certain parts of the orbit.

AT-06: Atmospheric Model Built

One of the most important acceptance tests performed for this project was to check that TUDAT was built with the NRLMSISE-00 model properly. To do so, the unit tests in TUDAT are run. These unit tests make sure that the built with a parameter different from the standard has been generated properly. Additionally, as will be seen in the next section, verification and validation were performed to check that the function that takes values from NRLMSISE-00 is working as intended.

---

[1] `https://shorturl.at/boKS2` (Last access: 20 April 2023)

Table 8.1: Acceptance Test Compliance

Acceptance Test	Compliance
AT-01	🟩
AT-02	🟩
AT-03-01	🟩
AT-03-02	🟩
AT-04-01	🟩
AT-04-02	🟩
AT-05	🟩
AT-06	🟩
AT-07	🟩

8.1.2. Verification NRLMSISE-00

Now that the acceptance tests have been performed, it is time to cover the verification done for the different areas applied in TUDAT. The first one will be on the atmospheric model. The NRLMSISE-00 model has been implemented in TUDAT, but the default build of TUDAT does not have it added. One has to rebuild TUDAT with the atmospheric model added in. Thus, firstly, an acceptance test was carried out to check that the build with NRLMSISE-00 was correctly done, as described in **AT-06**. Then, the verification of the NRLMSISE-00 was performed by reproducing Figure 8.2. As can be seen, the image was reproduced using the function generated to extract the temperatures and densities from the NRLMSISE-00. The two figures are compared to the values from Doornbos [2011] which can be seen in Figure 8.1. It should be noted that Figure 8.1 is a copy of Figure 2.1 but for simplicity of the verification it has been placed here again. As it can be seen, the density profile and temperature profile match for the different altitudes. Thus, it was concluded that the NRLMSISE-00 function was working as intended.

8.1.3. Verification HWM14

The next verification that was performed was on the thermospheric wind model. As previously explained, the HWM14 model was taken from an online source that wrapped it to Python and made a library. In order to verify that the HWM14 was installed correctly and that the results are as expected, three verifications were performed. Firstly, the plots seen in the GitHub of the library[2] are recreated. With this test, it is verified that the installation is successful. The second test was to cross-verify the results from the Python version to those from the online NASA tool at CMR [3]. A set of random input parameters were used, and the output from the website and the Python package were compared and verified. Additionally, in order to make sure that the verification against the online source was accepted, an email was sent to the NASA representative to make sure the website was a reliable source. Unfortunately, it was found that the results from the online HWM14 were never verified, and instead, the NASA representative redirected us to the latest version of the HWM14 update paper [Drob et al. 2015]. When looking at the paper, no easily re-creatable plots were found. Thus, it was decided that the verification against the online source was enough.

AT-06: HWM14 Interface

Finally, an acceptance test was carried out. One thing is to have the HWM14 running properly, another is to make sure that the interface between the HWM14 and TUDAT is set up properly. The different inputs and outputs of the HWM14 model have been introduced and explained in Section 7.1. It is of key importance that these correct inputs and outputs are applied from and into TUDAT correctly. In order to verify this was the case, a simple test was carried out. A simulation with an inclination of 53°, with zero eccentricity and altitude of 300 km and aerodynamic perturbations, both translational and rotational, is run and the inertial velocity vector of the satellite is saved. Then, the same simulation is run but this time the HWM14 is also included, and the inputs for the HWM14 model are saved along with the inertial velocity vector. The difference between both velocity vectors is calculated and translated to the vertical frame following the transformations in Mooij [1994]. Then, the HWM14 is run with the previously saved

---

[2] `https://github.com/rilma/pyHWM14` (Last access: 30 April 2022)

[3] `https://kauai.ccmc.gsfc.nasa.gov/CMR/` (Last access: 30 April 2022)

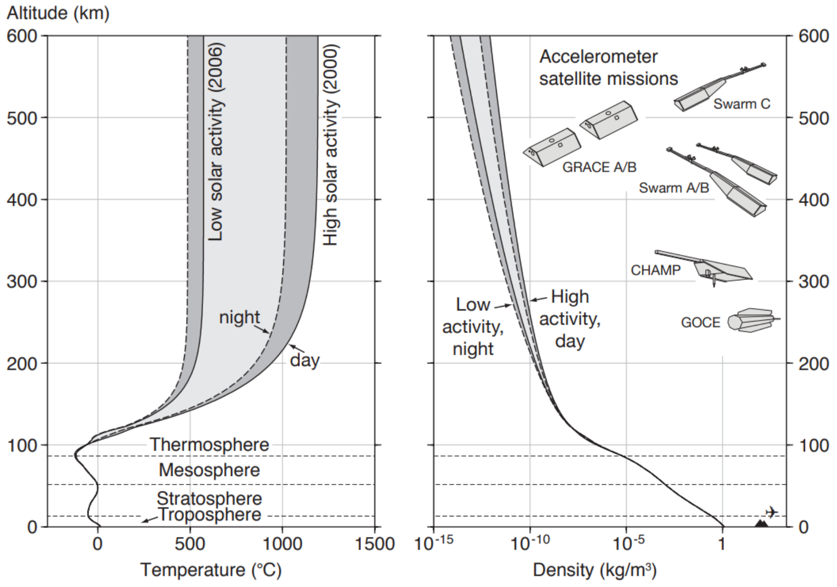

Figure 8.1: Altitude profiles of atmospheric temperature (left) and density (right), according to the NRLMSISE-00 model, evaluated for 18:00 on July 15 2000 and 2006, over Delft, The Netherlands [Doornbos 2011]

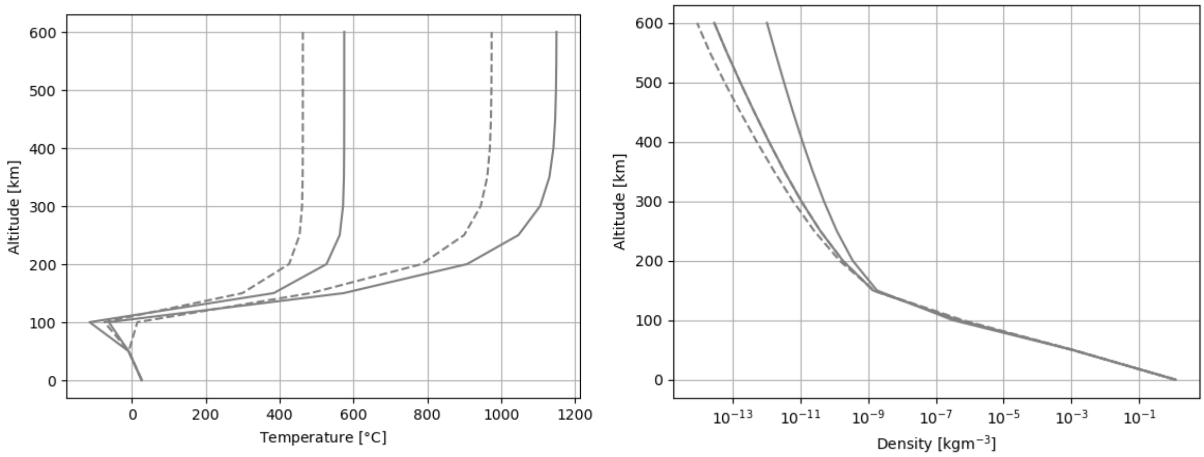

Figure 8.2: Altitude profiles of atmospheric temperature (left) and density (right), evaluated for 18:00 on July 15 2000 and 2006, over Delft

inputs and the final velocity vectors are compared. If the application of the HWM14 is done properly, the results should be the same. This was indeed the case.

8.1.4. Verification Aerodynamic Coefficient Interpolator

The final verification performed for TUDAT was the aerodynamic coefficient interpolator. As previously explained, the aerodynamic coefficient interpolator was generated in order to interpolate the values for the current simulation from the database. The verification of the interpolator was rather straightforward. A number of random speed ratios, densities angles of attack and sideslip angles were chosen. These values were used as input for the interpolator, and the output was compared to results calculated manually. This verification was performed for both the force and moment coefficients. Additionally, at some point, it was considered to change the interpolator in order to reduce computational time, and different Python packages were used to test if lower times could be achieved. The results of these different methods were also saved and compared to the initial values to verify the application of these methods was correct. In the end, the initial interpolator stayed as the other methods did not improve the computational time, but

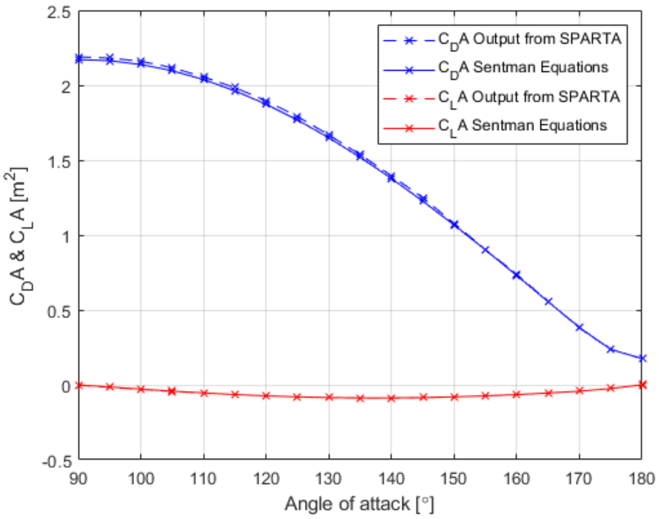

Figure 8.3: C_DA and C_LA coefficients

the results were used as additional verification.

8.2. Verification SPARTA

The second main section of the verification and validation chapter is the verification of SPARTA. As previously mentioned, SPARTA is used to generate the aerodynamic force and moment coefficients. Thus, it is of high importance to verify that the results from SPARTA are correct. As SPARTA is a black box, a set of input parameters gives a set of output parameters, the final result is the one we are interested in. The verification of the force, moment and transition regime will be shown here. Each of the simulations performed in the different subsections has a different set of conditions. They will each be stated and the results analysed.

8.2.1. Verification Force Coefficient

The first verification from SPARTA is the force coefficients generation. As previously explained, the force coefficients from SPARTA are actually force coefficients time area and thus have a unit of m^2. For the verification of the force coefficients, a flat panel will be used. The results from the flat panel are then compared to the analytical values from the Sentman equations described in Chapter 5.

The first step was to generate a rectangular flat panel mesh. This was done using Blender and following the steps described in Section 6.2. The next step is to set up the simulation inputs. The inputs used for the flat plate are generated based on the equations and explanation given in Section 6.3. The Set-up conditions and inputs are the following:

- $nrho$ = 10^{15} m^{-3}
- f_{num} = 1.7280×10^{12}
- box_size = 12
- $grid$ = 100
- $part\_cell$ = 10
- $time\_step$ = 1.5789×10^{-6}
- Only oxygen

It should be noted that only oxygen is used for the verification simulations. This is due to the fact that during the actual simulations in SPARTA this is also done. As previously explained, the speed ratio trick is used. Thus, for the verification, it only makes sense to also use the oxygen composition. Additionally, all the previous values follow from the calculations given a value of $nrho$.

The C_DA and C_LA coefficients are then plotted. The results can be seen in Figure 8.3. As it can be seen, the difference between the analytical and numerical solutions is very small. The maximum

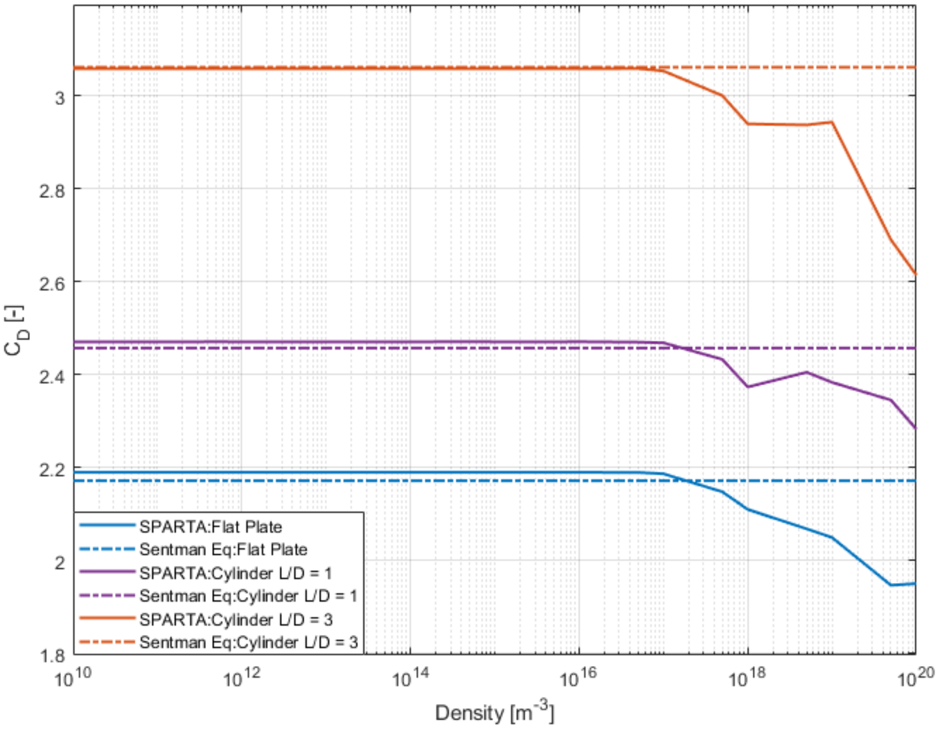

Figure 8.4: Behaviour of C_D for different shapes and different number densities

difference for the C_DA is of 0.0238 m^2 and for the C_LA is of 0.0026 m^2. The discrepancies in the results likely comes from the fact that the analytical equations assume the plate to be infinitely thin, which is not the case in SPARTA. However, the differences are so small that the results are accepted. Additionally, a similar plot can be found in Doornbos [2011] where he also compares the C_DA and C_LA to the Sentman equations and the plots are identical.

8.2.2. Verification Flow Regime

The second verification that is performed is for the flow regime. As there will be different altitudes and thus different densities, it is important to verify that the transition regime behaviour is as expected. In order to do so, the C_DA for three different objects, a flat panel, a cylinder with length to diameter of 1 and a cylinder with length to diameter of 3, are calculated. The simulation set-up conditions and inputs are the following:

- $nrho$ = 10^{10} to 10^{20} m^{-3}
- f_{num} = 1.7280×10^{12} to 1.728×10^{17}
- box_size = 12
- $grid$ = 100
- $part\_cell$ = 10
- $time\_step$ = 1.5789×10^{-6}
- Only oxygen

The results can be seen in Figure 8.4. The results are in agreement with the results from Mehta et al. [2014] which can be seen in Figure 8.5. It should be noted that Mehta has normalized the C_DA with respect to the area, and thus only the C_D is compared for these plots. The output from SPARTA had to be tweaked by dividing the output C_DA by the reference area in order to get the same values. Nevertheless, the behaviour of the different cylinder ratios and the flat plate is in good agreement between both plots. Additionally, the analytical solution is also very close to the numerical solution until the transition regime starts around 10^{17} m^{-3} and the equations for the free flow regime break down. The results can therefore be said to be verified.

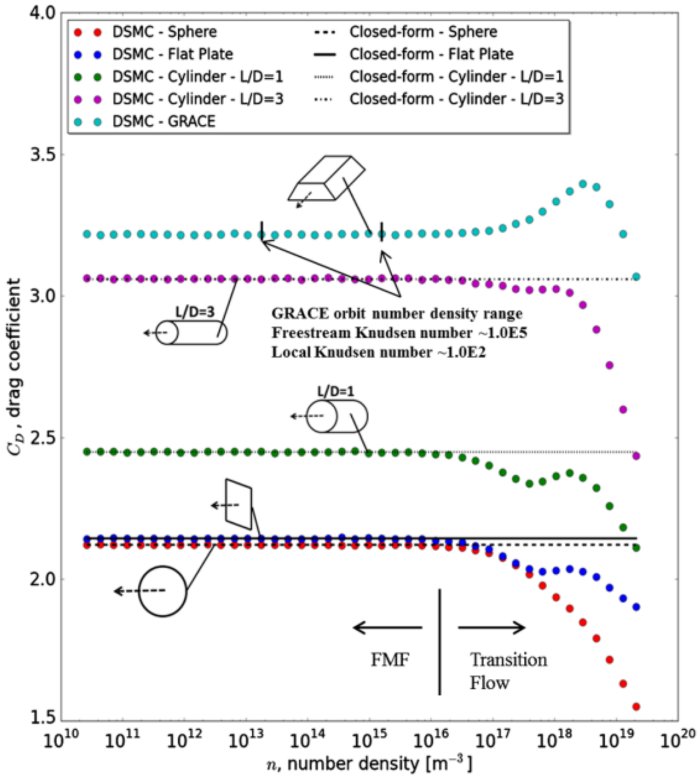

Figure 8.5: Comparison of the free molecular closed-form solutions to DSMC results into the transition flow regime. The flow changes from free molecular to transition at a number density of 1E16 [Mehta et al. 2014]

Furthermore, it is interesting to talk about the behaviour of the C_D. As it can be seen, for densities lower than 10^{16} m^{-3}, the coefficients for all three shapes are constants. The transition regime starts at about 10^{17} m^{-3} and ends before 10^{20} m^{-3}. The lower bound of the number density corresponds to an altitude of about 100 km, which is well below the altitude for this project. Thus, this verification was also used to select the range of values of number densities for this thesis.

8.2.3. Verification Moment Coefficients

The last verification to be performed is for the moment coefficients. It is of key importance to make sure that the moment coefficients are calculated correctly, as they will be part of the aerodynamic torques acting on the satellite. Thus, a similar process to that for the transition regime and force coefficients will be performed. It should be noted that it was rather hard to find any plots to use for the verification of the coefficients. Most of the papers found during the literature study had some calculations of the moment coefficients but for very complex shapes. These complex shapes also meant that the mesh had to be designed properly as well. Instead, the paper from Hart et al. [2014] was used. in said paper, the authors generate the moment coefficient for a number of different shapes. The process is not very clear, but after choosing different reference points for the moments, the results were able to be recreated. In order to recreate said results, the following set-up was used:

- $nrho$ = 10^{10} m^{-3}
- f_{num} = 1.7280×10^{12}
- box_size = 12
- $grid$ = 100
- $part\_cell$ = 10
- $time\_step$ = 1.5789×10^{-6}
- Only oxygen

The shape used for the verification of the moments was a stepped cylinder. Said stepped cylinder had the dimensions seen in Figure 8.8. The moment coefficient is calculated at the lower left ”corner” of

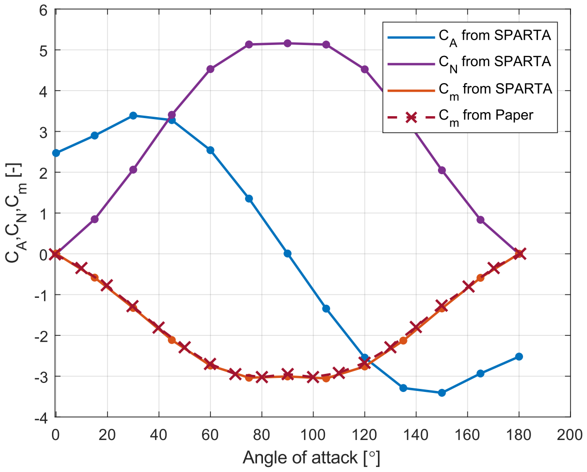

Figure 8.6: C_A,C_N and C_m forces and moment coefficients for a stepped cylinder

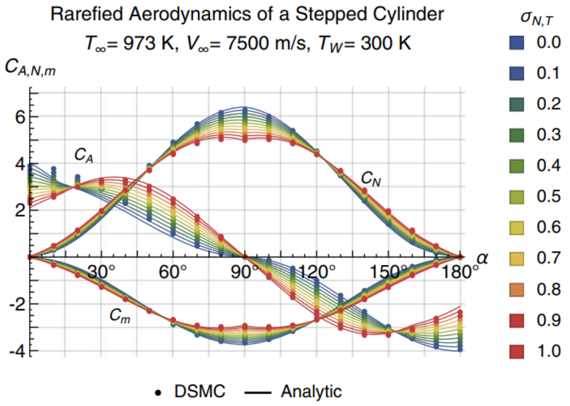

Figure 8.7: Validation of the aerodynamic coefficients of a stepped cylinder [Hart et al. 2014].

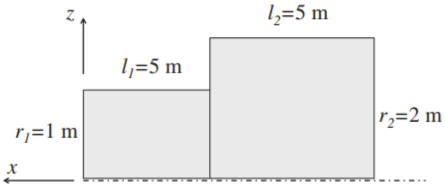

Figure 8.8: Stepped cylinder dimensions [Hart et al. 2014]

the image, where the x and z axis lines are coming from. The results of the simulation can be seen in Figure 8.6 while the plot from the paper from Hart et al. [2014] can be seen in Figure 8.7. The plot from the graph might be hard to read at first, but the line that is interesting is the red line, for which the $\sigma_{N,T}$ is set to one. The coefficients C_A and C_N are the force coefficients in the x and z-axis of the body frame of the object, and the coefficient C_m is the moment around the y-axis of the body frame. Additionally, both the C_A and C_N have been normalized with respect to the area to get a unitless coefficient from the SPARTA output. The moment coefficient, C_m, was normalized with respect to the area and distance to the lower left ”corner”.

As it can be seen in Figure 8.6, the force coefficients are in agreement between the output from SPARTA and the results from Hart et al. [2014]. This further reinforces the idea that the force coefficients are properly generated. When looking at the moment coefficients, the values from the paper have also been plotted in Figure 8.6. As it can be seen, the value of C_m from the SPARTA post-processing is in agreement with the values from the paper. Thus, the moment coefficients are said to be verified. just to make sure no mistake was made, the C_m coefficient was also calculated for a cone and compared to the results from Hart et al. [2014]. The results are not shown in this thesis, as said results once again agree with each other. The only downside from this verification is that only one of the moment coefficients has been verified. However, as there is a dependency between the force coefficients and the moment coefficients due to the vectorial distance playing a role at the moment coefficients, if one of the coefficients is correct for two different cases, it can be assumed that the other two coefficients are also correct.

8.3. Validation Software

Once all the verification of the smaller areas of the software has been performed, a final validation of the complete software is performed. This validation is performed in order to make sure that even though all smaller aspects work as intended, the whole software also does work as it is expected. As can be expected, validation of the whole software is rather hard. This is due to the fact that the only information

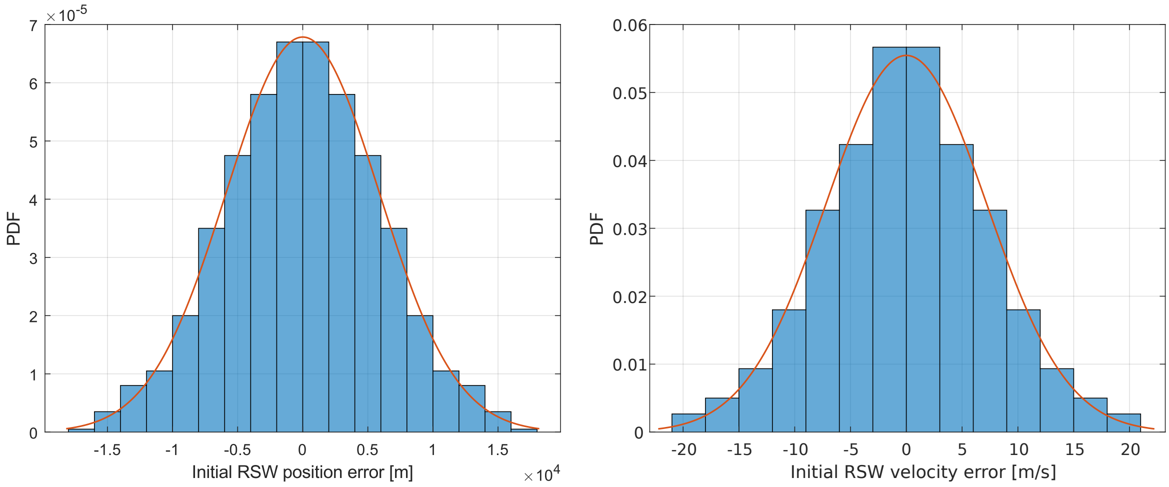

(a) Position

(b) Velocity

Figure 8.9: Histograms for the initial TLE error behaviour

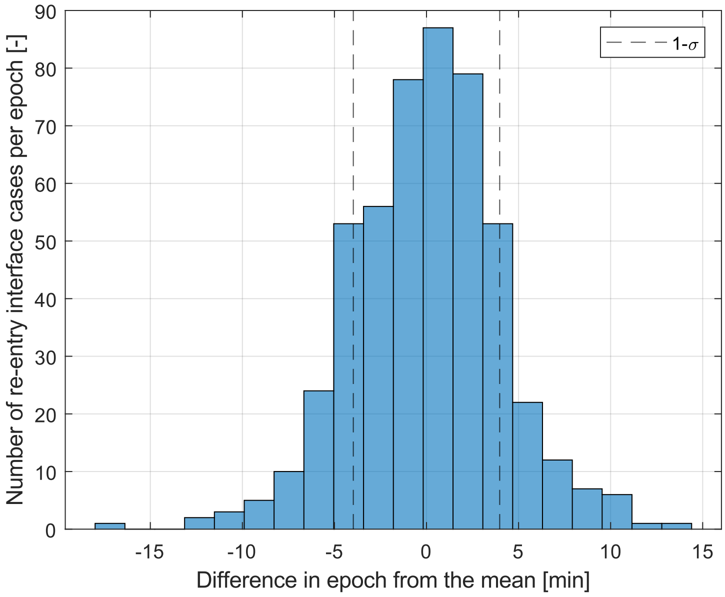

Figure 8.10: Histogram for the difference in re-entry epoch for different initial TLE errors

available is the TLE data. Thus, there is information on the last known position and velocity of the satellite, but there is nothing on its re-entry. Thus, for the current validation, what was decided to be performed was to run two different simulations. An explanation and analysis of results from both of these simulations will be given in Section 8.3.1 and Section 8.3.2 respectively.

8.3.1. Simulation V&V 1: Fixed Inertial Attitude

The first simulation consists of running the translational and dynamics, but a constant inertial attitude is taken. In this case, all three inertial angles, pitch, yaw and roll, are set to 0° and the aerodynamic moments are set to 0 to prevent any changes in the angular velocity of the satellite. Additionally, an initial TLE error is also used. The simulation is run until the satellite reaches an altitude of 120 km. Then, the final epoch is recorded and a comparison of the different epochs is then performed. The results from the propagation are then used to validate the rotational and translational dynamics.

The results from the simulation can be seen in Figure 8.10. It can be seen that the epoch difference

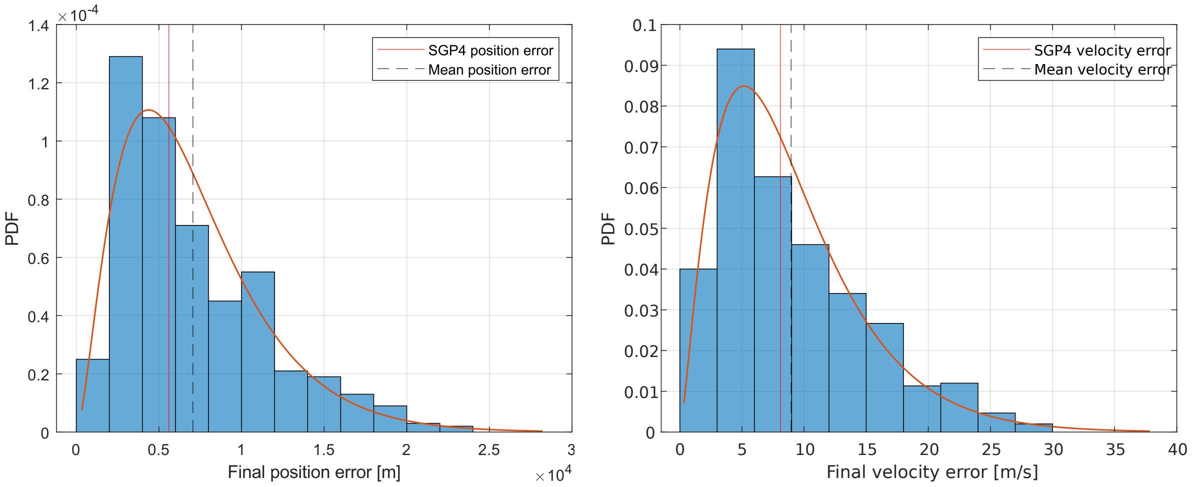

(a) Position **(b)** Velocity

Figure 8.11: Histograms for the difference in the final translational state of the propagation versus the TLE data

Table 8.2: Initial TLE for Simulation V&V 2

STARLINK-5066
1 55424U 23014AK 23044.31593119 .17017551 43578-5 42645-2 0 9997
2 55424 69.9915 53.4310 0006040 196.8570 192.1954 16.28763011 3147

Table 8.3: Final TLE for Simulation V&V 2

STARLINK-5066
1 55424U 23014AK 23044.37237465 .18318819 43709-5 37005-2 0 9994
2 55424 69.9823 53.2471 0007250 179.4720 180.7030 16.31041054 3158

follows a normal distribution centred at around the mean. This is somewhat surprising as, even though the TLE error input follows a normal distribution, the behaviour of the satellite in the orbit is highly not linear. However, as the aerodynamic coefficients acting on the satellite are constant, it is expected that the distribution is somewhat normal as the re-entry interface will depend on the initial state error only. Additionally, due to the inertial attitude being constant, the satellite is rotating with respect to the flow as the aerodynamic angles, angle of attack and sideslip angle, will be changing throughout the whole simulation. The rate of change of these angles will be small, 360° over one orbital period, which at around 120 km altitude is of around 5213 s, thus a change of $0.07\,^{\circ}\,\mathrm{s}^{-1}$ is expected. The initial TLE errors, both in position and velocity, can be seen in Figure 8.9.

As can be seen in the position and velocity error graphs, the initial TLE errors have a normal distribution. This is a good verification that the application of these errors is done properly. Additionally, it can be seen that for a fixed inertial attitude, the epoch error is also a normal distribution. This output was expected, to some extent. The process through which the TLE error is propagated is not linear, in fact, it is very non-linear, and therefore the end distribution could be anything. However, as the rotational rate of the satellite is fixed to maintain a constant inertial attitude, it was expected that some sort of normal distribution could occur. This is due to the fact that the dynamics could be considered, to some extent, constant in the sense that only the initial state changes.

8.3.2. Simulation V&V 2: Validation Versus Other TLE

The second simulation consists of running translational and rotational motion dynamics for a given initial TLE and the corresponding TLE error until the satellite reaches the next TLE epoch. At the final epoch, the position and velocity of the propagated TLE are then compared to the position and velocity of the TLE at the final epoch. These values are then saved and compared. Additionally, the initial TLE is propagated using the SGP4 for a nominal case, so no initial TLE error and the final velocity and position at the second TLE epoch are saved too. The SGP4 propagation value is then compared to the results from the TUDAT propagation. The two TLEs used for the propagation are Table 8.2 and Table 8.3 respectively.

Once again, the results from this simulation are expected to follow some sort of normal distribution. This is due to the fact that, similar to the previous simulation, the TLE errors are known to follow a multivariate distribution. The main difference between the simulations is the rotational dynamics. For the second simulation, the rotational dynamics are also propagated with the corresponding aerodynamic moments. This means that an initial state change could result in very different rotational dynamics and thus a completely different final distribution. As previously mentioned, the dynamics of the propagation are very non-linear, thus the output could take any shape. The results from simulation 2 can be seen in Figure 8.11.

As can be seen in the final position and velocity error, both graphs follow a similar pattern. Both graphs present some skewed normal, or gamma, distribution behaviour. This is partially expected, as once again, the initial TLE errors follow a multivariate normal distribution. Additionally, what is important to note in these two graphs is that when the SGP4 propagation was performed under nominal conditions, so no initial TLE error, the value of the final SGP4 error is very close to the mode of both distributions. This result from the SGP4 is the best validation that can be performed for the current project at hand. The results of both simulations agree to a good degree, and thus the software can be assumed to be fully verified and validated. It is now time to move into the results part of the thesis.

Part III

Results

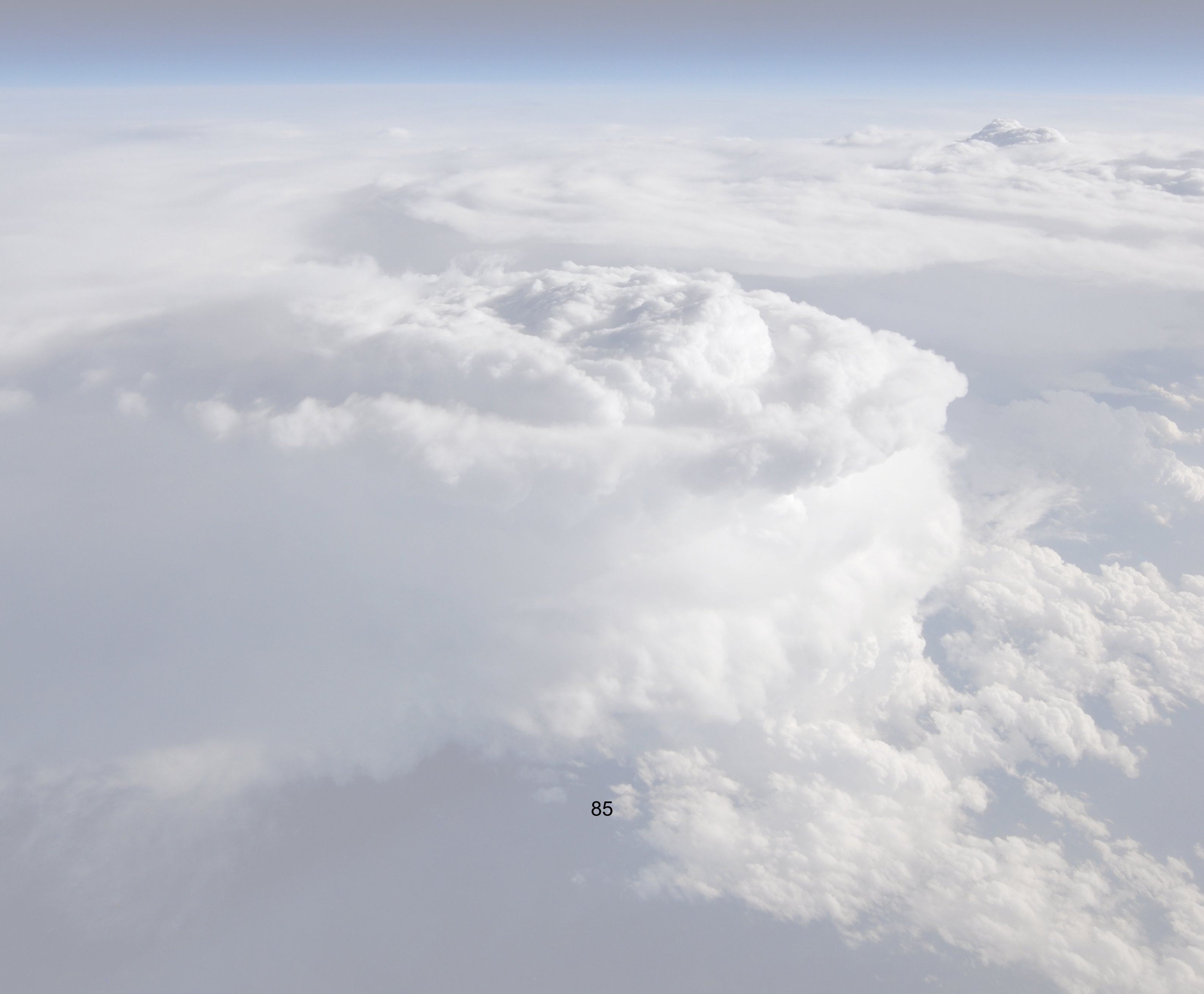

9

Simulation Results

The priority of this research is to examine the influence of a more accurate aerodynamic modelling and initial state, translational and rotational, uncertainties in the re-entry prediction epoch of satellites, using Starlink as a case study. Thus, before this chapter continues, let us have a small resume of all the information gathered in the previous sections and how the simulations that will be explained further in this chapter link to the research questions.

In the previous chapters, all the information required to model the environment in which the orbit of Starlink takes place has been introduced. The physical aspects, such as the shape of the Earth, the atmospheric and thermospheric wind model and the physical parameters of the satellite have been detailed and an explanation of how they have been applied is given. Additionally, the perturbations that can be expected while in orbit are also presented. Finally, verification and validation of all the software have also been performed. This means that the software is ready to run all the necessary simulations. However, before that happens, let us remember the research question:

To what extent is it possible to improve the re-entry epoch prediction by using more accurate aerodynamic modelling of the object in orbit while also taking into account initial state, translational and rotational, uncertainties such that impact analysis on Earth will be more accurate and reliable?

From the research question, it is then possible to also define the research objective, which is:

To achieve an improved re-entry epoch prediction by means of applying a more accurate aerodynamic model of the object in orbit and taking into account initial state uncertainties to have a better impact prediction on Earth.

With this in mind, it is possible to set out a number of batches of simulations that will help us answer the main research question. Firstly, in Section 9.1, the first batch of simulations which will generate results for a constant aerodynamic angle case is analysed. The rotational motion will be ignored and the results from the initial TLE error for a random initial, and constant, aerodynamic angle are shown. Next, in Section 9.2 a batch of simulations in which a random initial attitude is given and no TLE errors are present is shown and analysed. Following the information gathered from two previous sections, in Section 9.3 the results from a batch of simulations in which a random attitude plus the TLE errors are shown. Next, in Section 9.4, an analysis of how the re-entry epoch changes based on which TLE is taken is presented. Finally, in Section 9.5, a comparison between the predicted re-entry of Starlink 1181 made with this software and the values from the ESA prediction software is performed.

Lastly, before the results are shown, in Table 9.1, all the simulations and their characteristics are given. This is done in order to have a compact overview of all the simulations that are carried out in this section. When in doubt of the characteristics, this table can be consulted to see what are the properties of the simulation in question. It is important to note that the aerodynamic acceleration and aerodynamic torques are considered to be included in the corresponding dynamics. Additionally, the type of propagation shown is, either translational, rotational or both. Furthermore, if the initial state has TLE errors, it will also be

Table 9.1: Explanation of the Simulation conditions

	Simulation					
	1.1-1.5	1.6	2	3	4	5
Starlink ID	5066	5066	5066	5066	5066	1181
Translational dynamics	On	On	On	On	On	On
Rotational dynamics	Off	Off	On	On	On	On
Fixed aerodynamic angles	Yes	Yes	No	No	No	No
TLE Error	No	Yes	No	Yes	Yes	Yes

stated. Finally, for Simulation 5 a different Starlink satellite is used, thus the Starlink satellite is also shown for all simulations. It should be noted that all the simulations have the same environment and the same general perturbations. Said set-up is defined by the following parameters:

- **Environment:**
  - Oblate Earth
  - NRLMSISE-00
  - HMW14
- **Perturbations:**
  - Earth spherical harmonics (24,24)
  - Third body perturbations of Sun and Moon
  - Solar radiation pressure
  - Aerodynamic accelerations (If translational dynamics on)
  - Aerodynamic torque (If rotational dynamics on)

9.1. Simulation 1: Constant Aerodynamic Angles

The first batch of simulations will consist of simulations with a constant set of aerodynamic angles. This means that the value of the aerodynamic angles for each different simulation will be fixed at the start of the simulation and then kept constant for the whole propagation. This is done in order to get an idea of how the satellite behaves if the aerodynamic angles, and thus aerodynamic forces, are kept constant. This is a very similar situation to when using the constant ballistic coefficient parameter, which is what is currently done. The results from the different angles will, hopefully, give insight into the behaviour of the satellite.

9.1.1. Simulation 1 Set-Up

The simulation set-up for this batch is the following:

- **Dynamics:**
  - Translational propagation with fixed aerodynamic angles
- **Initial State:**
  - Initial position and velocity from TLE
  - TLE error for position and velocity
  - Fixed angle of attack
  - Fixed sideslip angle
  - Bank angle set to 0°
- **Termination Condition:**
  - Altitude of 120 km
- **Number of Simulations**
  - 250 Simulations per aerodynamic angle set

It should be noted that the aerodynamic accelerations are present, but the aerodynamic torques are not. It is also important to note that the termination condition of 120 km is geocentric altitude. This applies to all termination conditions of all simulations.

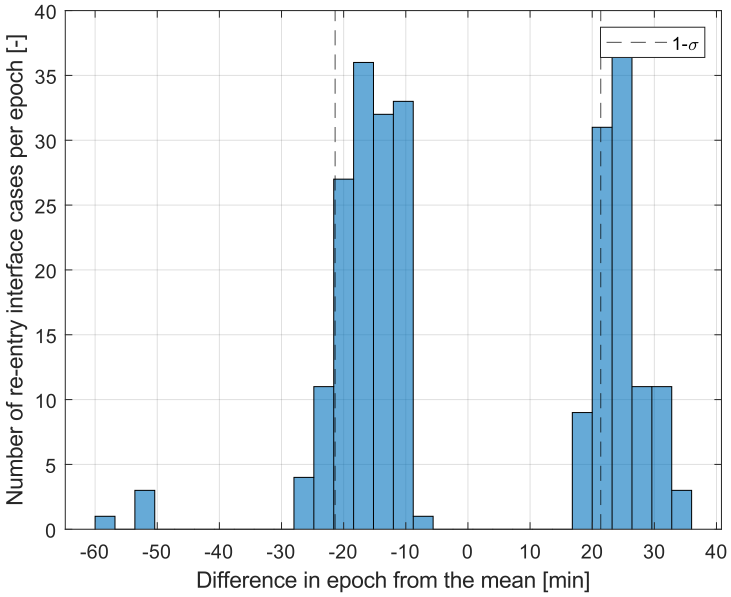

Figure 9.1: Epoch difference for Simulation 1 with α,β = 0°

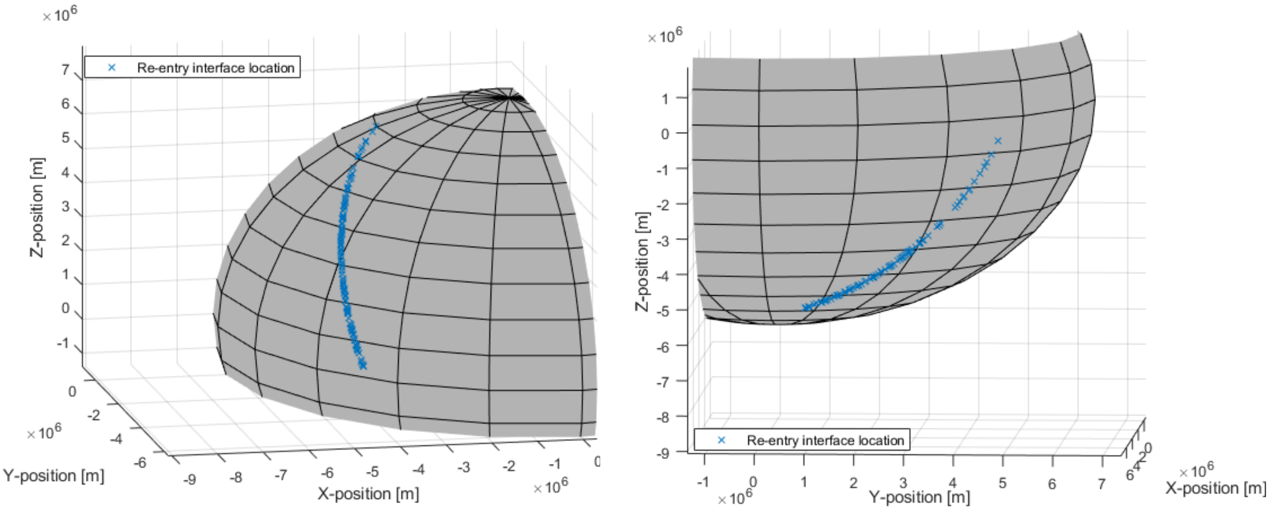

(a) Re-entry interface for the higher latitudes

(b) Re-entry interface for the lower latitudes

Figure 9.2: Re-entry epoch interface position for Simulation 1

9.1.2. Results Simulation 1

The first batch for simulation 1 consisted of having both aerodynamic angles, the angle of attack and the sideslip angle, fixed to 0°. The difference in the epochs from the mean can be seen in Figure 9.1. As can be seen in the plot, there are two peaks, at around -20 and 20 min from the mean epoch. This result is rather surprising, as it is completely opposite to what was previously obtained in the verification and validation chapter. Thus, a bit more research was done to understand why this behaviour happened.

The first step was then to plot the re-entry interface location of all the simulated orbits. As can be seen in Figure 9.2, the re-entry interface happens only when the satellite passes either pole and approaches the equator. This was rather surprising, but now it made sense that there were no re-entries at the mean epoch. When looking at why this could happen, the first idea that comes to mind is the shape of the Earth. For the current simulation, the oblate Earth from the WSG84 model is used. The effect of using this model is that due to the flattening of the Earth, the surface of the Earth gets closer to the center of mass as the

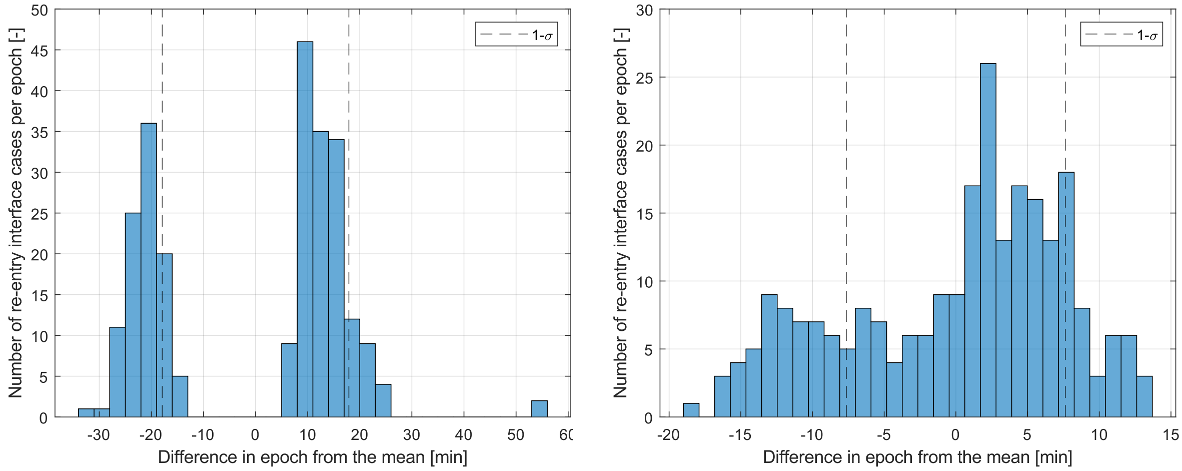

(a) Simulation 1.1, α = 8°, β = 0°, L/D ratio = 0.0487

(b) Simulation 1.2, α = −178°, β = 16°, L/D ratio = 0.007

Figure 9.3: Histogram for epoch difference for Simulation 1.1 and Simulation 1.2

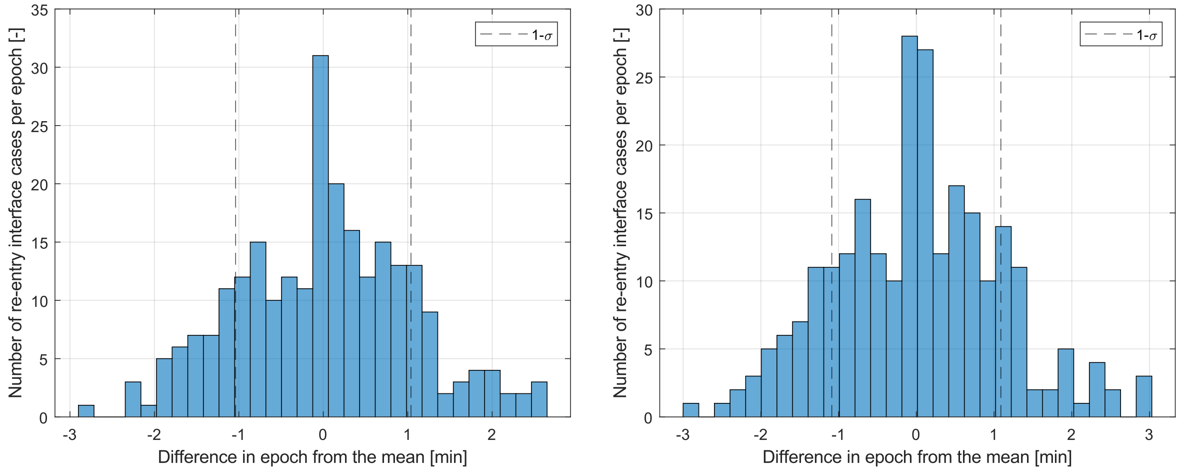

(a) Simulation 1.3, α = 6°, β = 84°, L/D ratio = -0.0041

(b) Simulation 1.3, α = 40°, β = 80°, L/D ratio = -0.002

Figure 9.4: Histogram for epoch difference for Simulation 1.3 and Simulation 1.4

satellite increases latitude from 0 to 90° and decreases from 0 to −90°. As the termination condition of the simulation was the altitude, for the specific case in which the angle of attack and the sideslip angle are both set to 0° the decrease in altitude when passing over the equator and approaching each pole, is slower than the effect of the flattening of the Earth. This meant that the altitude kept increasing even though the satellite was decaying. The idea of the flattening of the Earth playing a role is also supported by the fact that close to the pole, where the gradient of the flattening is less, there are fewer re-entry interfaces, and these interfaces concentrate towards the equator.

Once this was found out, it was of a lot of interest to find for which set of angles this was the case. The first idea was then to look at the set of L/D ratios for all combinations of the angle of attack and sideslip angle in the database of coefficients from SPARTA. This was done in order to assess if the L/D ratio was the most important parameter. For reference, the L/D ratio for the angle of attack and sideslip angle 0° is -0.00099. The negative means that for this combination of angles, the lift is acting in the positive Z_{aero}. Now, a number of different angle combinations are analysed to see if for the different L/D ratios the results are similar. The theory is that for a L/D ratio closer to zero than -0.00099 the difference in epochs should, at some point, start converging towards the mean epoch of that batch. In order to prove this, the following angle combinations were tested:

- **Simulation 1.1**
  - Angle of attack = 8°
  - Sideslip angle = 0°
  - L/D ratio = 0.0487
- **Simulation 1.2**
  - Angle of attack = −178°
  - Sideslip angle = 16°
  - L/D ratio = 0.0070
- **Simulation 1.3**
  - Angle of attack = 6°
  - Sideslip angle = 84°
  - L/D ratio = -0.0041
- **Simulation 1.4**
  - Angle of attack = 40°
  - Sideslip angle = 80°
  - L/D ratio = -0.0020

The results from these simulations can be seen in Figure 9.3 and Figure 9.4. It was expected that for large values of the lift-over-drag ratio, such as simulation 1.1 which has the highest possible L/D ratio, the results would be centred in two peaks. Additionally, for simulation 1.2 in which the L/D ratio is smaller than for simulation 1.1, the results resemble a normal distribution, but it can be seen that there is a peak at around -12.5 min. This suggests that there is indeed a correlation between the L/D ratio and the behaviour of the two peaks. Furthermore, when looking at simulations 1.3 and 1.4, which have a small negative L/D ratio, it can be seen that the distributions of the epochs are centred around the mean. This is also expected as the L/D ratio is very small, smaller than that of simulation 1.2. However, these results do not explain why for the angle of attack and sideslip angle equal to 0° there are two peaks when the L/D ratio of that case is the closest one to zero.

The answer to that question comes from looking at the total magnitude of the drag. In the specific case of the angle of attack and sideslip equal to 0° the L/D ratio is almost zero, but the absolute value of the $C_D A$ is the smallest one there is, equally small as for an angle of attack equal to ±180° and sideslip equal to 0°, with a value of 5.34 m^2. This is due to the fact that at these three orientations, the flow is aligned with the smallest surface area possible with respect to the flow and thus the drag coefficient, and the area with respect to the flow, are both the smallest, which leads to the smallest $C_D A$ acting on the satellite. This means that even though the L/D ratio is very small, and the distribution should be centred around the mean of the epochs, it is not. In order to test this theory, a simulation with the angle of attack equal to −180° and sideslip equal to 2° was run. The results from this simulation can be seen in Figure 9.5. This simulation was run as for this angle configuration the L/D ratio is equal to -0.0019, which is almost the same as simulation 1.4, but the total $C_D A$ is of 5.82 m^2. The results show that the total $C_D A$ also plays an influence in the epoch distribution when the L/D ratio is not very high. These results will be further supported by the results from simulation 1.5

9.1.3. Simulation 1.5

For the next batch of Simulations 1.5, what was done was to run 2000 simulations with a random initial set of aerodynamic angles that were kept constant throughout the simulation. The same conditions as the ones described in Section 9.1.1 are used, only the number of simulations is changed to 2000 and no TLE initial state error is applied. This is done to fully understand the effect of the fixed aerodynamic angles before adding more uncertainties to the equation. The final epochs are recorded and compared. The results can be seen in Figure 9.6. As can be seen, it seems like a skewed normal distribution centred at around -154 min. It would be interesting to understand why this is the case.

The first thing that was looked into was the L/D ratio. A plot showing the relationship between epoch difference from mean and the L/D ratio of each of the selected aerodynamic angles is shown in Figure 9.7a. As it can be seen, there seems to be no relation. For some small values of the L/D ratio, close to 0, the epoch difference values seem to be close to -154 min. However, there are also some cases for the small L/D ratio that have epoch differences of up to 600 min. Thus, no clear correlation has been

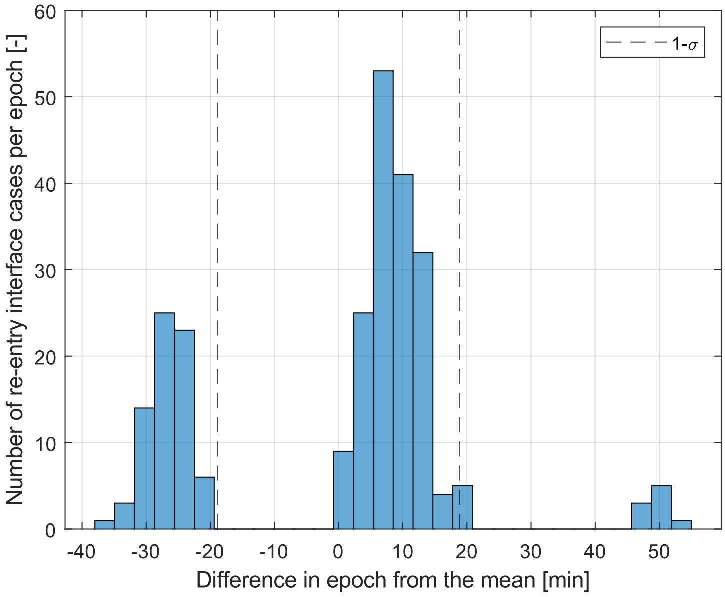

Figure 9.5: Histogram for epoch difference for α = −180°, β = 2°, L/D ratio = -0.0019

found. Now, referring back to the previous simulations, it was found that the C_DA also seemed to have an essential influence on the results. Thus, the epoch difference is also plotted versus the C_DA of the selected aerodynamic angles. The results can be seen in Figure 9.7b. In this case, there is a clear relationship between the C_DA and the epoch difference. The higher the absolute value of the C_DA, the closer to the -154 min the simulation re-entry epoch difference is. Thus, the results from the previous section, in which it was suggested that the C_DA was of more relevance than the L/D ratio, are backed by the results shown here.

9.1.4. Simulation 1.6

Now that the effect of the drag and the different aerodynamic angles has been studied, the last batch of simulations that will be performed is for constant aerodynamic angles, but the initial state TLE errors will also be added to the simulation. Once again, 2000 simulations are performed for a random aerodynamic angle configuration with TLE errors, both in position and velocity, being added in the initial state. The results can be seen in Figure 9.8. When compared to the previous plot in Simulation 1.5, it can be seen that the results are very similar. The main change is that the histogram for Simulation 1.6 is a bit more shifted to the right, with a higher number of epochs having a difference of less than 0 min. Once again, the behaviour of the C_DA was investigated, along with the initial position and initial velocity TLEs. The results can be seen in Figure 9.10.

As it can be seen, there is no dependency in the initial TLE error, neither in position nor velocity, with the difference in the final epoch. The main effect is due to the C_DA. This can be seen as the larger the absolute C_DA, more negative than $-60\,\mathrm{m}^2$, have a darker colour, due to the re-entry epoch time being before the mean epoch, while the lower C_DA, below $-10\,\mathrm{m}^2$, have a lighter colour due to the epoch difference being over 1000 min in some cases. One final observation is to be made. This is in regard to the maximum epoch difference. The maximum value comes out to 1607 min difference, which is about 26 h and 48 min. This means that the Earth has had enough time to do a full rotation around its axis, and the re-entry position is very similar to some of the previous results. However, for the other different epochs, this is not necessarily the case. This means that there is a very wide range of possible positions for the re-entry interface to begin. To better visualise this, all the final longitudes and latitudes for Simulation 1.6 have been plotted in Figure 9.9. As can be seen, the possible re-entry interface position takes a wide range of values, which is a problem when attempting to calculate the final re-entry position of the satellite.

The main conclusion that can be achieved from Simulation 1 was that the C_DA plays a significant role

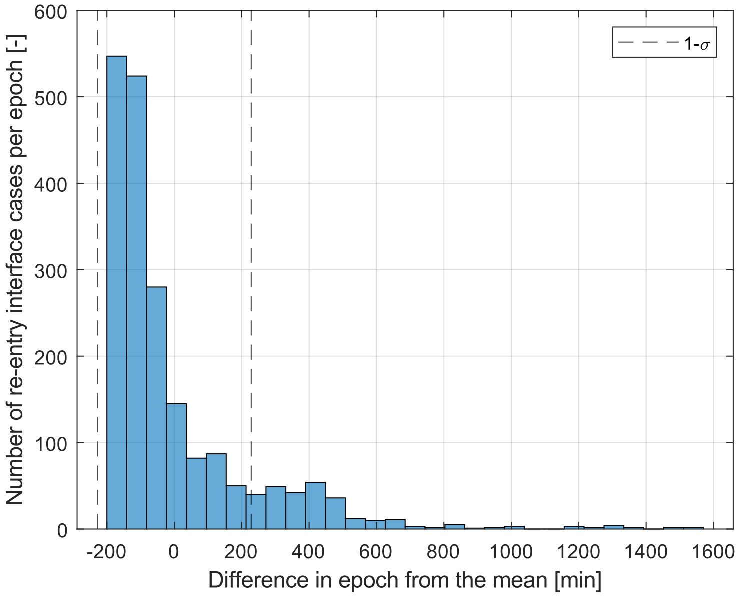

Figure 9.6: Histogram for epoch difference for simulation 1.5

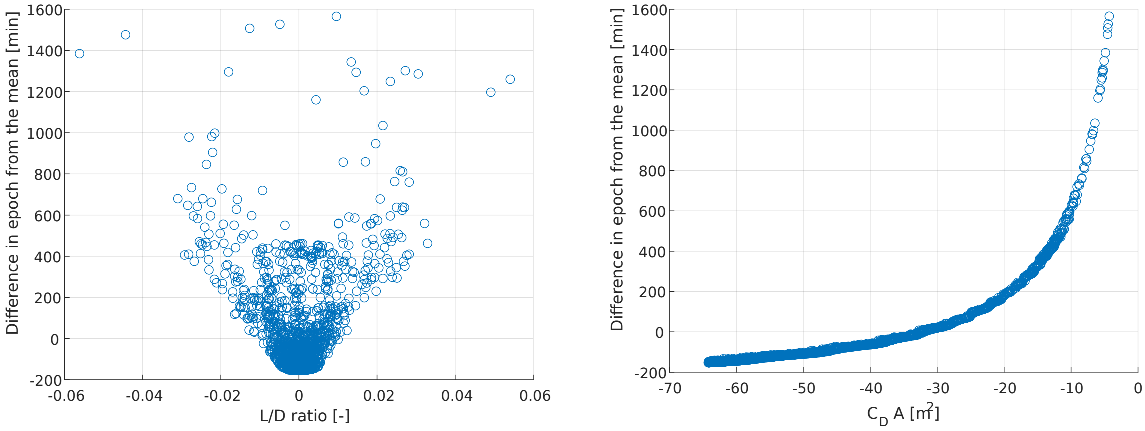

(a) Epoch difference from mean versus L/D ratio of the selected aerodynamic angles

(b) Epoch difference from mean versus $C_D A$ of the selected aerodynamic angles

Figure 9.7: Aerodynamic coefficients and ratios for Simulation 1.5

in the decay of the orbits. Additionally, in case the $C_D A$ is close to zero, the effect of the Earth flattening can also play an important role in the re-entry interface position. Fortunately, as seen in a number of figures in this section, the majority of the attitude combinations give an absolute value of $C_D A$ rather large. 80.5 % of the simulations had a $C_D A$ more negative than 20 m^2, which is when the difference in the epoch starts to reach 200 min after the mean epoch. Thus, it can be assumed that most of the re-entry epoch interfaces will be around the -200 and 200 min if a $C_D A$ of $-20\,\text{m}^2$ or smaller is found to be the average in the future simulations.

9.2. Simulation 2: Random Initial Attitude and no TLE Error

The second batch of simulations will consist of a number of simulations to understand the rotational dynamics and its effect on the re-entry interface epoch. This means that there will be no initial state TLE errors, and the main focus will be on comparing the results of the fixed aerodynamic angles with a free rotational dynamics model. This is done to better understand the differences between only using

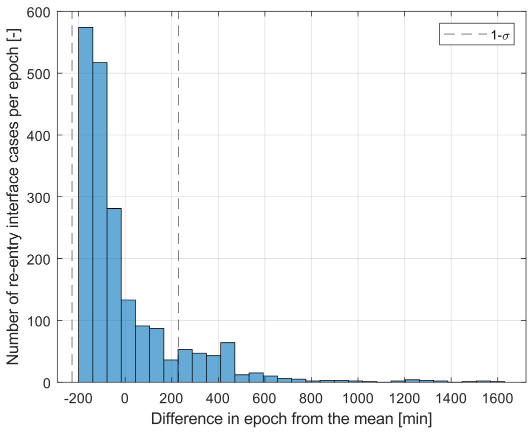

Figure 9.8: Histogram for epoch difference for simulation 1.6

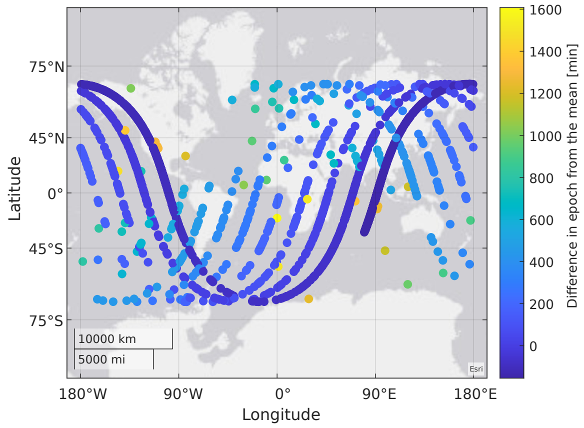
75°N
45°N
0°
45°S
75°S
Latitude
180°W
90°W
0°
90°E
180°E
Longitude
10000 km
5000 mi
Esri
1600
1400
1200
1000
800
600
400
200
0
Difference in epoch from the mean [min]

Figure 9.9: Final re-entry interface longitude and latitude for all the simulations in Simulation 1.6

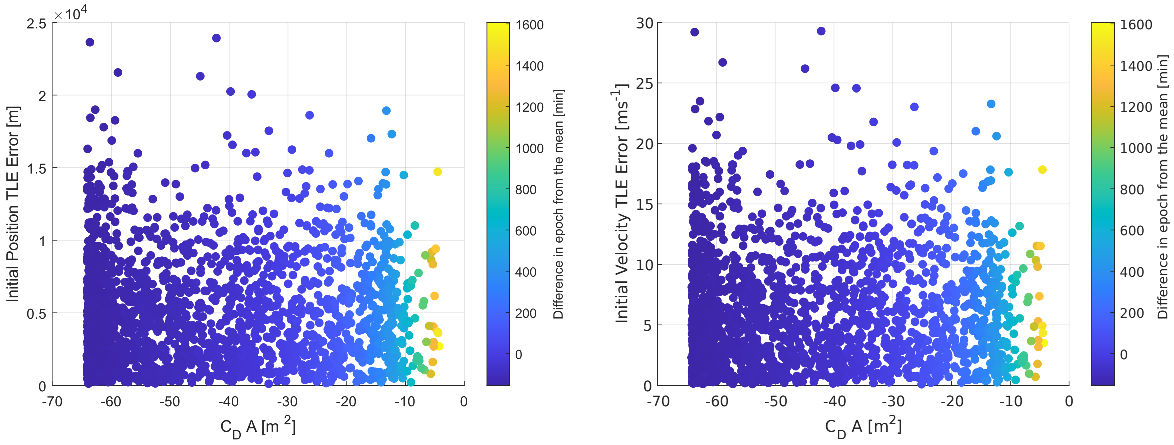

(a) Initial position TLE

(b) Initial velocity TLE error

Figure 9.10: Initial TLE errors vs $C_D A$ with difference in epoch

translational dynamics and using both translational and rotational dynamics, as it is part of the research question.

9.2.1. Simulation 2 Set-Up

The simulation set-up for this batch is the following:

- **Dynamics:**
  - Translational propagation
  - Rotational propagation
- **Initial State:**
  - Initial position and velocity from TLE
  - Random initial pitch angle
  - Random initial yaw angle
  - Random initial roll angle
- **Termination Condition:**
  - Altitude of 120 km
- **Number of Simulations**
  - 1500 Simulations

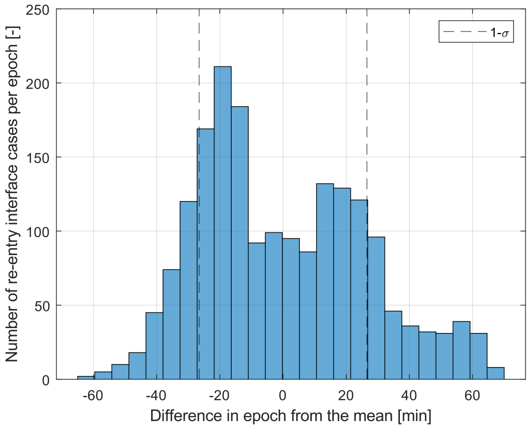

Figure 9.11: Histogram for epoch difference for Simulation 2

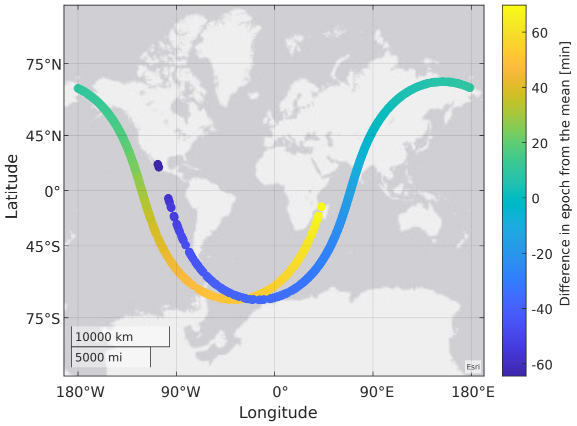

Figure 9.12: Final re-entry interface longitude and latitude for simulations in Simulation 2

As can be seen, both translational and rotational dynamics will be propagated given an initial position, velocity and attitude. In comparison to Simulation 1, for Simulation 2 the aerodynamic torques will also be included in the rotational dynamics. Additionally, only 1500 simulations will be run. This is due to the fact that rotational dynamics require a significant increase in computational time when compared to the translational simulations only. Thus, a smaller number of simulations will be used to save computational time. For reference, a simulation of the first batch using only translational motion would take about 4 s but when using rotational and translational dynamics a simulation would take about 120 s depending on the initial conditions. The change increase in simulation time comes from the fact that the rotational dynamics are faster than the translational ones which require a lot smaller time steps to properly simulate the cases.

9.2.2. Results Simulation 2

The results from Simulation 2 can be seen in Figure 9.11. Once again, it is clear that there is a peak at around ± 20 min, with the one at 20 min being larger. Nonetheless, it can be seen that for the rotational dynamics, the spread is significantly less than for the translational dynamics only, see Figure 9.6 where the graph goes from -200 min to 1600 min. While for the rotational dynamics, the spread is about -60 to 60 min. There is already an improvement in the precision of the final epoch. This improvement can also be seen in Figure 9.12 where only about 1 orbit and a half takes place between the first re-entry interface epoch and the last one. While in the case of Simulation 1.6 with only translational dynamics, it takes more than a full day for all re-entry interface epochs to happen.

Now, it is important to understand why there is a peak at -20 min. To understand this behaviour, a number of analysis was performed. Firstly, the initial attitudes versus the difference in the mean epoch are plotted to try to find a correlation. This can be seen in Figure 9.13. It is a bit hard to read the plot as it is in 3D, but when looking at the results in 2D there seems to be no relationship between initial attitude and final epoch difference. Thus, going back to what was done for Simulation 1, the C_DA was looked into.

To do so, a similar approach to that of Simulation 1 was performed. The different angles of attack and sideslip angles are saved, along with the force body coefficients for the simulation. Then, the aerodynamic angles are calculated for each time step. Now, different to Simulation 1 where the angles were constant, and the aerodynamic coefficients didnot vary much as they were taken from the database of coefficients for the lowest density case, the aerodynamic coefficients varied a significant amount for Simulation 2. This is due to the fact that the rotational dynamics made the coefficients vary in a large range. Thus, in order to get a good average aerodynamic coefficient, a weighted average based on the time step of the simulation was performed. This way, the aerodynamic coefficients are averaged with respect to their influence on the dynamics and not the whole propagation. The average C_DA and L/D ratio are plotted to try and understand the difference in the epoch behaviour. The results can be seen in Figure 9.14. Once again, the L/D ratio plot does not help explain the epoch difference distribution. It

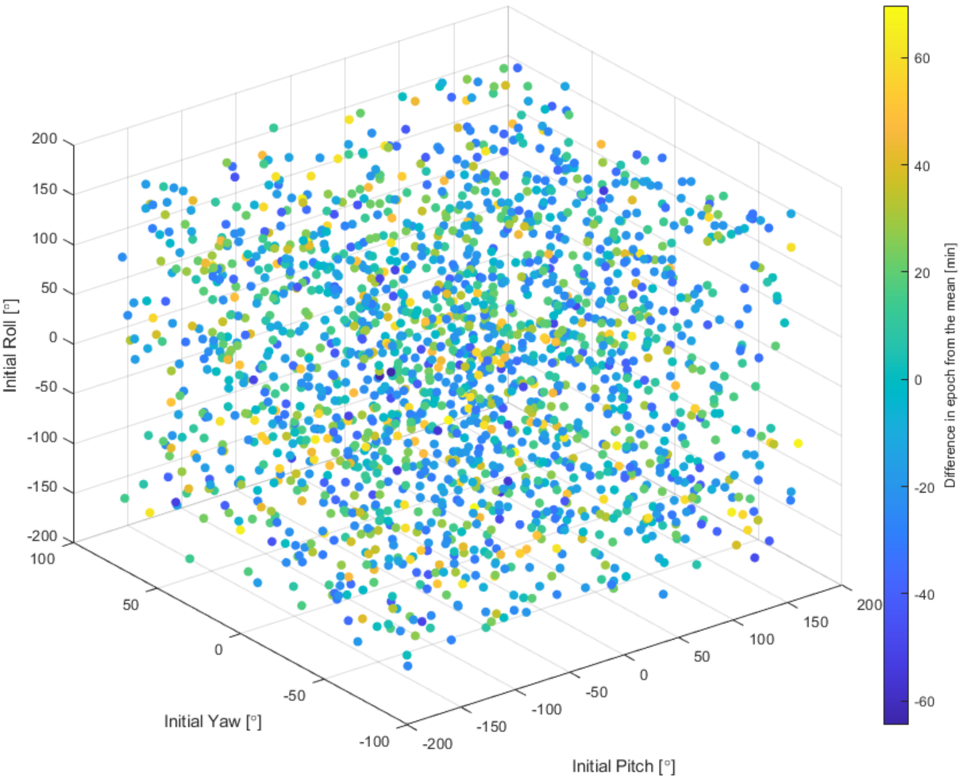

Figure 9.13: Initial attitude vs difference from mean epoch for Simulation 2

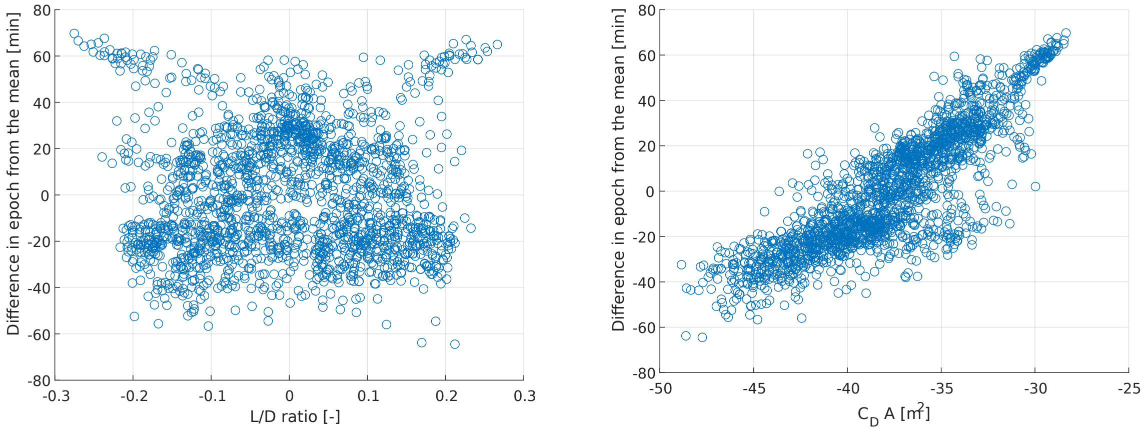

(a) Epoch difference from mean versus mean L/D ratio

(b) Epoch difference from mean versus average C_DA

Figure 9.14: Aerodynamic coefficients and ratios for Simulation 2

can be seen that for the peak at -20 min, the spread of the L/D ratio is between -0.2 and 0.2 while for the peak at 20 min, most of the concentration of the values are at around the L/D ratio of 0. There is no clear relation between the L/D ratio and the re-entry interface epochs.

When looking at the C_DA effect, see Figure 9.14b, there seems to be a clear linear relationship. This is unexpected based on the previous results from Simulation 1, which shows exponential behaviour. However, when looking at the spread of the different C_DA, it is significantly smaller than for the fixed attitude case. Thus, it does make sense that when focusing on a small part of an exponential graph, you get a linear behaviour. Additionally, it is believed that this smaller range of C_DA is due to the fact that there are rotational dynamics involved. As the satellite is rotating during the decay, the coefficients sort of average out. The spread of the -45 to $-30\,\mathrm{m}^2$ seen for the rotational dynamics lies in the mean of the epoch chase for the translational simulation. This reinforces the idea of an averaging out due to the fast rotational dynamics experienced during re-entry.

The main conclusion that can be drawn from Simulation 2 was that the due to the rotational dynamics, the C_DA gets averaged throughout the simulation. This means that all the behaviour for the C_DA close to zero is not seen in the re-entry interface epochs. This average C_DA for the rotational dynamics also agrees with the mean re-entry epoch for Simulation 1. Additionally, due to the averaging of the C_DA, the spread of the re-entry interface epochs is significantly smaller than for the constant aerodynamic angle case, with all re-entry interface epochs being within 2 hours. Once again, the L/D ratio does not seem to have any relationship to the re-entry epochs whatsoever and the behaviour tends to be dominated by the C_DA. Finally, there are two peaks in the re-entry interface epoch distribution. These peaks are believed to be, once again, due to the C_DA distribution having more average cases around the values in which the re-entries happen to be at $\pm$ 20 min.

9.3. Simulation 3: Random Initial Attitude and TLE Error

The third batch of simulations will consist of a number of simulations to understand the effect of the TLE errors when paired with translational and rotational dynamics and its effect on the re-entry interface epoch. The main focus will be on comparing the results of Simulation 2, where no TLE errors are present, with those of Simulation 3 and to understand if the TLE errors play an important role in the simulation.

9.3.1. Simulation 3 Set-Up

The simulation set-up for this batch is the following:

- **Dynamics:**
  - Translational propagation
  - Rotational propagation
- **Initial State:**

  - Initial position and velocity from TLE
  - Initial position and velocity error from TLE
  - Random initial pitch angle
  - Random initial yaw angle
  - Random initial roll angle
- **Termination Condition:**
  - Altitude of 120 km
- **Number of Simulations**
  - 1500 Simulations

For this simulation batch, all the aspects of interest in this thesis will be applied. The rotational and translational dynamics, as well as the whole environment and initial TLE error, will be propagated. This simulation will give a lot of insight into how important the behaviour of the simulation is when all the different aspects, which have been previously covered, are applied.

9.3.2. Results Simulation 3

The results from Simulation 3 can be seen in Figure 9.15. Once again, there are two peaks, at around $\pm$ 20 min. However, when comparing the frequency of these values to those from Simulation 2, it can be seen that the frequency at which these values happen is lower. The TLE errors tend to spread the error a bit more instead of centralizing it around the peaks. The same behaviour was seen in Simulation 1.5, when only translational dynamics and TLE plus translational dynamics are used. Once again, the longitude and latitude at the re-entry epoch have been plotted in Figure 9.16. The behaviour is similar to that of Simulation 2, where it takes about one orbit and a half for all the re-entries to occur.

Similar to the previous cases, it is important to look at why this behaviour happens. Based on the previous results, it would be expected that the general behaviour of the dynamics is similar to that of Simulation 2. This was indeed the case. Firstly, there seems to be no relationship between the initial attitude and the final re-entry interface epoch. Furthermore, when looking at the L/D ratio and re-entry epoch, seen in Figure 9.17, there is a bit of a cluster at 20 min from the mean epoch when the L/D ratio is between -0.05 and 0.05. This suggests that if the L/D ratio is on the lower side, the satellite is more likely to take longer to reach the re-entry interface, as expected. Similarly, the values around the -20 min epoch have two sets of clusters at around -0.2 to -0.05 and 0.05 to 0.2. There are some exceptions, but most of the values in this range lie between the -10 and -30 min range. When looking into why this was the case, see Figure 9.19, it was discovered that for the values in the -10 to -30 min epoch range, the C_DA was lower, in the range of -40 to −49 m^2. Thus, similar to what was found in Simulation 1, the L/D ratio is important, but the value of the C_DA is also important in determining whether it will re-enter before the mean or afterwards. It is interesting to note that for Simulation 2 this behaviour was not fully seen. For a number of the L/D ratios between -0.05 and 0.05, the re-entry interface epoch is also around -20 min. It is theorised that this is due to the fact that the TLE errors provided a wider range of initial starting positions and velocities and the spread of the data made it easier to find this relation.

The last aspect to look into is the effect of the initial TLE errors in the final re-entry epoch time. The effect of the TLE position and velocity errors can be seen in Figure 9.20, respectively. Once again, it can be seen that the shift in colour is dependent on the C_DA rather than the TLE errors. This is similar to the behaviour seen in Simulation 1.6. Thus, it can be concluded that while the TLE errors do play a role in making sure the re-entry epochs are more evenly spread, the driving factor in deciding the re-entry epoch time is still the C_DA. Thus, the main conclusion from Simulation 3 is that the TLE errors, once again, are not the dominant factor in determining the re-entry interface epoch.

9.4. Simulation 4: Re-entry Epoch Spread vs Initial TLE

The last next of simulations will be run in order to understand the spread of the re-entry epoch prediction. All previous simulations have used the last available TLE for the Starlink-5066 satellite. However, this last TLE is at an altitude of about 190 km. This means that the re-entry interface epoch is performed with little to no time before the re-entry occurs. As it is known, time is of the essence in this analysis. Thus, it was decided to analyse the effect of using previous TLEs in the re-entry epoch interface analysis. Thus, this batch of simulations will focus on the change in the re-entry epoch spread based on different initial TLEs.

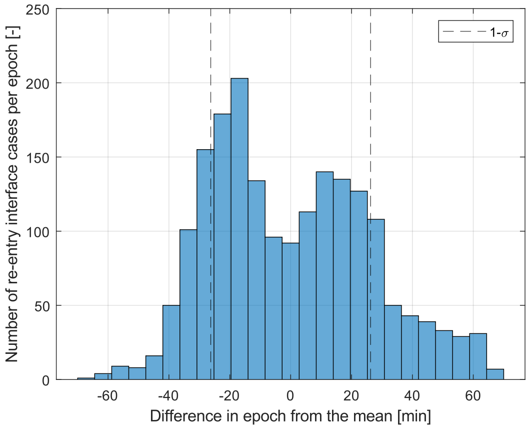

Figure 9.15: Histogram for epoch difference for Simulation 3

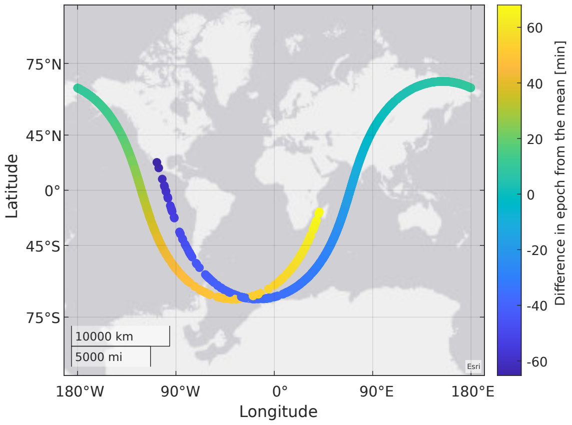
75°N
45°N
0°
45°S
75°S
Latitude
10000 km
5000 mi
Esri
180°W
90°W
0°
90°E
180°E
Longitude
60
40
20
0
-20
-40
-60
Difference in epoch from the mean [min]

Figure 9.16: Final re-entry interface longitude and latitude for simulations in Simulation 3

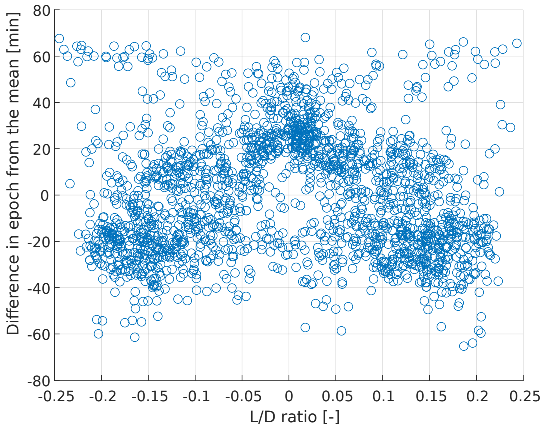

Figure 9.17: Epoch difference from mean versus mean L/D ratio of Simulation 3

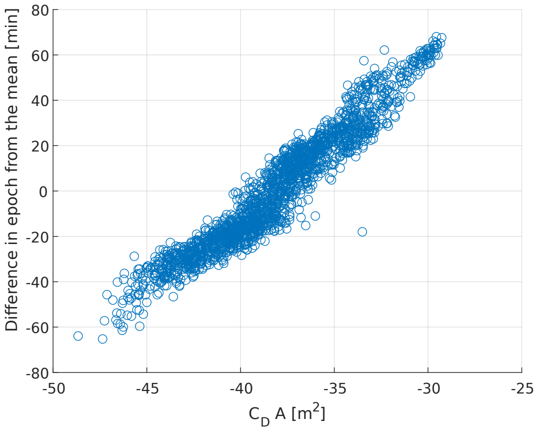

Figure 9.18: Epoch difference from mean versus average $C_D A$ of Simulation 3

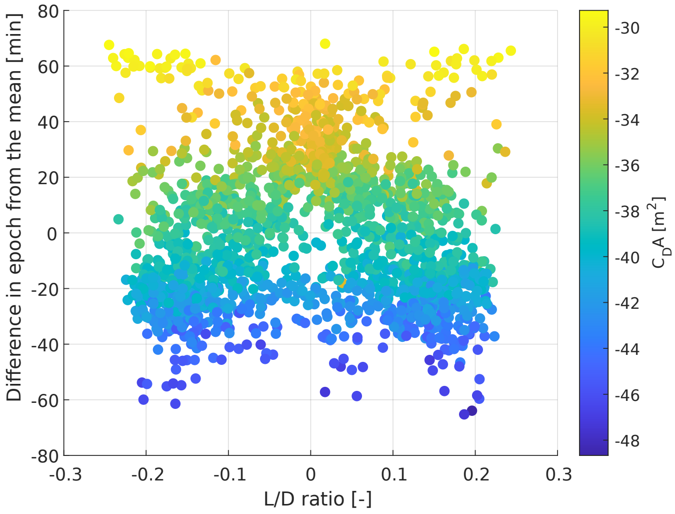

Figure 9.19: Epoch difference from mean versus L/D ratio with total $C_D A$ added as color for Simulation 3

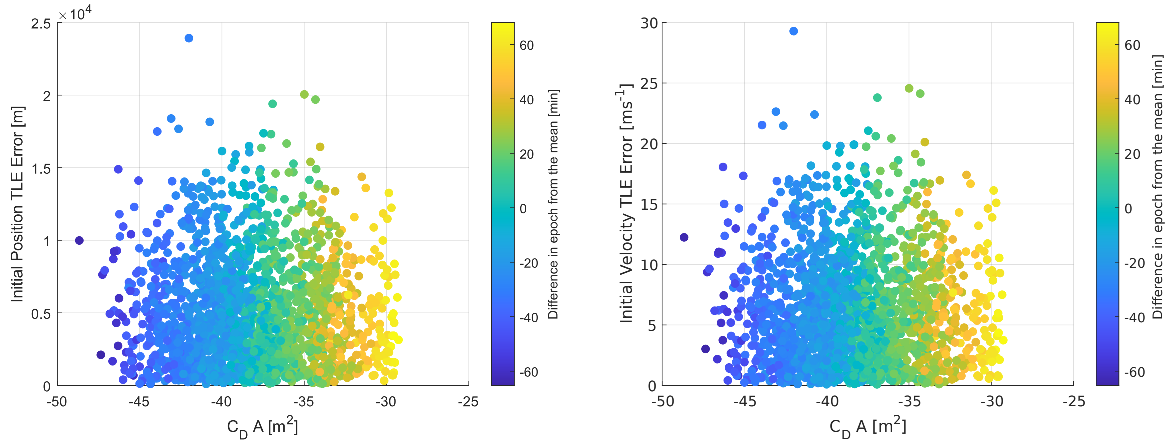

(a) Initial position TLE

(b) Initial velocity TLE error

Figure 9.20: Initial TLE errors vs $C_D A$ with difference in epoch for Simulation 3

9.4.1. Simulation 4 set-up

The simulation set-up for this batch is the following:

- **Dynamics:**
  - Translational propagation
  - Rotational propagation
- **Initial State:**
  - Set of 5 TLEs
  - Initial position and velocity from TLE
  - Initial position and velocity error from TLE
  - Random initial pitch angle
  - Random initial yaw angle
  - Random initial roll angle
- **Termination Condition:**
  - Altitude of 120 km
- **Number of Simulations**

Table 9.2: List of TLEs for Starlink 5066

TLE 1
1 55424U 23014AK 23038.61528550 .00403752 00000+0 16352-2 0 9997
2 55424 70.0079 70.1416 0006767 248.5078 111.5404 15.85077339 2235
TLE 2
1 55424U 23014AK 23039.05682226 .00477605 00000+0 18201-2 0 9990
2 55424 70.0070 68.8711 0006268 250.2205 109.8323 15.86174502 2305
TLE 3
1 55424U 23014AK 23039.62401810 .00561803 00000+0 19601-2 0 9990
2 55424 70.0061 67.2356 0006559 243.9137 116.1394 15.87792198 2395
TLE 4
1 55424U 23014AK 23040.19061852 .01015235 43826-3 34597-2 0 9994
2 55424 70.0045 65.5968 0005544 234.7076 125.3611 15.89660011 2484
TLE 5
1 55424U 23014AK 23041.57247284 .01462306 11067-2 37522-2 0 9999
2 55424 70.0044 61.5810 0004761 208.9223 151.1722 15.95313827 2704
TLE 6
1 55424U 23014AK 23042.82309275 .02312358 45523-2 38980-2 0 9992
2 55424 70.0027 57.9074 0002871 176.1884 183.9351 16.03713891 2903
TLE 7
1 55424U 23014AK 23044.31593119 .17017551 43578-5 42645-2 0 9997
2 55424 69.9915 53.4310 0006040 196.8570 192.1954 16.28763011 3147
TLE 8
1 55424U 23014AK 23044.37237465 .18318819 43709-5 37005-2 0 9994
2 55424 69.9823 53.2471 0007250 179.4720 180.7030 16.31041054 3158

- 100 Simulations per TLE

It should be noted that for this batch, only 100 simulations per TLE, so a total of 500 simulations, are run. This is due to the fact that the interest in this simulation is not so much the distribution of the epochs, but the difference in epoch behaviour when taking different initial TLEs. Additionally, the simulation time takes a significant amount due to the number of orbits that need to be calculated. Thus, to reduce the required computational time, only 100 simulations per TLE are run. The TLEs that will be used as starting conditions are TLE 4 to TLE 8 in Table 9.2. This batch of simulations will be called Simulation 4.3.

Additionally, two other simulations will be run. Firstly, a simulation starts at a given epoch and is propagated until the next epoch is performed. This propagation will be done for all consecutive pairs of TLEs available. Then, at each final epoch, the final translational state from the propagation will be compared to the TLE translational state for said epoch. This error behaviour will show how propagation error behaves. This simulation is called Simulation 4.1. Secondly, a simulation starting from the earliest TLE, seen in Table 9.2 as TLE 1, and propagating until the last available TLE, seen in Table 9.2 as TLE 8, will be run. Then, at each available TLE epoch, the difference in the translational state between the propagation and the TLE value will be calculated. This error behaviour will show how propagation error behaves if no updates on the translational state are given. This simulation will be called Simulation 4.2. For these two simulations, the initial attitude and the TLE errors are set to zero in order to simulate a ”nominal” case.

9.4.2. Results Simulation 4.1 and Simulation 4.2

The results of Simulation 4.1 and 4.2 can be seen in Table 9.3. For these simulations, a table was chosen over a plot. This is due to the fact that the error behaviour for the TLE depends on a number of factors, such as the altitude of the TLEs and epochs. Thus, to be able to fully understand the error behaviour, it was decided to generate a table. A visual representation with the orbits, TLEs and satellite location at the TLE epochs for Simulation 4.2 can also be seen in Figure 9.21.

Table 9.3: Results from Simulation 4.1 and 4.2

TLE	Altitude of TLE [km]	Epoch of TLE since J2000 [s]	Delta of Epochs [s]	Simulation 4.1 Position Error [km]	Simulation 4.2 Position Error [km]
1	320.3	729053229.9	-	0	0
2	316.9	729091378.6	38148.7	98.5	98.5
3	312.9	729140384.3	49005.7	152.2	367.0
4	307.9	729189338.6	48954.3	157.2	815.7
5	292.7	729308730.8	119392.2	859.4	3032.6
6	268.6	729416784.4	108053.6	1364.4	7128.3
7	198.2	729545765.6	128981.2	3465.2	13153.3
8	197.1	729550642.4	4876.7	5.2	13215.7

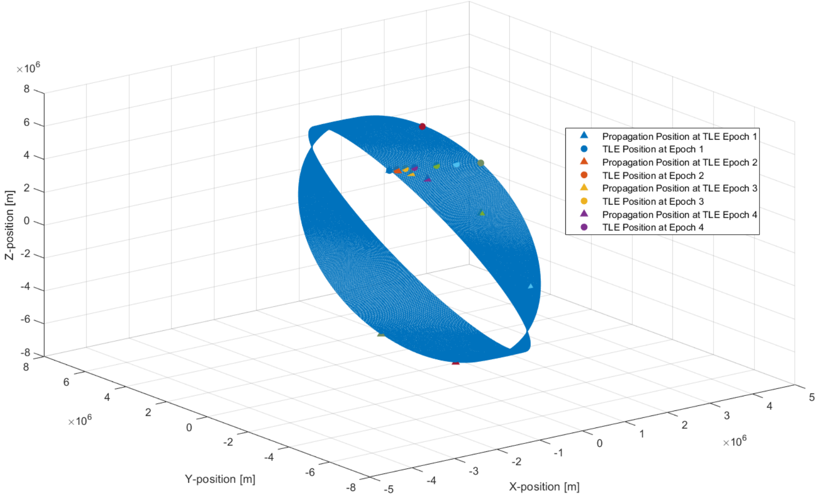

Figure 9.21: TLE positions and satellite position at the TLE epochs

When looking at the error behaviour, the first clear distinction is that Simulation 4.2 has increasing errors as the TLE progress. This is expected, as the initial position is not reset after comparing the propagation results to the TLE values at the given TLE epoch. The error for Simulation 4.2 reaches a maximum of 13 215 km at the last available TLE. For Simulation 4.1 where the position and velocity of the satellite is reset after comparing it at the given epoch, the maximum position error is of 3465.2 km. It is clear that by resetting the position and velocity after each available TLE, the total error can be reduced.

Additionally, when looking at the values, there seems to be a relationship between propagation time and error for Simulation 4.1. The longer the propagation times, the larger the error. Furthermore, at lower altitudes, the error also tends to be larger even if the propagation time is similar. For instance, the error for TLE 6 in Simulation 4.1 is of 1364.4 km for a propagation time of 108 053.6 s at an altitude of 268 583.3 m. however, when looking at the error for TLE 5 of the same simulation, the error is of 859.4 km for a propagation time of 119 392.2 s but at an altitude of 292 748.8 m. This shows that even though the simulation time is important, the lower altitudes also play an essential role in the error behaviour. This behaviour is harder to see in Simulation 4.2 due to the error being propagated since the first TLE. Nonetheless, it is also clear that the error increases significantly more at lower altitudes than in the previous cases.

Lastly, in the visual representation of Simulation 4.2, Figure 9.21 and the zoomed in version in Figure 9.22, it can be seen that the current model used in this thesis causes the satellite to ”lag behind”. With increasing propagation time from a given epoch, the propagated satellite position tends to be earlier in orbit than the TLE data. For instance, for the last TLE, the red-coloured point, the difference between the TLE and the propagation value is almost half an orbit. This means that the model predicts the satellite

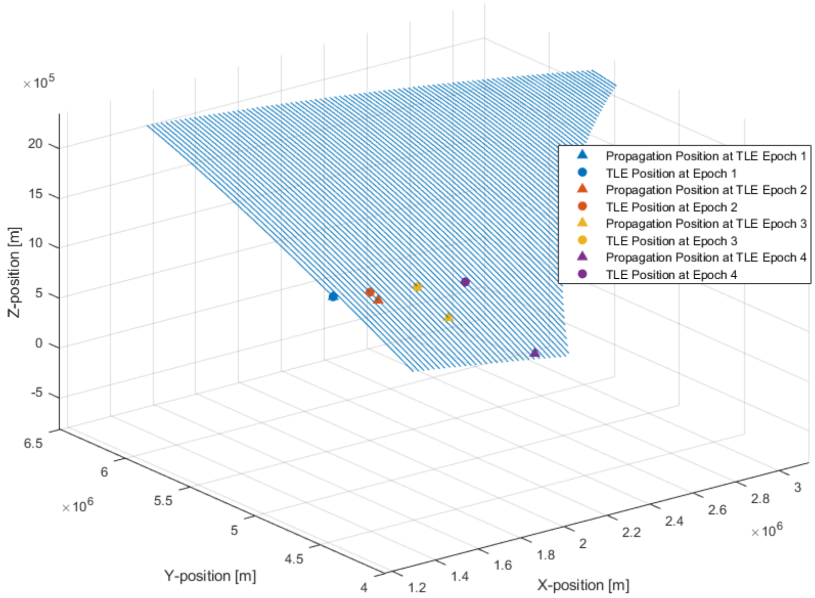

Figure 9.22: Zoomed in plot for TLE position and the corresponding propagation position at epochs 1 to 4

slows down more than it should. In order to analyse why this happens, it was decided to look at the B^* value of the satellite versus that of the TLEs. The B^* value is calculated using the following equation:

$$B^* = \frac{\rho_0 B}{2} = \frac{\rho_0 C_\text{d} A}{2m} \tag{9.1}$$

where C_d is the drag coefficient, A is the reference area, m is the mass of the satellite and ρ_0 is defined as $0.157\,\mathrm{kg\,m^{-2}R_E^{-1}}$ [Hoots et al. 1980]. In essence, it is a normalised ballistic coefficient. This value is used in the SGP4 propagator, and it takes into account all perturbations, thus it is not the best method of comparison. However, at the lower altitudes where the aerodynamic perturbation is the dominating factor, it can be used as a reference value to compare what the SGP4 calculated this value to be versus the value that is achieved in the propagation. From the last TLE available, TLE 8, the B^* is supposed to be $3.705\times10^{-3}\mathrm{R}_E^{-1}$. When calculating the B^* for the propagation, the value of $C_D A$ is taken as $37.5\,\mathrm{m}^2$, the average value for Figure 9.18, and the mass is taken as 260 kg. This yields a value of B^*_{prop} is around $1.13\times10^{-2}\mathrm{R}_E^{-1}$. It can be seen that the value of B^*_{prop} is about 250% larger than the one from the TLE data. Thus, it can be expected that the satellite lags behind, as the aerodynamic forces should slow it down. However, as will be seen in the results from the next section, this lagging behind in the orbit does not necessarily translate to a faster re-entry. This is due to the fact that for the propagation, the lift and side force are also taken into account. It is believed that the use of the lift force in combination to the drag force and sideslip force causes the satellite to lag behind but not re-enter faster.

9.4.3. Results Simulation 4.3

The results from Simulation 4.3 can be seen in Figure 9.23. In said figure, there are a number of different histograms with different colours. Each of the colours represents the data of epochs from a different TLE. From the data, it can be seen that for the TLEs which start earlier in time, the final re-entry interface epoch is further down in time. This means that the software tends to underestimate the orbital decay. It should be noted that there tends to be a bit of overlap between the different TLEs results. For instance, there is some overlap between TLE 1 and TLE4 and TLE4 and TLE 5. This suggests that if the initial TLEs have a similar starting altitude, which is the case for TLE1 and TLE4 and TLE4 and TLE5, there is some overlap possible. Additionally, as the initial epoch of the TLEs gets closer to the re-entry interface epoch, the prediction of said interface gets better. For instance, the difference between the last two TLEs

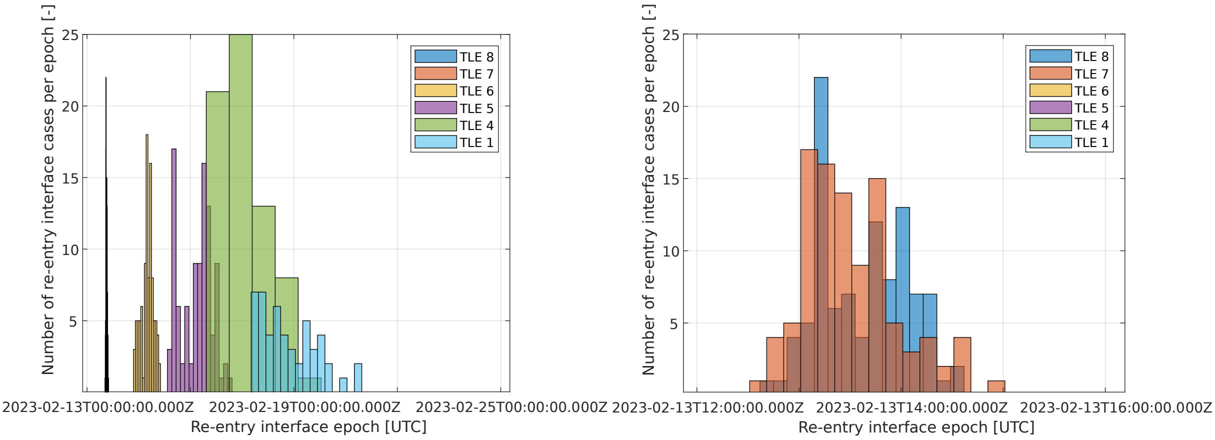

(a) All TLEs

(b) TLE 8 and TLE 7

Figure 9.23: Histogram for the different re-entry interface epochs with different starting TLEs

is negligible, with all the predicted re-entry interface epochs of the last TLE being inside the predicted re-entry interface epochs of the second to last TLE, seen in Figure 9.23b.

The main takeaway from the results of Simulation 4 is that, firstly, the re-entry interface epoch highly depends on the starting TLE for the prediction. Secondly, the error increases drastically if the position and velocity from new TLEs are not added to the propagation. Finally, for the latest TLEs, it has been shown that the re-entry interface epoch window lies within the previous one. This is good news as this means that it is possible to predict the re-entry interface epoch to some extent even if the last TLE is not known.

9.5. Simulation 5: Into the Future

The last batch of simulations done for the thesis will consist of predicting the re-entry of a Starlink satellite. So far, all the simulations have been performed for satellites that have already re-entered. However, it is important to see if it is possible to estimate with certain accuracy the re-entry of future satellites. Thus, for Simulation 5, a satellite that is currently in orbit, in this case the Starlink 1181, has been chosen. As per the previous simulations, the set-up and results will now follow.

9.5.1. Simulation 5 set-up

The simulation set-up for this batch is the following:

- **Dynamics:**
    - Translational propagation
    - Rotational propagation
- **Initial State:**
    - Initial position and velocity from TLE
    - Initial position and velocity error from TLE
    - Random initial pitch angle
    - Random initial yaw angle
    - Random initial roll angle
- **Termination Condition:**
    - Altitude of 120 km
- **Number of Simulations**
    - 500 Simulations

It should be noted that the TLE used for this simulation will be different from the previous one. The TLE used for this simulation is seen in Table 9.4. Additionally, as the propagation is going to go into

Table 9.4: TLE of for Simulation 5. Taken on the 04 of May

STARLINK-1181
1 45086U 20006AU 23124.38069328 .00587501 00000+0 40862-2 0 9999
2 45086 52.9609 173.1752 0017614 14.0531 346.0972 15.71974117180974

dates that are yet to come, the data for the a$_p$ and F$_{10.7}$ are predicted values. This will definitely have an influence on the re-entry interface epoch prediction. However, as the epoch predictions of the propagation will be compared to those from the ESA prediction software which also needs to predict the solar and geomagnetic activity, the uncertainty will be present in both predictions.

9.5.2. Results Simulation 5

The results from Simulation 5 can be seen in Figure 9.24. As can be seen, the prediction of the re-entry interface follows a similar distribution as the previous cases. When looking at it, the mean date is 2023-05-25 at 01:27 UTC, with the earliest epoch being 2023-05-23 at 14:31 and the latest re-entry being 2023-05-26 at 09:39. The spread of the re-entries is of 3 days. This is interesting, as the results from Simulation 5 match, to some extent, the spread of the results from TLE 1 in Simulation 4.3, where the spread was also of 3 days. This is, to some extent, expected as the initial altitude is similar, and the solar cycle has not changed between the re-entry of Starlink 5066 and the current date of interest. Additionally, based on results from Simulation 4.3, it was seen that the re-entry interface window for TLE 1 and TLE 4 was shifted by about 6 days from the re-entry interface window for the latest available TLE. If we apply these 6 days as a correction factor to the results, it is expected that Starlink 1181 will re-enter at around the 17 of May 2022.

Now, it is important to compare these results with some other possible results. The comparison will be made against the re-entry prediction from the ESA RAPID software. The predicted re-entry of Starlink 1181 can be seen in the ESA re-entry portal website[1]. The re-entry prediction of ESA for Starlink 1181 while using the TLE from the 04 of May as the initial state can be seen in Figure 9.25. ESA gives a prediction window between May 15 and May 22, with the expected value being around the early morning of May 19. When comparing the prediction of ESA with that of our software, it can be seen that if the correction factor of 6 days is applied, the re-entry prediction windows are very similar. There are still some discrepancies, which are expected due to the different assumptions made in the software used. For instance, the ESA RAPID tool assumes the C_L of the satellites is zero, which has been shown to not be the case for Starlink, especially with some configurations where the L/D ratio is up to 0.3 Additionally, there is also the difference in the atmospheric models used and the prediction for the solar and geomagnetic activity prediction too. For this project, the predictions from the Celestrack file[2] are used, while for the ESA prediction software, it is not known if they use the same file or the predictions from their own forecast software, called SOLMAG[3]. Overall, a number of different parameters can affect the prediction.

Furthermore, it should be noted that the predictions from ESA 15 days out are also not perfect. For instance, for Starlink 1065 which re-entered on April 20, 14 days before the re-entry ESA's prediction was a re-entry epoch window between April 13 and April 18. Thus, it is important to also take this into account when comparing the different values. After all, it is only a prediction.

---

[1] `https://reentry.esoc.esa.int/home` (Last access: 05 May 2023)

[2] `https://celestrak.org/SpaceData/sw19571001.txt` (Last access: 05 May 2023)

[3] `https://sdup.esoc.esa.int/solmag/` (Last access: 05 May 2023)

[4] Source:`https://reentry.esoc.esa.int/home` (Last access: 05 May 2023)

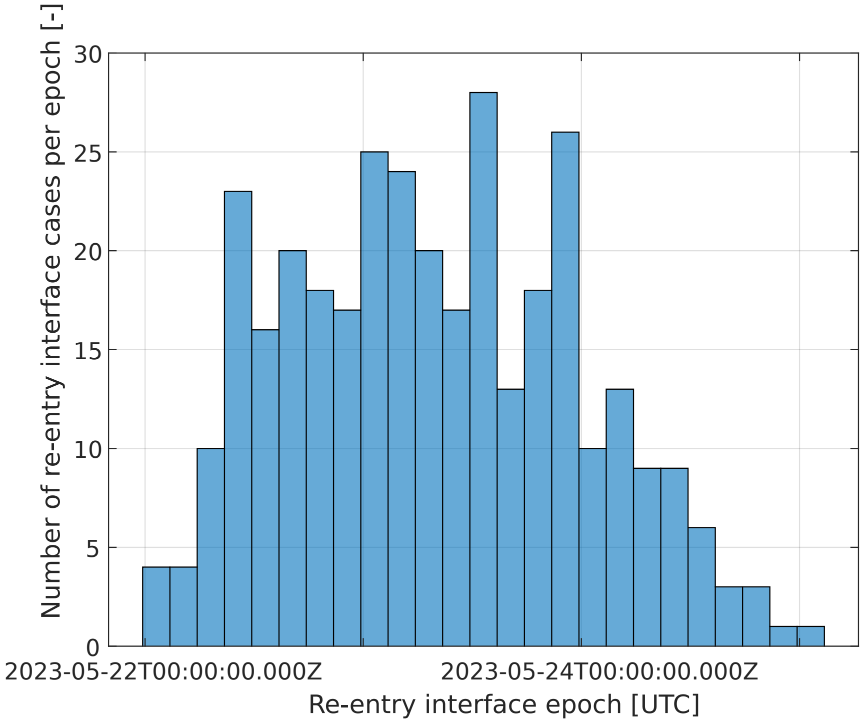

Figure 9.24: Histogram for the different re-entry interface epoch predictions for Simulation 5

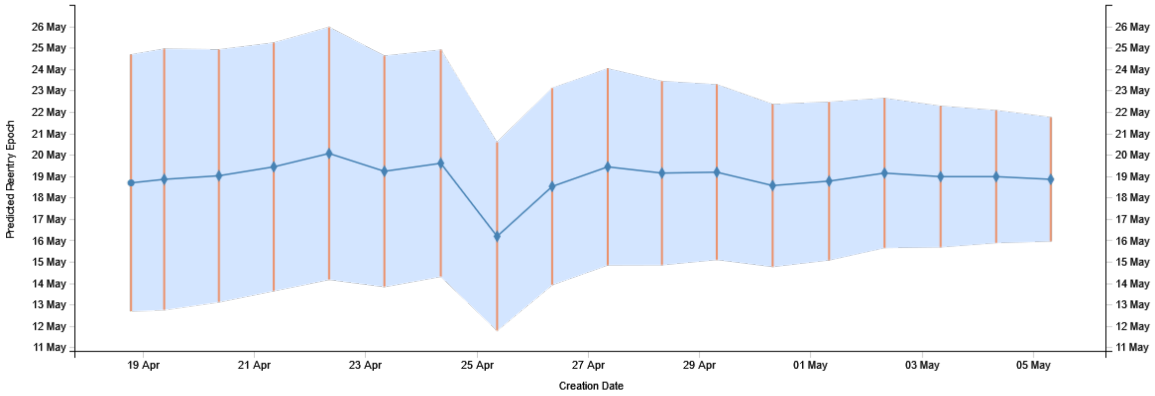

Figure 9.25: ESA's re-entry prediction for Starlink 1181 ^{4}

10

Conclusions and Recommendations

It is now time to conclude this thesis work. So far, this thesis saw the introduction to the different aspects that affect the orbital decay of a satellite. A focus was presented in the aerodynamics of the satellite, with an emphasis on the generation of the force and moment coefficients, along with the effect of these aerodynamic coefficients in the orbital propagation when translational and rotational dynamics are applied. Furthermore, a study on the initial state uncertainty, both in the rotational and translational state, was performed to better understand the effect of this uncertainty in the orbital decay of the satellite. In the introduction of this project, the objective question was introduced. Said objective is the following:

To achieve an improved re-entry epoch prediction by means of applying a more accurate aerodynamic model of the object in orbit and taking into account initial state uncertainties to have a better impact prediction on Earth.

From the research objective, four main sub-questions were developed in order to fulfil the objective. These were:

1. Is there an improvement in the re-entry epoch prediction when using variable values for the aerodynamic coefficients?
2. What is the effect of adding rotational dynamics to the re-entry interface epoch prediction?
3. What is the effect of the initial state uncertainty on the re-entry epoch prediction?
4. Is it possible to perform a re-entry epoch prediction on the current Starlink satellites? If so, what is the change in the accuracy of epoch prediction with respect to ESOC prediction model?

To answer these questions, the project at hand consisted of initial research, which lead to a literature study and was followed by the construction of the software and the data analysis from the results of said software. The conclusion reached in this chapter comes from the analysis of the results from the previous chapter. Additionally, a series of recommendations will be given based on the discussions made in the previous chapters.

10.1. Conclusion

Firstly, the first sub-question regarding the accuracy of the re-entry prediction epoch when using variable values for the aerodynamic coefficients has a number of conclusions. When looking only at translational propagation with fixed aerodynamic angles, and thus constant aerodynamic forces, the results from Simulation 1 give a lot of insight. From the results of Simulation 1, it was clear that using a constant aerodynamic coefficient might not represent real-life situations. The behaviour of the Starlink satellite was highly dependent on the value of C_DA. Thus, using a constant aerodynamic coefficient for the force interactions will result in values that do not necessarily predict the re-entry interface epoch properly.

Additionally, it is also interesting to note that for some specific shapes, such as Starlink, having the lift force included in the simulation models should be a must. Most of the prediction models of today still only depend on the drag force and ignore the rest of the aerodynamic forces. However, as has been seen in this thesis, in some cases the L/D ratio got up to 0.2. This is an interesting result which should be studied forward more, as a more realistic representation of the aerodynamic forces could result in a better re-entry epoch prediction.

Secondly, the effect of the rotational dynamics on the re-entry interface epoch was studied in Simulation 2 and Simulation 3. From these two simulations, it was concluded that the rotational dynamics play an important role in the re-entry interface prediction due to the effect it has on the average C$_D$A of the satellite. From these simulations, it was concluded that the rotational dynamics reduce the ranges of C$_D$A experienced by the satellite. This reduction in the C$_D$A was translated to a lower spread of the re-entry interface epoch prediction, from about 1800 min for Simulation 1 to around 140 min for Simulation 2 and Simulation 3.

Thirdly, when looking at the effect of the initial state uncertainty on the re-entry interface epoch prediction, Simulation 1.6, Simulation 2 and Simulation 3 reach the same conclusion. The effect of the initial TLE error is not insignificant, but the re-entry interface epoch was significantly more dependent on the average C$_D$A experienced by the satellite during the orbit propagation than on the TLE initial error. The initial TLE error for the translational motion does spread the final re-entry interface epoch window more, but this error was dominated by the C$_D$A experienced. Additionally, it was also determined that the initial attitude did not have any effect on the final re-entry interface epoch. There was no correlation between the initial attitude and the final re-entry interface epoch. This means that the nominal attitude case can be used for all the propagations as long as the rotational dynamics are included.

Lastly, the re-entry interface epoch was predicted for Starlink 1181 which is still in orbit and compared to the values from the ESOC website[1]. Before this comparison was performed, a simulation to analyse the error in position and velocity of a satellite when different starting TLE epochs are used was run, Simulation 4. The results from Simulation 4 showed that when the initial TLE had an altitude of around 300 km, the prediction of the re-entry interface epoch was off by about 6 days when compared to the prediction from the last available TLE. This information was used to correct the prediction from Simulation 5. In Simulation 5, the last available TLE for Starlink 1181, at the moment in which this thesis was being written, was used as the starting point for the prediction of the re-entry interface epoch for a satellite that is currently decaying. The re-entry interface epoch window of Simulation 5 is compared to the prediction of the ESA software for the same starting TLE. The conclusion was that the initial prediction of this thesis was off by 7 days from the mean of the ESA software. However, when applying the correction factor of 6 days that were taken from Simulation 4, the re-entry interface epoch window of this thesis and that of the ESA are in close agreement.

In conclusion, the aerodynamic coefficient analysis that was performed in this thesis suggests that more accurate aerodynamic modelling will be beneficial for the re-entry interface epoch prediction. The dependency of the re-entry interface epoch on the average C$_D$A experienced by the satellite was rather large and not modelled properly by the TLE data. However, it should be noted that for TLEs that are a couple of weeks out from re-entry, it is not recommended to use a freely rotating rotational dynamic behaviour. As seen from the results of Simulation 4, the satellite tends to lag behind in the orbit, which could be caused by the larger equivalent ballistic coefficient from the simulation than that of the TLEs. It is very likely that far away from the re-entry, the satellite still has the ADCS working, thus, it is maintaining a nominal attitude and the freely rotational dynamics might not properly represent the behaviour of the satellite.

10.2. Recommendations

A couple of recommendations from this project now follow. Firstly, as mentioned in the previous paragraph, for this thesis it was assumed that the Starlink satellite rotational motion was not controlled and that it was affected only by the aerodynamic torques. This can be expected to not hold true for most of the simulation. As Starlink is a communications satellite, it will have a nominal attitude in order to perform its function. Although outside the scope of this thesis, it would be of high interest to see what would be the effect of adding a control algorithm to Starlink. As it was determined in this thesis, the initial attitude had no effect on the final re-entry epoch, but if for the first initial orbits, the attitude of the satellite is constant, the C$_D$A for those orbits be different from the average one for the free rotation case, thus a different re-entry interface epoch will be expected.

---

[1] `https://reentry.esoc.esa.int/home` (Last access: 05 May 2023)

Secondly, a sensitivity analysis should be performed. To begin with, a sensitivity analysis of the density output from the NRLMSISE-00 and its effect on the aerodynamic perturbations should be performed. The density not only plays a role in the aerodynamic force equation, but the aerodynamic coefficients are also dependent on the density. Thus, it would be of interest to see what the effect of the density is on the re-entry interface epoch prediction. It is theorised that it will have a larger effect than the initial TLE errors due to the fact that the density plays a double effect on the aerodynamic forces, which were found to be the driving factor of the re-entry interface epoch. Additionally, for this thesis, the NRLMSISE-00 model was used. The newer NRLMSIS 2.0 model could also be used to have a better estimation of the densities at the lower altitudes, close to 120 km.

Furthermore, a sensitivity analysis can also be carried out for the aerodynamic coefficients. From previous studies such as that of Toonen [2021], it is expected to have a small dependency of the aerodynamic coefficients from SPARTA on the input variables. However, it is important to analyse how accurately SPARTA calculates the aerodynamic coefficients. From the verification and validation, it was seen that for simple shapes the coefficients were very close to the analytical solutions. However, for more complex shapes where some more complex interactions between the particles and the shape of the satellite can occur, an analysis of the behaviour of the coefficients would be interesting. As previously discussed, the C_DA was the driving factor in the re-entry epoch prediction, thus, it is important to understand the behaviour of these coefficients when generated with SPARTA. Additionally, it was assumed that the reflection of the particles was specular. This assumption should be tested in some studies, such as Moe and Moe [2005], when a diffuse reflection was selected, the difference of C$_D$ was up to 20% at altitudes of 300 km when compared to the C$_D$ of using specular diffusion.

Finally, it would be interesting to see the behaviour of a different satellite. For this thesis, focus was placed on the Starlink satellite. The high number of satellites in orbit made it ideal for an analysis that involves generating aerodynamic coefficients for a specific shape. However, the shape of the Starlink is very interesting. Due to the large solar array is it possible to generate a large amount of lift, but also drag depending on the orientation with respect to the flow. It would be of interest to analyse a shape that has a smaller variation on the C_DA and see if the behaviour from the new satellite is similar to that of Starlink. For instance, the Iridium constellation could be an interesting satellite to analyse. The more cubic shape of the satellite, along with the fact that the older satellites are close to the end of their operational life, could provide another interesting case study to compare the results versus those seen in this thesis.

References

Aikin, A., A. Hedin, D. Kendig, and S. Drake (1993). “Thermospheric molecular oxygen measurements using the ultraviolet spectrometer on the Solar Maximum Mission spacecraft”. In: *Journal of Geophysical Research: Space Physics* 98.A10, pages 17607–17613.

Alarcón, J., H. Klinkrad, J. Cuesta, and F. Martinez (2005). “Independent orbit determination for collision avoidance”. In: *4th European Conference on Space Debris*. Volume 587, page 331.

Archinal, B. A., M. F. A’Hearn, E. Bowell, A. Conrad, G. J. Consolmagno, R. Courtin, T. Fukushima, D. Hestroffer, J. L. Hilton, G. A. Krasinsky, et al. (2011). “Report of the IAU working group on cartographic coordinates and rotational elements: 2009”. In: *Celestial Mechanics and Dynamical Astronomy* 109.2, pages 101–135. DOI: `https://doi.org/10.1007/s10569-010-9320-4`.

Boyce, W. (2004). “Examination of NORAD TLE accuracy using the iridium constellation”. In: *Spaceflight mechanics* 119, pages 2133–2142.

Bruinsma, S. and C. Boniface (2021). “The operational and research DTM-2020 thermosphere models”. In: *Journal of Space Weather and Space Climate* 11, pages 47–1. DOI: `https://dx.doi.org/10.1051/swsc/2021032`.

Chambre, P. A. and S. A. Schaaf (1961). “Flow of rarefied gases”. In: *Flow of Rarefied Gases*. Princeton University Press. DOI: `https://doi-org.tudelft.idm.oclc.org/10.1515/9781400885800`.

Defense Mapping Agency, U. S. (1987). *Department of Defense World Geodetic System 1984: its definition and relationships with local geodetic systems*. Volume 8350. Defense Mapping Agency.

Diekmann, F. (2012). “A Satellite Retires-The ERS-2 Deorbiting in Summer 2011”. In: *SpaceOps 2012*. DOI: `https://doi.org/10.2514/6.2012-1275597`.

Dirkx, D. and K. Cowan (2019). *AE4868 – Numerical Astrodynamics. Numerical Integration - Method Selection*.

Dirkx, D. and E. Mooij (2019). *AE4866 – Propagation and Optimization. Formulation of Equations of Motion*.

Doornbos, E. N. (2011). “Thermospheric Density and Wind Determination from Satellite Dynamics”. PhD dissertation. Delft University of Technology. ISBN: 978-90-9026051-8.

Drob, D. P., J. T. Emmert, J. W. Meriwether, J. J. Makela, E. Doornbos, M. Conde, G. Hernandez, J. Noto, K. A. Zawdie, S. E. McDonald, et al. (2015). “An update to the Horizontal Wind Model (HWM): The quiet time thermosphere”. In: *Earth and Space Science* 2.7, pages 301–319. DOI: `https://doi-org.tudelft.idm.oclc.org/10.1002/2014EA000089`.

Emmert, J. T., D. P. Drob, J. M. Picone, D. E. Siskind, M. Jones Jr, M. Mlynczak, P. Bernath, X. Chu, E. Doornbos, B. Funke, et al. (2021). “NRLMSIS 2.0: A whole-atmosphere empirical model of temperature and neutral species densities”. In: *Earth and Space Science* 8.3, e2020EA001321. DOI: `https://doi.org/10.1029/2020EA001321`.

Flohrer, T., H. Krag, H. Klinkrad, B. B. Virgili, and C. Früh (2009). “Improving ESA’s collision risk estimates by an assessment of the TLE orbit errors of the US SSN catalogue”. In: *Proceedings of the 5th European Conference on Space Debris–5th European Conference on Space Debris, Darmstadt, Germany*.

Forbes, J. M. (2007). “Dynamics of the thermosphere”. In: *Journal of the Meteorological Society of Japan. Ser. II* 85, pages 193–213. DOI: `https://doi-org.tudelft.idm.oclc.org/10.2151/jmsj.85B.193`.

Geul, J., E. Mooij, and R. Noomen (2017). “TLE uncertainty estimation using robust weighted differencing”. In: *Advances in Space Research* 59.10, pages 2522–2535. DOI: `https://doi.org/10.1016/j.asr.2017.02.038`.

Hargreaves, J. K. (1992). *The solar-terrestrial environment: an introduction to geospace-the science of the terrestrial upper atmosphere, ionosphere, and magnetosphere*. Cambridge university press. ISBN: 9780511628924.

Hart, K. A., S. Dutta, K. Simonis, B. A. Steinfeldt, and R. D. Braun (2014). “Analytically-derived aerodynamic force and moment coefficients of resident space objects in free-molecular flow”. In: *AIAA*

Atmospheric Flight Mechanics Conference, page 0728. DOI: `https://doi.org/10.2514/6.2014-0728`.

Hartman, P. G. (1993). “Long-term SGP4 performance”. In: *Space Control Operations Technical Note J3SOM-TN-93-01. US Space Command, USSPACECOM/J3SO. Colorado Springs, CO*.

Hładczuk, N. (2022). *SPARTA DSMC Simulator Manual*. Faculty of Aerospace Engineering.

Hoogendoorn, R., E. Mooij, and J. Geul (2018). “Uncertainty propagation for statistical impact prediction of space debris”. In: *Advances in Space Research* 61.1, pages 167–181. DOI: `https://doi.org/10.1016/j.asr.2017.10.009`.

Hoots, F. R., R. L. Roehrich, and T. Kelso (1980). “Spacetrack report no. 3”. In: *Project Spacetrack Reports, Office of Astrodynamics, Aerospace Defense Center, ADC/DO6, Peterson AFB, CO* 80914, page 14.

King-Hele, D. (1964). *Theory of satellite orbits in an atmosphere*. vi. London, UK.: Butterworths.

Knipp, D., W. K. Tobiska, and B. Emery (2004). “Direct and indirect thermospheric heating sources for solar cycles 21–23”. In: *Solar Physics* 224.1, pages 495–505. DOI: `https://doi-org.tudelft.idm.oclc.org/10.1007/s11207-005-6393-4`.

Koura, K. and H. Matsumoto (1992). “Variable soft sphere molecular model for air species”. In: *Physics of Fluids A: Fluid Dynamics* 4.5, pages 1083–1085. DOI: `https://doi-org.tudelft.idm.oclc.org/10.1063/1.858262`.

Kumar, K., P. van Barneveld, D. Dirkx, J. Melman, E. Mooij, and R. Noomen (2012). “Tudat: a modular and robust astrodynamics toolbox”. In: *5th ICATT Conference*. ESA. June 2012, Noordwijk, pages 1–8.

Labonville, F., P. Charbonneau, and A. Lemerle (2019). “A dynamo-based forecast of solar cycle 25”. In: *Solar Physics* 294.6, pages 1–14. DOI: `https://doi.org/10.1007/s11207-019-1480-0`.

Lith, T. van (2020). “Faster Low-Thrust Trajectory Design Through Finite Fourier Series”. Master’s thesis. TU Delft.

Litvin, A., W. Oliver, J. Picone, and M. Buonsanto (2000). “The upper atmosphere during June 5–11, 1991”. In: *Journal of Geophysical Research: Space Physics* 105.A6, pages 12789–12796. DOI: `https://doi.org/10.1029/1999JA000285`.

March, G. (2020). “Consistent thermosphere density and wind data from satellite observations. A study of satellite aerodynamics and thermospheric products.” PhD dissertation. Delft University of Technology. DOI: `https://doi.org/10.4233/uuid:862e11b6-4018-4f63-8332-8f88066b0c5c`.

March, G., E. Doornbos, and P. Visser (2019). “High-fidelity geometry models for improving the consistency of CHAMP, GRACE, GOCE and Swarm thermospheric density data sets”. In: *Advances in Space Research* 63.1, pages 213–238. DOI: `https://doi-org.tudelft.idm.oclc.org/10.1016/j.asr.2018.07.009`.

March, G., J. Van Den Ijssel, C. Siemes, P. N. A. M. Visser, E. N. Doornbos, and M. Pilinski (2021). “Gas-surface interactions modelling influence on satellite aerodynamics and thermosphere mass density”. In: *Journal of Space Weather and Space Climate* 11, page 54. DOI: `https://doi.org/10.1051/swsc/2021035`.

McCarthy, D. D., C. Boucher, R. Eanes, T. Fukushima, T. Herring, J. Lieske, C. Ma, H. Montag, P. Paquet, C. Reigber, et al. (1989). “IERS Technical Note 3”. In: *IERS Standards*.

Mehta, P. M., A. Walker, C. A. McLaughlin, and J. Koller (2014). “Comparing physical drag coefficients computed using different gas–surface interaction models”. In: *Journal of Spacecraft and Rockets* 51.3, pages 873–883. DOI: `https://doi.org/10.2514/1.A32566`.

Moe, K. and M. M. Moe (2005). “Gas-surface interactions and satellite drag coefficients”. In: *Planetary and Space Science* 53.8, pages 793–801. DOI: `https://doi.org/10.1016/j.pss.2005.03.005`.

Moe, K., M. M. Moe, and S. D. Wallace (1998). “Improved satellite drag coefficient calculations from orbital measurements of energy accommodation”. In: *Journal of spacecraft and rockets* 35.3, pages 266–272. DOI: `https://doi.org/10.2514/2.3350`.

Montenbruck, O. and G. Eberhard (2013). *Satellite orbits: Models, methods, and applications*. Springer.

Mooij, E. (1994). “The motion of a vehicle in a planetary atmosphere”. In: *Delft University of Technology, Faculty of Aerospace Engineering, Report LR-768*.

Moreno Gonzalez, A. (2020). “Characterisation of Shape-Based Methods and Combination with Coasting Arcs”. Master’s thesis. TU Delft.

Morokoff, W. and A. Kersch (1998). “A comparison of scattering angle models”. In: *Computers & Mathematics with Applications* 35.1-2, pages 155–164. DOI: `https://doi-org.tudelft.idm.oclc.org/10.1016/S0898-1221(97)00265-4`.

Noomen, R. (2019). *AE2104-Flight and Orbital Mechanics. Lecture slides*.

Peter, H., J. Fernández, and P. Féménias (2020). “Copernicus Sentinel-1 satellites: sensitivity of antenna offset estimation to orbit and observation modelling”. In: *Advances in Geosciences* 50, pages 87–100. DOI: `https://doi.org/10.5194/adgeo-50-87-2020`.

Picone, J., A. Hedin, D. P. Drob, and A. Aikin (2002). “NRLMSISE-00 empirical model of the atmosphere: Statistical comparisons and scientific issues”. In: *Journal of Geophysical Research: Space Physics* 107.A12, SIA–15. DOI: `https://doi.org/10.1029/2002JA009430`.

Pilinski, M. D., B. M. Argrow, and S. E. Palo (2010). “Semiempirical model for satellite energy-accommodation coefficients”. In: *Journal of Spacecraft and Rockets* 47.6, pages 951–956. DOI: `https://doi.org/10.2514/1.49330`.

Pilinski, M. D., R. L. McNally, B. A. Bowman, S. E. Palo, J. M. Forbes, B. L. Davis, R. G. Moore, K. Kemble, C. Koehler, and B. Sanders (2016). “Comparative analysis of satellite aerodynamics and its application to space-object identification”. In: *Journal of Spacecraft and Rockets* 53.5, pages 876–886. DOI: `https://doi.org/10.2514/1.A33482`.

Plimpton, S. and M. Gallis (2022). *SPARTA User Manual*. 7 Jan 2022. Sandia National Laboratories.

Rees, M. H. (1989). *Physics and chemistry of the upper atmosphere*. Cambridge University Press. ISBN: 9780511573118.

Regan, F. J. (1993). *Dynamics of atmospheric re-entry*. Washington, DC, USA.: AIAA.

Rishbeth, H. (1972). “Thermospheric winds and the F-region: A review”. In: *Journal of Atmospheric and Terrestrial Physics* 34.1, pages 1–47. DOI: `https://doi.org/10.1016/0021-9169(72)90003-7`.

Ronse, A. and E. Mooij (2014). “Statistical impact prediction of decaying objects”. In: *Journal of Spacecraft and Rockets* 51.6, pages 1797–1810. DOI: `https://doi.org/10.2514/1.A32832`.

Saltsburg, H., J. N. Smith, and M. Rogers (1966). *Fundamentals of Gas-Surface Interactions: Proceedings of the Symposium Held on December 14-16, 1966 at San Diego, California*. Elsevier.

Sentman, L. H. (1961). *Free molecule flow theory and its application to the determination of aerodynamic forces*. Technical report. LOCKHEED MISSILES and SPACE CO INC SUNNYVALE CA.

Tapping, K. (2013). “The 10.7 cm solar radio flux (F10. 7)”. In: *Space weather* 11.7, pages 394–406. DOI: `https://doi-org.tudelft.idm.oclc.org/10.1002/swe.20064`.

Thomsen, M. (2004). “Why Kp is such a good measure of magnetospheric convection”. In: *Space Weather* 2.11. DOI: `https://doi-org.tudelft.idm.oclc.org/10.1029/2004SW000089`.

Toonen, L. M. (2021). “Horizontal wind influence on satellite aerodynamics at the edge of space”. Master’s thesis. TU Delft.

Torrente, P. (2021). “Uncontrolled Motion for Asteroid Missions. An Application to the Binary Asteroid 1999 KW4”. Master’s thesis. TU Delft.

Vallado, D. and P. Crawford (2008). “SGP4 orbit determination”. In: *AIAA/AAS Astrodynamics Specialist Conference and Exhibit*, page 6770. DOI: `https://doi.org/10.2514/6.2008-6770`.

Vallado, D. A. (2013). *Fundamentals of astrodynamics and applications*. iv. Hawthorne, CA, USA.: Microcosm Press and Springer.

Vallado, D. A. and P. J. Cefola (2012). “Two-line element sets-Practice and use”. In: *63rd International Astronautical Congress, Naples, Italy*, pages 1–14.

Vallado, D. A. and D. Finkleman (2014). “A critical assessment of satellite drag and atmospheric density modeling”. In: *Acta Astronautica* 95, pages 141–165. DOI: `https://doi.org/10.1016/j.actaastro.2013.10.005`.

Vielberg, K. and J. Kusche (2020). “Extended forward and inverse modeling of radiation pressure accelerations for LEO satellites”. In: *Journal of Geodesy* 94.4, pages 1–21. DOI: `https://doi.org/10.1007/S00190-020-01368-6`.

Visser, T., G. March, E. Doornbos, C. De Visser, and P. Visser (2019). “Horizontal and vertical thermospheric cross-wind from GOCE linear and angular accelerations”. In: *Advances in Space Research* 63.10, pages 3139–3153. DOI: `https://doi-org.tudelft.idm.oclc.org/10.1016/j.asr.2019.01.030`.

Wakker, K. F. (2015). *Fundamentals of astrodynamics*. TU Delft Library.

Wertz, J. R., D. F. Everett, and J. J. Puschell (2011). *Space mission engineering: the new SMAD*. Microcosm Press.

Wilmott, P., S. Howson, S. Howison, and J. Dewynne (1995). *The mathematics of financial derivatives: a student introduction*. New York, USA.: Cambridge university press.

Yim, H.-J. and D.-W. Chung (2012). “Validation on residual variation and covariance matrix of USSTRATCOM Two Line Element”. In: *Journal of Astronomy and Space Sciences* 29.3, pages 287–293. DOI: `https://doi.org/10.5140/JASS.2012.29.3.287`.